astro-ph seminar 2026.02.16 (Ryou Ohsawa)

The fate of the failed supernova candidate M31-2014-DS1

E. R. Beasor, 2026, accepted for publication in MNRAS (arXiv:2601.05317)

ABSTRACT

The fate of massive stars above 20$M_\odot$ remains uncertain. Debate persists about whether they die as supernovae (SNe), or if they collapse directly into black holes (BHs) with little or no optical outburst — so-called "failed supernovae". The source M31-2014-DS1 experienced an optical outburst in 2014 and has remained faint at visual wavelengths since then. Due to its persistent faintness, it has been proposed as a failed SN candidate. We present new observations of this candidate obtained using the James Webb Space Telescope (JWST), the Submillimeter Array (SMA), and Chandra. The *JWST* observations demonstrate that a luminous mid-infrared source persists at the same location a decade after the star faded at visual wavelengths. We model its current spectral energy distribution (SED) as a dust-enshrouded star. No X-ray emission is detected, disfavoring the hypothesis that the late-time luminosity is powered by accretion onto a BH. We find that the remaining source is highly obscured by an asymmetric distribution of circumstellar dust, making it difficult to quantify its physical properties using spherically symmetric radiative transfer codes. The dust geometry requires that the inferred bolometric luminosity is only a lower limit, as a significant fraction of the central source's radiation may escape without being reprocessed by dust. We discuss the implications of these findings in the context of failed SN models and consider the potential overlap with signatures expected from a stellar merger, which also seems to provide a plausible explanation of this source.

Background

candidate: NGC 6946-BH1

The "Missing High-Mass Stars" problem: lack of supernovae corresponding to ~18 $M_\odot$

Massive stars are theoretically predicted to sometimes collapse directly into black holes without a luminous supernova.

Observational studies of failed supernovae is crucial for understanding the demographics of stellar-mass black holes.

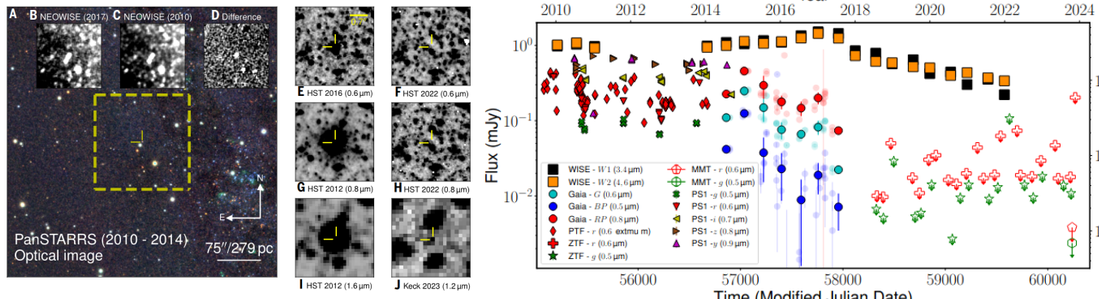

Figures 1 & 2 of De et al. (2026)

De et al. (2026, Science, 2410.14778) reported a new failed supernova candidate in M31 (**M31-2024-DS1**)

They reported a mid-IR brightening followed by sudden fading in optical and NIR wavelengths.

The projenitor was estimated to be a hydrogen-depleted yellow supergiant (~13 $M_\odot$) with a luminosity of approximately 10^5 $L_\odot$.

They argued that a failed supernova scenario explains the observational facts of M31-2024-DS1.

- Sudden fading in optical = No energy input since the stellar core is collapsed.
- Mid-infrared brightening = Eruptive mass-loss () due to a weak shockwave.
- No X-ray detection = the BH accretion activity hidden by a large column density (10^{24} cm^{-2})

Figures 4C & 5B of De et al. (2026)

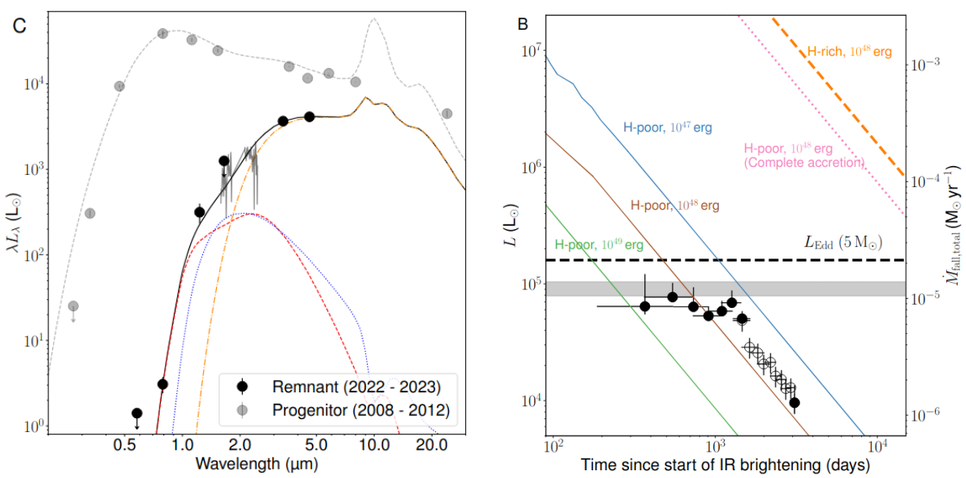

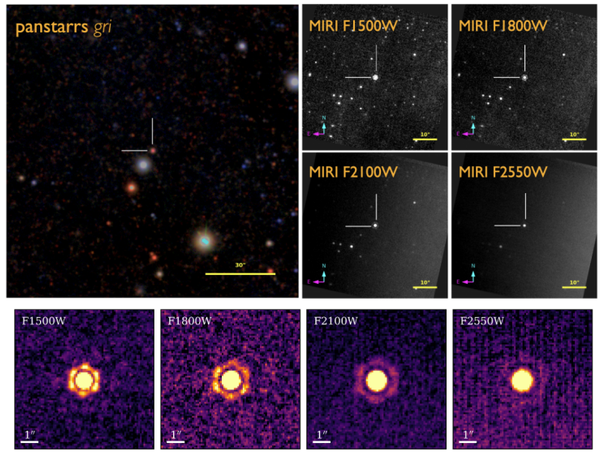

Figure 1 of Beasor et al. (2026): JWST follow-up observations

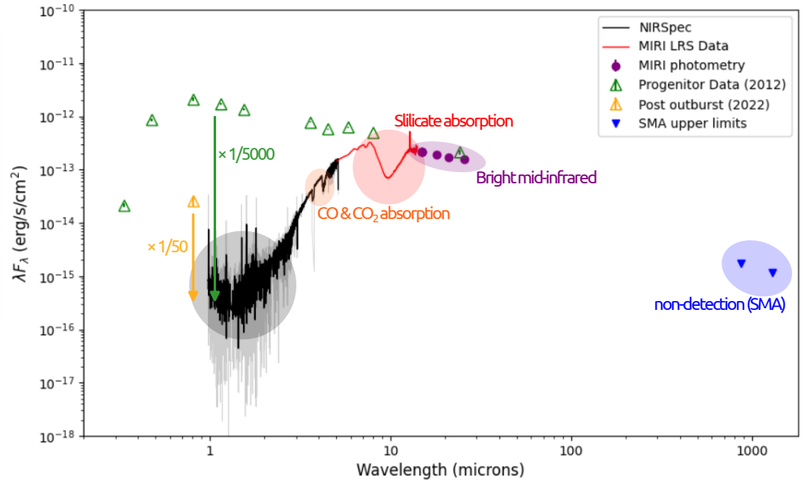

Figure 2 of Beasor et al. (2026): SED comparion between the progenitor and remnant

Observations

They carried out follow-up observations of M31-2024-DS1 to assess the failed SN scenario.

Mid-infrared emission peaking at ~ 10 μm was detected.
No sub-mm radio emission was detected.
No X-ray emission was detected.

James Webb Space Telescope (2024.11.28, DDT PI: Kishalay De):

NIRSpec spectroscopy covering 1.0–5.0 μm with high-resolution gratings

MIRI low-resolution spectroscopy in the 5–14 μm range

MIRI imaging photometry in four filters (F1500W, F1800W, F2100W, & F2550W)

Submillimeter Array (SMA; 2025.02, PI: Emma R. Beasor):

225.5 GHz continuum emission (ongoing mass loss or accretion processes)

Chandra X-ray Observatory (2024.11.06, DDT PI: Kishalay De):

ACIS-S imaging (fallback accretion onto a newly formed black hole)

Results

Observational facts by JWST/NIRSpect & MIRI:

- **Strong silicate absorption feature** at ~ 10 μm was detected.
- **CO & CO2 absorption features** were detected.
- NIR flux density was decreased by a factor of **5000** or **50**.
- **Mid-infrared (>10 μm) flux density was almost unchanged**.

1D radiative transfer modeling (DUSTY) couldn't explain the SED.

- 10 μm absorption required a high optical depth ($\tau_V \approx 23.2$).
- Such optical depth cannot explain the flux density around 1 μm.
- Asymmetric eject distribution was strongly favored.

Discussion

M31-2024-DS1 is not in line with several failed SN scenarios.

A failed SN event will produce a bright optical outburst, but such outburst wast not observed for M31-2024-DS1 (Lovegrove & Woosley, 2013)

The mid-infrared flux density of the remnant did remain for 10 years, although the accretion rate will decline (Perna et al., 2014)

No X-ray emission was detected either in the archival images (2015 & 2020) and the Chandlar observation in 2024 (Perna et al., 2014)

It seems difficult to distinguish observationally a failed supernova remnant from a stellar merger (luminous red nova). Observing a "disappearing star" alone provides insufficient evidence for failed supernova classification. Further monitoring over the coming years and theoretical studies are required.

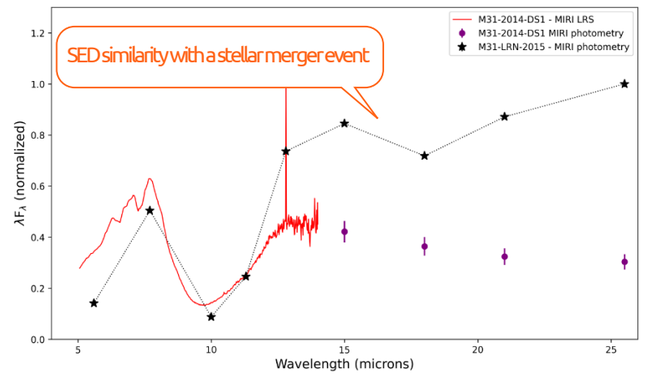

Figure 3 of Beasor et al. (2026): :SED comparison with a stellar merger event

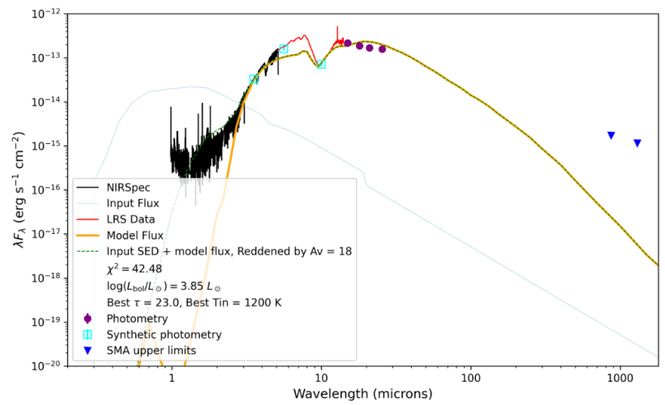

Figure 4 of Beasor et al. (2026): DUSTY modeling

The fate of the failed supernova candidate M31-2014-DS1

Emma R. Beasor[1]★, Nathan Smith[2], Jeniveve Pearson[2], Bhagya Subrayan[2], Edo Berger[3], David J. Sand[2], and Jay Strader[4]

[1]Astrophysics Research Institute, Liverpool John Moores University, IC2, 146 Brownlow Hill, Liverpool, L3 5RF, UK
[2]Steward Observatory, University of Arizona, 933 North Cherry Avenue, Tucson, AZ 85721-0065, USA
[3]Center for Astrophysics | Harvard & Smithsonian, 60 Garden Street, Cambridge, MA 02138, USA
[4]Department of Physics and Astronomy, Michigan State University, East Lansing, MI 48824, USA

Accepted XXX. Received YYY; in original form ZZZ

ABSTRACT

The fate of massive stars above $20M_{\odot}$ remains uncertain. Debate persists about whether they die as supernovae (SNe), or if they collapse directly into black holes (BHs) with little or no optical outburst — so-called "failed supernovae". The source M31-2014-DS1 experienced an optical outburst in 2014 and has remained faint at visual wavelengths since then. Due to its persistent faintness, it has been proposed as a failed SN candidate. We present new observations of this candidate obtained using the James Webb Space Telescope (JWST), the Submillimeter Array (SMA), and Chandra. The *JWST* observations demonstrate that a luminous mid-infrared source persists at the same location a decade after the star faded at visual wavelengths. We model its current spectral energy distribution (SED) as a dust-enshrouded star. No X-ray emission is detected, disfavoring the hypothesis that the late-time luminosity is powered by accretion onto a BH. We find that the remaining source is highly obscured by an asymmetric distribution of circumstellar dust, making it difficult to quantify its physical properties using spherically symmetric radiative transfer codes. The dust geometry requires that the inferred bolometric luminosity is only a lower limit, as a significant fraction of the central source's radiation may escape without being reprocessed by dust. We discuss the implications of these findings in the context of failed SN models and consider the potential overlap with signatures expected from a stellar merger, which also seems to provide a plausible explanation of this source.

Key words: black holes – circumstellar matter – stars: mass-loss – stars: massive –

1 INTRODUCTION

In the canonical view of single-star evolution, solar metallicity stars with initial masses above $8M_{\odot}$ are expected to end their lives as supernovae (SNe) and leave behind a neutron star (NS) remnant (Heger et al. 2003). However, the existence of stellar-mass black holes (BHs) requires that some massive stars collapse further to make remnants more massive than NSs. This possibility has inspired suggestions that some of these massive stars may fail to explode successfully, disappearing from view rather than producing a bright transient (Kochanek et al. 2008). The factors determining how a massive star ends its life are complex, and likely not a simple function of initial mass (e.g. Sukhbold et al. 2018; Laplace et al. 2025).

Serendipitious pre-explosion imaging of the progenitors to supernovae (SNe) has played an important role in our understanding of how massive stars end their lives, as it is arguably the most direct method of linking SNe to their progenitors. It was through this direct detection technique that red supergiants (RSGs) were confirmed as the most common progenitors to Type II-P supernovae (e.g. Smartt et al. 2004; Maund & Smartt 2005; Fraser 2016). However, as the sample of Type II-P SNe with pre-explosion imaging increased, some authors noted an apparent lack of progenitors with inferred initial masses above 16-18 $M_{\odot}$, despite the existence of RSGs in nearby stellar populations that are thought to have initial masses in this range (Smartt et al. 2009; Smartt 2015). The statistical significance of the putatively missing high-mass progenitors is controversial, however, and has been widely debated (Davies & Beasor 2018; Davies & Beasor 2020a,b; Kochanek 2020; Beasor et al. 2025; Healy et al. 2024, among others). In addition to the low statistical significance of missing progenitors, there are a number of other caveats to the RSG problem. For one, the initial masses are derived using stellar evolution models, which are highly uncertain at late phases (e.g., Renzo et al. 2017; Zapartas et al. 2021; Eldridge & Stanway 2022). Secondly, progenitor luminosities are typically estimated using only the HST F814W filter, which can underestimate the true luminosity (Beasor et al. 2025). Third, in the original RSG problem analysis (Smartt et al. 2009), no correction was applied for circumstellar dust extinction (Walmswell & Eldridge 2012), which can further bias progenitor luminosities downward. Finally, most studies have focused on Type II-P supernovae, but higher-mass RSGs may preferentially explode as other SN types, such as Type IIn or stripped-envelope SNe (e.g., Smith et al. 2011), which could change the inferred progenitor mass distribution.

The lack of high-mass RSG progenitors has been interpreted by some as a smoking gun suggesting that the most luminous RSGs collapse to form a BH with little or no explosion (e.g. Smartt et al. 2009; Smartt 2015). Following this observational result, theoretical work identified possible regimes of stellar mass which seem to be

★ E-mail: E.R.Beasor@ljmu.ac.uk

harder to explode in simulations, leading to the suggestion that there are 'islands of explodability' (e.g. Sukhbold et al. 2018; Couch et al. 2020; Ebinger et al. 2019; Laplace et al. 2025), in which a high mass star is less likely to successfully explode[1]. Some recent work has suggested that these studies overestimate the likelihood of direct collapse in the RSG mass regime (e.g. Burrows et al. 2024, 2025). There is also support from the gravitational wave side, with the mass range of detected BHs implying a lower initial-mass transition from neutron star (NS) to BH (e.g. Schneider et al. 2025), as well as some works claiming that there is no lower BH mass gap at all (Ray et al. 2025).

All of this has motivated the search for the observational signature of a failed SN. Generally, teams search for failed SNe the same way they search for successful SNe; by searching for sudden changes in brightness. In the failed SN searches, however, a progenitor star must first be detected in multiple epochs before it can be seen to fade or disappear entirely. As such, the search is limited to very nearby galaxies (Kochanek et al. 2008).

There are two key challenges in identifying failed SNe. First, massive stars might fade for reasons other than collapse to a BH, so there may be other types of fading stars that masquerade as failed SNe (see Jencson et al. 2022; Beasor et al. 2024). And second, from various theoretical predictions, it is unclear exactly what a failed SN should look like. There is a wide range of theoretical predictions for their observable characteristics. For one, it has been suggested that failed SNe may undergo a direct collapse and have no visible signature beyond disappearing (Kochanek et al. 2008). Lovegrove & Woosley (2013) suggest the collapse of a massive star may be accompanied by lingering infrared emission, potentially lasting for several years, but would not expect an optical transient. Perna et al. (2014) suggest a failed supernova would produce a dim but prolonged optical transient due to long-lasting fallback accretion onto the BH, while Antoni & Quataert (2023) find the collapse of a massive star into a BH would produce a bright transient due to the luminosity from rapid accretion. The inherent ambiguity in the wide range of current theoretical predictions makes it challenging to uniquely identify a fading star as a failed SN, especially since other types of events like stellar mergers may look similar (see discussion in Beasor et al. 2024).

The most compelling candidate of a failed SN to date had been N6946-BH1 (hereafter BH1), first identified by Adams et al. (2017). The progenitor to the source was initially interpreted as an RSG with an initial mass of $\sim 30 M_{\odot}$, which then underwent an optical outburst before fading by a factor of 10 over 3000 days. However, it has also been noted that a number of observations prior to the outburst were more similar to those expected for stellar mergers (e.g. Beasor et al. 2024). For one, the source had appeared to redden over the preceeding 5 years from the colors of a warm supergiant to those of a cool, red supergiant (e.g. Adams et al. 2017; Humphreys 2019; Beasor et al. 2024)[2], similar to known stellar merger event V1309 Sco (Shara et al. 2010; Mason et al. 2010; Stępień 2011). Further, some models suggest the optical outburst of BH1 may have been too faint to be from a failed SN (Antoni & Quataert 2023). Finally, there remains an IR bright source at the position of BH1. As discussed in Beasor et al. (2024) and Kochanek et al. (2024), it is not possible to distinguish between the failed SNe and merger scenarios without further epochs of data.

There have been other proposed candidates for failed SNe, including M101-OC1, a blue supergiant, (Neustadt et al. 2021), N3021-OC1, a yellow supergiant (Reynolds et al. 2015) and PHL293B, a luminous blue variable (LBV Allan et al. 2020). We note that neither of these objects have been considered to be strong candidates for failed SNe and have not been followed up with mid-IR facilities to confirm their disappearance. There is emerging evidence that some massive stars undergo major dimming events before re-brightening at later epochs, including M51-DS1 (Jencson et al. 2022) and Betelgeuse (Montargès et al. 2021). The cause of these dimming events is unclear, but these studies show that any failed SNe candidate needs to be followed up at later times to confirm the source has not re-appeared.

Recently, De et al. (2024b) identified a new failed SN candidate in M31. This new candidate was identified by searching for outbursts in data from the NEOWISE mid-infrared survey (Mainzer et al. 2014) in the direction of Andromeda (M31). De et al. identified a source that brightened by 50% in the mid-IR over two years beginning in 2014. For the subsequent thousand days after the MIR brightening started, the inferred total luminosity remained nearly constant, before fading below the progenitor flux over the next year, and NEOWISE data showed it continued to fade through 2022. During this time the optical flux from the source faded by a factor of ≥ 100 between 2016 and 2019. The authors dubbed the candidate M31-2014-DS1, and claim its moderate outburst and subsequent fading can be explained by the infall of the stellar envelope onto a newly formed black hole. The progenitor star was interpreted as a hydrogen-poor supergiant, with an inferred luminosity of $\log(L/L_{\odot}) = 5$ and effective temperature of ~ 4500K (De et al. 2024b). We note that there are a number of SN with detected progenitors at a similar luminosity (see Fig. 6 in Beasor et al. 2025, and references within), implying that stars at this luminosity are able to yield successful explosions in many cases. Also, if the star is a stripped-envelope progenitor (as modelled by De et al. 2024b), some theoretical work suggests these stars should be easier to explode than their non-stripped counterparts (e.g. Laplace et al. 2025). Here, we present new *JWST* and *SMA* observations of M31-2014-BH1 and model the data using `DUSTY` modelling. In Section 2 we discuss the near-IR, mid-IR, radio and X-ray data. In Section 3 we discuss the dust shell model fitting. In Section 4 we discuss current failed SN models. In Sections 5 & 6 we discuss whether the observations of M31-2014-DS1 are consistent with either the failed SNe model or stellar mergers.

2 DATA

2.1 JWST

The position of M31-2014-DS1 was observed by the James Webb Space Telescope (JWST) on November 28 2024. The data included NIRSpec (Jakobsen et al. 2022) and MIRI LRS (Rieke et al. 2015) spectra as well as photometry from and MIRI, taken under DDT Program 6809 (PI: De, De et al. 2024a).

Imaging was taken in MIRI filters F1500W, F1800W, F2100W and F2500W, see Fig. 1. We identified the source using the bluest MIRI filter and registered all images to a pre-disappearance HST image of the field, which served as the reference position. Alignment was done manually by eye, allowing us to confirm that the same source was clearly detected in all subsequent observations. Following the method described in Pearson et al. (2025), PSF photometry of the MIRI ob-

[1] We note that this result comes from 1-D stellar evolution modeling, and explodability is determined by adopting a criterion for the progenitors core compactness. The use of this simple compactness parameter to determine whether or not a progenitor will explode is debated, and the core structure may be more complicated than 1-D stellar evolution models predict.

[2] We note that the reddening timescale may be longer, but there are no Spitzer data before 2004.

Filter	Flux ($\times 10^{-6}$ mJy)
F1500W	1.0902 ± 0.0059
F1800W	1.1295 ± 0.0136
F2100W	1.1718 ± 0.0148
F2550W	1.3342 ± 0.0137

Table 1. Flux measurments for MIRI photometry.

Observation Date	On-source Time (minutes)
250219_04:11:12	79
250218_03:56:04	130
250217_03:46:50	139
250216_04:05:22	79

Table 2. SMA observations.

servations was done using `space_phot`[3] (Pierel 2024; Pierel et al. 2024) on the Level 2 products. This is done by fitting the supernova's PSF in each of the Level 2 CAL files using WebbPSF (Perrin et al. 2012, 2014, version 1.2.1) models. Given the low signal to noise detection of the source in the F2550W individual exposures, for this filter we instead do PSF photometry on the Level 3 stacked images. For photometry on the Level 3 products, `space_phot` uses temporally and spatially dependent Level 2 PSF models from WebbPSF, and drizzles them together to create a Level 3 PSF model. The resulting MIRI photometry is listed in Table 1 and MIRI images are shown in Figure 1.

The NIRSpec data were obtained via the MAST data archive (Pence et al. 2019) and were processed using the standard data reduction pipeline. Data were taking in the fixed slit mode using the G140H/F100LP, G235H/F170LP and G395H/F290LP gratings resulting in spectral coverage bwteeen 1.0 μm and 5.0 μm. The 1-D spectra were extracted using the `spec1d` function from `specutils` (Smith et al. 2020). We then smoothed the spectrum using a moving average and a window size of 5 pixels.

The JWST/MIRI LRS data were retrieved from the MAST archive and processed using the standard JWST pipeline which utilizes the `calwebb_detector1` and `calwebb_spec2` stages to correct detector artifacts and perform calibration (Bushouse et al. 2022). The spectral range covered is 5 to 14μm. One-dimensional spectra are extracted using `extract_1d` summing the flux within a defined spatial aperture along the source trace, optimizing flux recovery. Background subtraction was carried out by estimating the background flux from regions adjacent to the source trace and subtracting it from the flux measured within the extraction aperture.[4]

2.2 Radio

The Submillimeter Array (SMA) observations were obtained as part of the Large Project POETS (Pursuit of Extragalactic Transients with the SMA; project 2022B-S046, PI: Berger). The observations are summarized in Table 2. During these observations, the SMA was tuned to a local oscillator (LO) frequency of 225.5 GHz, providing spectral coverage at 209.5˘221.5 and 229.5˘241.5 GHz. Across all nights, 3C84 was observed as a bandpass calibrator, Uranus was observed as a flux calibrator, and J0136+478 was observed as a gain calibrator, with a 12-min cycle time cadence.

Analysis of the data was performed using the SMA COMPASS pipeline (G. K. Keating et al. 2025, in prep.), which flags spectral data based on outliers in amplitude when coherently averaging over increasing time intervals for each channel within each baseline, as well as baselines where little to no coherence is seen on calibrator targets. Flux calibration was performed using the Butler–JPL–Horizons 2012 (Butler 2012) model for Uranus. The data were imaged, and deconvolution was performed via the CLEAN algorithm (Högbom 1974).

[3] `space_phot` version 0.2.5 `space-phot.readthedocs.io`
[4] `https://github.com/STScI-MIRI/LRS_ExampleNB/blob/main/miri_lrs_pipeline_extraction.ipynb`

We do not detect emission at the location of M31-DS1 in any of our observations, with a combined rms noise level of 0.5 mJy.

2.3 X-ray

X-ray observations at the position of M31-2014-DS1 were taken with ACIS-S (Garmire et al. 2000) on board the *Chandra* X-ray observatory under DDT program 25509003 (PI: De) on 6 November 2024. The data were reprocessed with `CIAO` v4.17 and CALDB 4.12.2. Source counts were extracted from a 2″ circular aperture centered on the optical position of M31-2014-DS1, and the background was estimated from a concentric annulus with inner and outer radii of 5″ and 10″. Spectra and instrumental responses were generated using `specextract`. The on source time was 10734.8 s and no counts were detected in either the source or background regions, leading to a 90% confidence upper limit of $< 2.1 \times 10^{-4}$ counts s^{-1}.

To convert the observed count rates into fluxes, we assumed an absorbed power-law spectrum with $N_{\rm H} = 1 \times 10^{23}$ cm^{-2} and photon index $\Gamma = 1.7$. The adopted value of $N_{\rm H}$ reflects the expected high intrinsic extinction toward the source (Bahramian et al. 2015). Under these assumptions, we derive an upper limit on the X-ray luminosity of $L_X < 2.96 \times 10^{35}$ erg s^{-1} in the 0.5–7.0 keV band.

3 THE SPECTRAL ENERGY DISTRIBUTION

The JWST spectral energy distribution (SED) of M31-2014-DS1 is shown in Fig. 2. The NIRSpec data reveal that at short optical/near-IR wavelengths, a faint, red source persists at the position of the failed SN candidate whereas MIRI data reveal a luminous mid-IR source that peaks around 8-10 μm, which has almost the same 20 μm flux as the progenitor. At the shortest wavelengths, there is also a slight uptick in the flux toward shorter wavelengths (~ 1-2mum) extending past the observed wavelength range, perhaps suggesting the presence of a lingering optical source.

The mid-infrared spectrum exhibits a strong silicate absorption feature at 10 μm, indicative of a substantial amount of cool oxygen-rich circumstellar dust in absorption along the line of sight. In typical red supergiants undergoing standard mass-loss, this feature generally appears in emission (e.g. Beasor et al. 2020). However, in cases with large quantities of circumstellar material—particularly when the dust distribution is asymmetric—the silicate feature can instead appear in absorption, as observed in objects such as IRAS 01304+6211, an OH/IR object in Cassiopeia (Kemper et al. 2002) and WOH G64, a supergiant known to have a non-spherical dusty torus (Ohnaka et al. 2008). Karambelkar et al. (2025) present JWST observations of luminous red novae several years after their outbursts, including M31-LRN-2015, claimed to be a merger product that show strong silicate absorption features in its spectra, see Fig. 3. Additional absorption features are present at 4.3 and 4.5 μm, likely associated with CO and possibly CO_2, further supporting the presence of a significant amount of dusty molecular material (Wood et al. 1989; Cox et al. 1988; Cami et al. 1997). We also present the pre-disappearance spectral energy

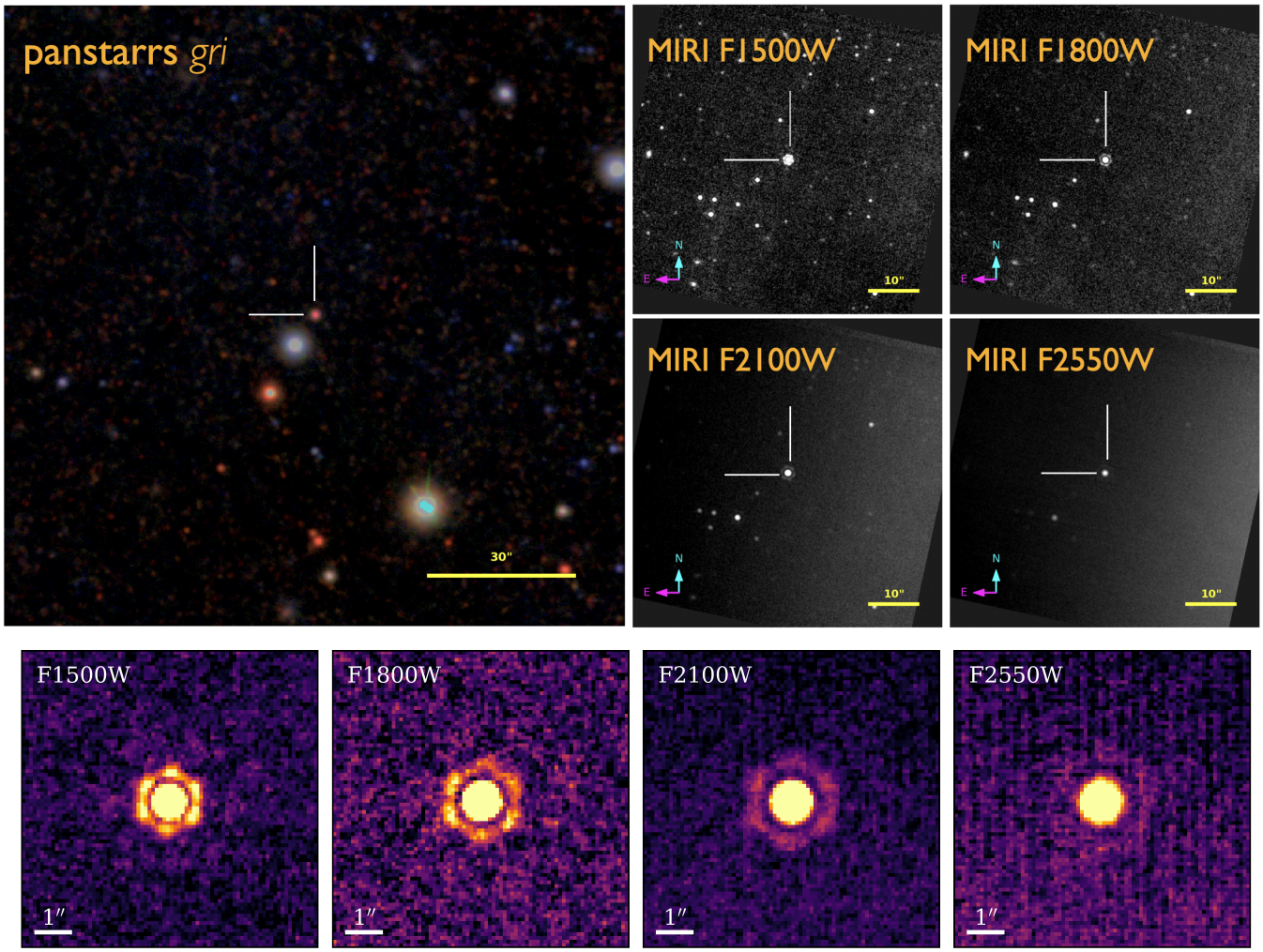

Figure 1. *Top left:* Finder chart for M31-2014-DS1 using Pan-starrs *gri* photometry. *Top Right:* JWST/MIRI imaging of the source remaining at the position of M31-2014-DS1. *Bottom:* PSFs in each JWST MIRI filter.

distribution (SED) of the progenitor star for comparison, as well as HST data from 2022, see Fig. 2.

When comparing the photometry of the progenitor system to the new JWST data there are clear differences, see Fig. 2. Firstly, the near-IR flux ($\lambda < 2\mu$m) has faded by a factor of ~5000 at 1μm and by a factor of 50 since 2022. At longer wavelengths, there is still a loss of flux compared to the 2012 emission, but at a much lower factor. At $\lambda \geq 10\mu$m, the flux has remained constant. The unchanged flux at $\lambda > 10\mu$m is consistent with the system increasing in extinction (likely due to dust production), which dramatically reduces the flux at shorter wavelength and causes the silicate feature to go into absorption rather than emission. The longer wavelength observations are not consistent with an overall reduction in bolometric luminosity of the system.

If the circumstellar dust surrounding DS1 is asymmetric (see below) then the integrated IR luminosity is only a lower limit to the source's true luminosity, since this method relies on the assumption that any radiation lost to extinction at shorter wavelengths is re-emitted at longer wavelengths. This assumption only holds true for stars with spherically symmetric dust shells. As such, any luminosity estimate derived from such modeling would be a lower limit, as optically thick, asymmetric dust configurations could obscure significant amounts of flux along certain lines of sight, whereas the light being re-emitted at longer wavelengths may be only a small fraction of the total intrinsic luminosity. This hypothesis requires that an Earth-based observer is viewing the system from a vantage point at latitudes near the equatorial plane.

3.1 DUSTY modeling

We explore models for the source using the 1-D DUSTY radiative transfer code, which solves the radiative transfer equations assuming spherical symmetry. For the dust shell models used in this work, we used MARCS model atmosphere models (Gustafsson et al. 2008) at $T_{\rm eff}$ = 4400 to match the inferred temperature from De et al. (2024b). For the dust itself we use the silicate-rich composition defined by Draine & Lee (1984) and vary the grain size from 0.1 to 1.0μm in steps of 0.1. We allow the inner dust temperature (i.e. the temperature at the innermost radius of the dust shell) to vary between 100K to 1200K in steps of 100K. We chose 1200K as a maximum $T_{\rm in}$ value since silicate dust sublimates at temperatures above this (Hanner 1988).

For fitting the models, we convolve the model spectrum from

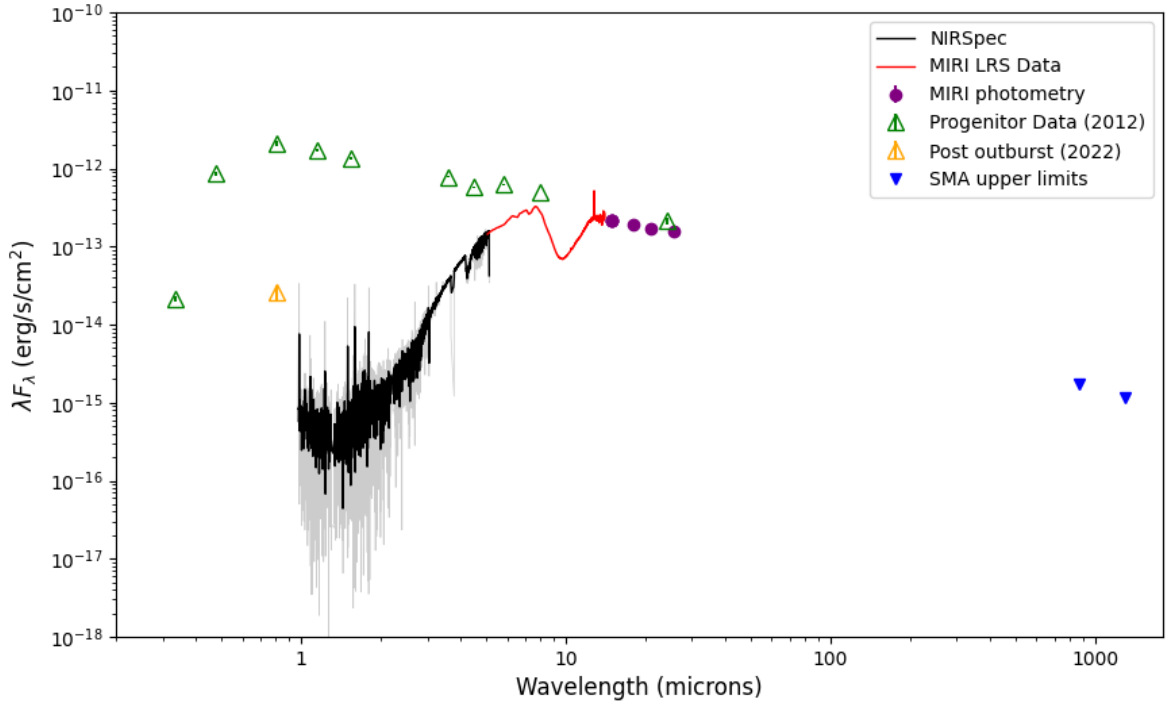

Figure 2. The SED of the remaining source at the position of M31-2014-DS1 obserevd by JWST and SMA. The NIRSpec data have been smoothed using a moving average with a window size of 5 pixels (black solid line). We also show the SED of the progenitor star (green triangles) as well as post-outburst data (orange triangle).

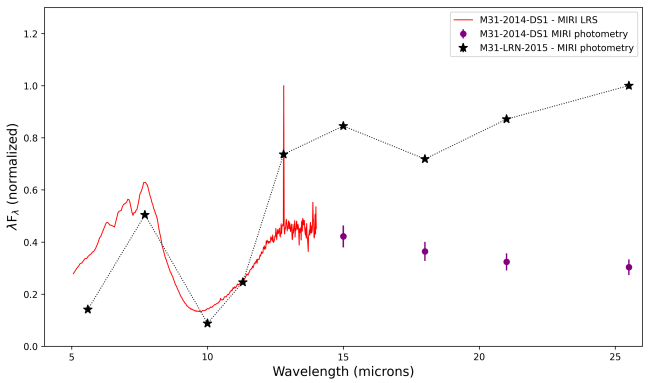

Figure 3. Comparison between the mid-IR appearance of M31-2014-DS1 and luminous red nova M31-LRN-2015 (Karambelkar et al. 2025). The fluxes have been normalised for direct comparison.

DUSTY with the JWST filter profiles for the MIRI photometry. We also convolve the NIRSpec and MIRI LRS spectrum with filter profiles for NIRCAM/F360M, MIRI/F560W, and MIRI/F1000W to create synthetic photometry and improve the fit at shorter wavelengths.

We found that no single DUSTY model could provide a good fit to the full SED of M31-2014-DS1, see Fig. 4. When attempting this, it is possible to fit the SED well at λ>2μm, but at shorter wavelengths there appears to be a hotter, separate component. As noted above the strong silicate absorption feature and the presence of CO and CO2 features strongly suggest the dust is not spherically symmetric, and so it is expected that using a spherically symmetric radiative transfer code such as DUSTY will fail to fit the JWST data. We instead model the SED using two components to mimic the effect that an asymmetric dust distribution would have on the output SED. We begin by fitting only the cooler component of the SED with DUSTY as described above. To model the NIRSpec data ($\lambda < 2\mu$m) we take the input model SED ($T_{\rm eff}$ = 5000K, blue line) and redden it by 20 magnitudes using the G23 extinction law (Gordon et al. 2023). We then linearly combine this model component with a scaled-down version of the input spectrum to create a compsite model of the full SED (green dashed line).

We show our best-fit model in Figure 4. The emergent luminosity of the model, after applying 18 mag of extinction, is $\log(L/L_\odot)$ = 3.85, and we again note that due to the likely asymmetric nature of the dust this is a lower limit on the true luminosity of the system. We find that a high optical depth, τ_V = 23.2 is required to fit the silicate feature in absorption, corresponding to a total dust mass of $0.004 M_\odot$. There may be cold dust shells at larger radii that do not effect the near and mid-IR SEDs.

4 DISCUSSION

4.1 Failed supernova models

The idea that a massive star could collapse into a black hole without producing a successful supernova explosion was first proposed by Nadezhin (1980), who suggested that the sudden loss of gravitational

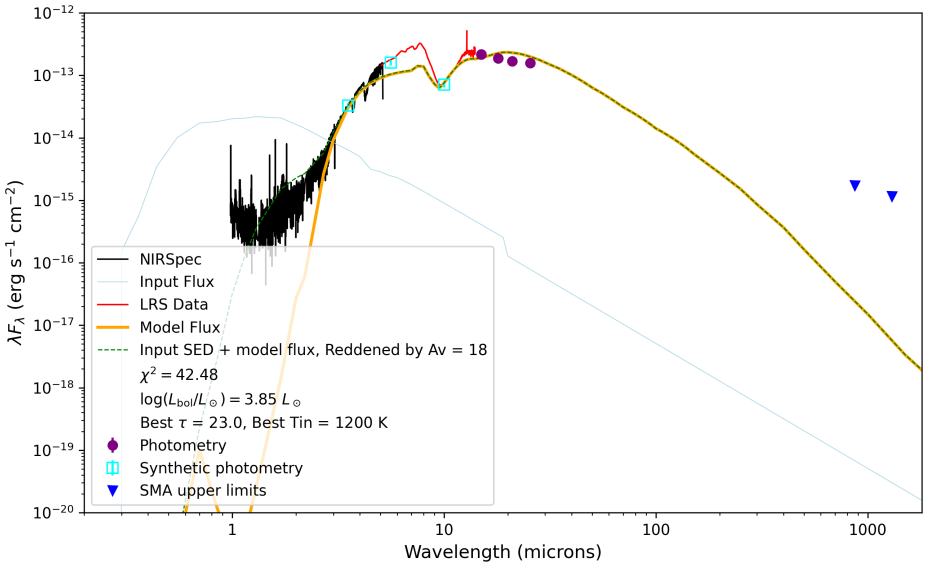

Figure 4. Fit to the JWST data with DUSTY modeling and an additional reddened component.

binding energy due to neutrino emission during core collapse could unbind the loosely bound hydrogen envelope of a red supergiant. This early insight laid the foundation for later theoretical work by Woosley & Weaver (1986) and Fryer et al. (1999), who modeled the outcomes of core collapse in massive stars. While these studies often focused on successful explosions or gamma-ray bursts (GRBs) via the collapsar mechanism, they noted that in cases lacking sufficient rotation or involving extended stellar envelopes, the collapse could fail to launch a strong explosion, resulting instead in a direct black hole formation with minimal electromagnetic emission.

Building on Nadezhin (1980), Lovegrove & Woosley (2013) modeled the low-energy transients expected when an RSGs envelope is ejected purely by neutrino-driven mass loss, predicting a faint, short-lived optical signal. More recent work by Ott et al. (2011) and O'Connor & Ott (2011) introduced the "compactness parameter" as a diagnostic for identifying which stellar progenitors are most likely to fail, providing a quantitative framework for predicting black hole formation in core-collapse events (see also Sukhbold et al. 2018).

The concept of failed SNe gained further relevance with the emergence of the "red supergiant problem," which noted a lack of high-mass progenitors ($\gtrsim$18–20 $M_\odot$) in pre-explosion imaging (Smartt et al. 2009; Smartt 2015). To test the failed SN hypothesis observationally, Kochanek et al. (2008) proposed a long-term monitoring survey of nearby galaxies to search for massive stars that disappear without a bright explosion. But the expected observational signature of a failed SN is unclear. Below, we discuss various models that make predictions for the observable features of failed SNe, as well as the bespoke model proposed to explain the observations of M31-2014-DS1.

4.1.1 *Lovegrove & Woosley 2013*

In this work, the authors used hydrodynamical models of 15 and 25$M_\odot$ progenitors with weakly bound envelopes (i.e. RSGs) to explore the fates of SN progenitor stars following the sudden loss of 0.2 - 0.5$M_\odot$ of gravitational mass from their centres via neutrinos. They find that this sudden loss of mass can generate a very weak outgoing shock. For an RSG progenitor, this weak shock is able to eject the hydrogen envelope and form a very weak optical transient with a total kinetic energy of $\sim 10^{47}$ erg and an ejection velocity of only 100km/s. The models suggest such an event would result in faint, red transients that could last up to 1 year, peaking at a luminosity of approximately 10^{39} erg/s. In-fact, these events would appear similarly to luminous red novae (LRN), though with lower ejection speeds. The observations of M31-2014-DS1 show a lack of any bright optical outburst as predicted by this model.

4.1.2 *Perna et al. 2013*

While not a study of failed supernovae, in Perna et al. the appearance of compact objects surrounded by disks was explored. They find that for SN that leave behind BHs, the presence of disks is ubiquitous (Perna et al. 2014). For weak explosions (the case most similar to a failed SN), the outer envelope may remain bound and allow for the formation of a disk.

The expected duration of associated X-ray emission varies significantly depending on the properties of the fallback disk. For compact, hyper-accreting disks—such as those forming from rapidly rotating, low-metallicity stars typically associated with long-duration GRBs—the transient emission (including X-rays) is expected to last no more than several hundred seconds. In contrast, if the fallback material forms a longer-lived disk, the emission may persist for much longer. This scenario could arise from more slowly rotating but highly extended progenitors, such as supergiant stars, where the large stellar radius compensates for the lower rotational velocity by contributing sufficient angular momentum to sustain an extended accretion disk. or through weak/anisotropic explosions that allow outer layers to remain bound, and the resulting phenomena can have much longer durations. Early phases of these long-lived disks, even if no longer neutrino-cooled, could produce weaker, very long gamma-ray transients, which would likely have associated X-ray emission lasting for several days. For older, long-lived disks around BHs, sig-

nificant X-ray luminosity, comparable to that of anomalous X-ray pulsars (AXPs) or modeling ultraluminous X-ray sources (ULXs), is expected to persist for much longer periods, potentially on the order of 10^4 to 10^5 years. Therefore, the X-ray emission from fallback onto a newly formed black hole can range from brief transient bursts to very long-lasting, persistent sources.

Basinger et al. (2021) suggested that observing X-rays may not be a useful diagnostic for failed SNe as the X-rays may be absorbed via the envelope of the collapsed star. For another failed SN candidate, N6946-BH1, no X-rays were detected by Chandra X-ray telescope (Basinger et al. 2021). No X-rays were detected at the position of M31-2014-DS1 in archival data (De et al. 2024b) or more recent observations (this work, see Section 2).

4.1.3 Antoni & Quataert 2023

Antoni & Quataert (2023) explored the fate of massive stars that fail to produce a successful SN. Specifically, they model a $16.5 M_\odot$ RSG and a lower mass yellow supergiant (YSG) using the `athena++` hydro code. In each case, a large fraction of the stars' envelope would collapse into the core and produce a BH. Importantly, the accretion luminosity from the infall of the envelope would lead to the production of a visible transient.

In this model, a failed SN would appear similar to a luminous red nova (LRN), with a luminous red plateau lasting hundreds of days. The RSG model produces a plateau length of ~ 500 days, while the YSG plateau lasts 200 days.

The failed SN candidate N6946-BH1 is also noted as being qualitatively similar to these events, although the models predict a somewhat higher explosion energy and luminosity than observed for N6946-BH1 if its progenitor was a $25 M_\odot$ RSG. The authors also find that an $11.2 M_\odot$ YSG would produce a luminous transient significantly brighter than that of N6946-BH1 (see Fig. 13 within). Given the presumed outburst for M31-2014-DS1 was even less luminous than that of BH1, the observations of M31-2014-DS1 do not fit this model.

4.1.4 De et al. 2024b

The observations of M31-2014-DS1 appear to show a scenario that is not fully consistent with any of the aforementioned BH formation models. For one, there is a lack of any bright optical outburst as predicted by both Lovegrove & Woosley (2013) and Antoni & Quataert (2023). Secondly, the progenitor itself differs from the typically assumed most-likely failed SNe progenitor. The progenitor to M31-2014-DS1 appeared as a H-depleted YSG progenitor, rather than a H-rich RSG. De et al. (2024b) attempt to reconcile the lack of a bright outburst and a failed SN by proposing an intermediate case of a weak impulsive ejection that caused enough additional extinction from new dust formation to counteract the luminosity. They find that the luminosity and duration of any missed outburst is limited to $\leq 10^5 L_\odot$ and ≤ 70 days.

Lovegrove & Woosley (2013) attribute the lingering flux from a failed SN to H-recombination in the ejected envelope. In the scenario laid out by De et al. (2024b), there is also H-recombination in addition to flux coming from accretion onto the BH. However, the progenitor system was identified as a hotter, H-depleted star (based on the progenitors' position on the HR diagram), meaning a lower-mass H envelope than studied in the Lovegrove & Woosley (2013) scenario. In addition, there is a 10^{48} erg shock into the envelope which unbinds only $0.1 M_\odot$ of material. The authors suggest this weak shock would produce a brief, luminous optical transient that would be easy to miss given the photometric coverage of the source. The authors also suggest that convective turbulence during the final stages of evolution lead to an angular momentum that can suppress direct accretion.Combined these effects lead to less efficient accretion (only 1% of infalling material is likely to accrete directly) and a longer fading time.

The model also addresses the lack of detected X-ray emission from the accreting black hole. No X-rays were found in archival Chandra, Swift, or NuSTAR observations taken between 2015 (*Chandra, NuStar*) and 2020 (*Swift*). De et al. (2024b) explain this by proposing that the newly formed black hole is heavily enshrouded by both the unbound ejecta and a dense outflow from the inefficient accretion process. This material creates a high column density that absorbs any X-rays, preventing their detection. The authors predict that this obscuring material will dissipate over time, and the source may become transparent to soft X-rays within the next several years to decades, potentially revealing the nascent black hole through future observations. At the time of the most recent *Chandra* observations, taken in November 2024, the source has still not been detected, see Section 2.

5 IS M31-2014-DS1 A FAILED SUPERNOVAE?

In the previous sections we discussed the predicted observational signatures for a failed SN from a number of models. Ultimately, the only model that appears to fit the data is that of De et al. (2024b). This bespoke model was constructed specifically to reconcile the observations of M31-2014-DS1 with the failed supernova scenario, proposing that a weak shock in a hydrogen-depleted progenitor star could explain the lack of a bright optical outburst.

However, several observational details challenge the interpretation of M31-2014-DS1 as a failed SN. Ten years after the initial mid-infrared brightening in 2014, JWST observations reveal a persistent, luminous infrared source at its location. The long-wavelength flux ($\lambda \geq 10\,\mu$m) has remained nearly constant since 2012, which is inconsistent with a simple, overall reduction in the system's bolometric luminosity. In a failed SN scenario where a BH is formed, the luminosity from fallback accretion is expected to decline over time as the accretion rate decreases. The fact that the source's mid-IR flux has not faded significantly, and that its current luminosity is estimated to be around 7–25% of the progenitor's, complicates the collapse model.

Furthermore, no X-rays have been detected from the position of M31-2014-DS1 in archival Chandra observations from 2015, Swift observations from 2020 or Chandra observations from 2024. This is in contention with models that predict long-lasting X-ray emission from fallback accretion onto a new black hole (e.g. Perna et al. 2014), potentially for thousands of years. Although the non-detection could be explained by heavy obscuration from the collapsing star's envelope or newly formed dust (Basinger et al. 2021; De et al. 2024b), the combination of a lingering, steady infrared flux and a lack of detectable X-rays more than 10 years after the suggested collapse of the star would argue against a failed SN.

6 IS M31-2014-DS1 A STELLAR MERGER?

As demonstrated in the previous section, M31-2014-DS1 does not fit any of the standard predictions for a failed SN. The only model that successfully matches the observations is the custom model constructed for this object from De et al. (2024b). While the authors do

make a prediction for the fate of the source, i.e. that it will continue to fade below it's pre-disappearance luminosity, this alone is not sufficient in confirming the failed SN scenario. A difficulty with such revised failed SN models is that by invoking long-lasting accretion to explain the lingering late-time luminosity, one pushes the observed expectations to a regime that becomes difficult to distinguish from a range non-terminal outburst scenarios, such as dusty shell ejection and stellar merger events. There have been a number of observed eruptive transients that have faded in the optical but remained bright in the infrared as they became dust obscured, many of which are interpreted as stellar merger events (e.g. V1309 Sco; (Tylenda et al. 2011), V4332 Sgr; (Kamiński et al. 2010), M85 OT2006-1; (Rau et al. 2007), M31 RV; (Bond et al. 2011), NGC 4490-OT2011; (Smith et al. 2016), M101 OT2015-1; (Blagorodnova et al. 2017), SPIRITS IR-transient sample; (Jencson et al. 2019), JWST-studied mergers (AT2021blu, AT2021biy, AT2018bwo, M31-LRN-2015); (Karambelkar et al. 2025)).

In the binary merger scenario, the observed luminosity of any progenitor system can have a significant contribution from shock heating of the outflow from the inspiral phase, raising the apparent luminosity (Pejcha et al. 2017; Smith et al. 2018). In other words, the observed yellow supergiant progenitor luminosity is not the nuclear burning luminosity of the system, but is enhanced by the inspiral phase. This luminosity is not indicative of an initial mass using the usual mass-luminosity relations from single star models; the true stellar luminosity and corresponding initial mass are lower. As such, converting from an observed luminosity to an initial mass would lead to an overestimate of the progenitor mass (see Beasor et al. 2024). In addition, this means that the apparent drop in luminosity observed for both M31-2014-DS1 and N6946-BH1 is not necessarily entirely due to extinction from an ejected envelope or dust production, since the luminosity may naturally decrease as the extra luminosity from the inspiral phase is shut off – the system may actually be returning to it's quiescent radiative luminosity. This pre-merger increase in luminosity due to inspiral was observed for the merger system V1309 Sco (Tylenda et al. 2011).

Kashi & Soker (2017) propose that stellar mergers, particularly those classified as Type II intermediate-luminosity optical transients (ILOTs), can exhibit such behavior due to anisotropic mass loss. In their model, a strongly interacting binary ejects mass preferentially into the equatorial plane, forming a dense, optically thick dust torus that obscures the central source from equatorial viewing angles. Observers in these directions predominantly detect reprocessed radiation from the polar regions, leading to a dramatic reduction in optical flux (down to ~10% of its original value), while the infrared emission remains strong due to dust heating. It is important to recognize a clear selection effect that favors the identification of edge-on systems in surveys searching for disappearing stars. In such merger events, the observed fading of the progenitor is typically caused by obscuration from an equatorial dust torus. Consequently, merging systems are more likely to be misidentified as failed supernova candidates when they are viewed nearly edge-on, because systems that are nearly edge-on will fade the most dramatically. Face-on mergers are expected to occur as well, but they are less likely to exhibit significant fading and therefore are less likely to be flagged as a disappearing star (Andrews et al. 2021). The intrinsic luminosity of an ILOT outburst likely depends on the mass of the engulfed companion, and in edge-on systems, extinction could obscure a significant portion of the outburst's light—especially if the event was relatively weak.

Kashi & Soker outline five evolutionary phases for such events: (1) *Pre-outburst interaction*, involving gradual brightening and increasing IR-to-optical luminosity ratios as dust begins to form; (2) *Early outburst*, characterized by a sharp rise in both optical and IR luminosity as mass is ejected; (3) *Late outburst*, during which equatorial dust fully obscures the central source, causing significant optical dimming; (4) *Post-outburst*, where the system is dominated by IR emission from polar dust; and (5) *Recovery*, as the dust shell gradually thins and the central source becomes visible again over years to decades.

The predicted observational signatures of Type II ILOTs can closely resemble those of failed supernovae, particularly the apparent disappearance of a massive star in visible wavelengths. Both M31-2014-DS1 and NGC 6946-BH1, for example, exhibit this behavior. In the ILOT scenario, this fading is explained by asymmetric dust formation obscuring the source, rather than by collapse to a black hole. Notably, some failed supernova candidates, such as NGC 6946-BH1, also show a luminous optical outburst (~10^6 $L_\odot$) prior to their disappearance, consistent with the "Early outburst" phase of the ILOT model. The extended duration of the optical dimming—lasting decades—is likewise consistent with the long recovery timescales predicted for equatorially enshrouded merger remnants. Kashi & Soker specifically suggest that NGC 6946-BH1 could be a Type II ILOT and predict that its visible emission may eventually re-emerge as the dust clears over time.

We note however, that predictions for the appearance of mergers and merger products are generally lacking through the literature. The presence of any outburst may depend on the mass of the companion as well as the orientation of the system. Qualitatively, the behaviour of both M31-2014-DS1 and N6946-BH1 seem to be consistent with observations of mergers (e.g. V1309 Sco). For DS1, we note that it's JWST spectrum shares a number of features with observations of luminous red novae (Karambelkar et al. 2025), in particular M31-LRN-2015, which is thought to have been the result of a merger.

7 CONCLUSIONS

In this paper, we investigate the likely fate of the failed supernova candidate M31-2014-DS1 in light of new observations from JWST and the SMA. Our main findings are as follows:

- We detect an infrared source coincident with the position of M31-2014-DS1 in JWST/NIRSpec, MIRI/LRS, and MIRI imaging. We derive a luminosity of $\log(L/L_\odot) = 3.85$, corresponding to approximately 7% of the progenitor system identified by De et al. (2024b). This value is likely a lower limit, as the spectral energy distribution (SED) shows the 10 μm silicate feature in absorption, alongside other molecular absorption features, indicative of high extinction along our viewing direction and an asymmetric dust geometry. We also cannot know whether the luminosity of the source identified by De et al. (2024b) was the quiescent luminosity of the system, or whether this was a value heightened by binary processes such as inspiralling.
- No source is detected at radio wavelengths.
- No X-rays are detected.
- We compare the observed properties to theoretical predictions for the outcome of a failed supernova. Current models, however, provide no clear expectations that would allow a failed supernova remnant to be distinguished observationally from a stellar merger.

Ultimately, while the source is significantly fainter than the progenitor, its fate remains uncertain. One possibility is that the star has collapsed to a black hole, in which case it will continue to fade. Alternatively, the event may have been the result of a stellar merger,

in which case the system could re-brighten once the dust obscuration diminishes and the central source becomes visible. Distinguishing between these scenarios will require further JWST monitoring over the coming years.

ACKNOWLEDGEMENTS

E.R.B. is supported by a Royal Society Dorothy Hodgkin Fellowship (grant no. DHF-R1-241114). Time-domain research by the University of Arizona team and D.J.S. is supported by National Science Foundation (NSF) grants 2108032, 2308181, 2407566, and 2432036 and the Heising-Simons Foundation under grant #2020-1864.

DATA AVAILABILITY

All JWST data presented in this work are available via MAST. The SMA data are available by request. Chandra data are available from the Chandra Data Archive (CDA).

REFERENCES

Adams S. M., Kochanek C. S., Gerke J. R., Stanek K. Z., Dai X., 2017, MNRAS, 468, 4968
Allan A. P., Groh J. H., Mehner A., Smith N., Boian I., Farrell E. J., Andrews J. E., 2020, MNRAS, 496, 1902
Andrews J. E., et al., 2021, ApJ, 917, 63
Antoni A., Quataert E., 2023, MNRAS, 525, 1229
Bahramian A., Heinke C. O., Degenaar N., Chomiuk L., Wijnands R., Strader J., Ho W. C. G., Pooley D., 2015, MNRAS, 452, 3475
Basinger C. M., Kochanek C. S., Adams S. M., Dai X., Stanek K. Z., 2021, MNRAS, 508, 1156
Beasor E. R., Davies B., Smith N., van Loon J. T., Gehrz R. D., Figer D. F., 2020, MNRAS, 492, 5994
Beasor E. R., Hosseinzadeh G., Smith N., Davies B., Jencson J. E., Pearson J., Sand D. J., 2024, ApJ, 964, 171
Beasor E. R., Smith N., Jencson J. E., 2025, ApJ, 979, 117
Blagorodnova N., et al., 2017, The Astrophysical Journal, 834, 107
Bond H. E., et al., 2011, The Astronomical Journal
Burrows A., Wang T., Vartanyan D., 2024, ApJ, 964, L16
Burrows A., Wang T., Vartanyan D., 2025, ApJ, 987, 164
Bushouse H., et al., 2022, JWST Calibration Pipeline, doi:10.5281/zenodo.7229890, https://doi.org/10.5281/zenodo.7229890
Cami J., Witteborn F. C., de Koter A., et al. 1997, Astrophysical Journal, 488, 268
Couch S. M., Warren M. L., O'Connor E. P., 2020, ApJ, 890, 127
Cox P., Huggins P. J., Greenberg J. M., et al. 1988, Astronomy & Astrophysics, 200, 143
Davies B., Beasor E. R., 2018, Monthly Notices of the Royal Astronomical Society, 474, 2116
Davies B., Beasor E. R., 2020a, MNRAS, 493, 468
Davies B., Beasor E. R., 2020b, MNRAS, 496, L142
De K., Jencson J., Lau R. M., MacLeod M., 2024a, Observing the birth of a black hole in M31, JWST Proposal. Cycle 3, ID. #6809
De K., et al., 2024b, arXiv e-prints, p. arXiv:2410.14778
Draine B., Lee H. M., 1984, The Astrophysical Journal, 285, 89
Ebinger K., Curtis S., Fröhlich C., Hempel M., Perego A., Liebendörfer M., Thielemann F.-K., 2019, ApJ, 870, 1
Eldridge J. J., Stanway E. R., 2022, ARA&A, 60, 455
Fraser M., 2016, Monthly Notices of the Royal Astronomical Society: Letters, 456, L16
Fryer C. L., Woosley S. E., Hartmann D. H., 1999, ApJ, 526, 152
Garmire G. P., et al., 2000, in AIAA Space Programs and Technologies Conference. Huntsville, AL
Gordon K. D., Clayton G. C., Decleir M., Fitzpatrick E. L., Massa D., Misselt K. A., Tollerud E. J., 2023, ApJ, 950, 86
Gustafsson B., Edvardsson B., Eriksson K., Jørgensen U. G., Nordlund Å., Plez B., 2008, Astronomy & Astrophysics, 486, 951
Hanner M. S., 1988, Astrophysical Journal, 334, L11
Healy S., Horiuchi S., Ashall C., 2024, arXiv e-prints, p. arXiv:2412.04386
Heger A., Fryer C. L., Woosley S. E., Langer N., Hartmann D. H., 2003, ApJ, 591, 288
Humphreys R. M., 2019, Research Notes of the American Astronomical Society, 3, 164
Jakobsen P., et al., 2022, Space Science Reviews, 218, 49
Jencson J. E., et al., 2019, The Astrophysical Journal Supplement Series
Jencson J. E., et al., 2022, ApJ, 930, 81
Kamiński T., Schmidt M., Tylenda R., 2010, Astronomy & Astrophysics
Karambelkar V., et al., 2025, arXiv e-prints, p. arXiv:2508.03932
Kashi A., Soker N., 2017, MNRAS, 467, 3299
Kemper F., Vriend W. J., Tielens A. G. G. M., Peeters E., Allamandola L. J., Barlow M. J., 2002, Astrophysical Journal, 577, 1007
Kochanek C. S., 2020, MNRAS, 493, 4945
Kochanek C. S., Beacom J. F., Kistler M. D., Prieto J. L., Stanek K. Z., Thompson T. A., Yüksel H., 2008, The Astrophysical Journal, 684, 1336
Kochanek C. S., Neustadt J. M. M., Stanek K. Z., 2024, ApJ, 962, 145
Laplace E., Schneider F. R. N., Podsiadlowski P., 2025, A&A, 695, A71
Lovegrove E., Woosley S. E., 2013, ApJ, 769, 109
Mainzer A., et al., 2014, The Astrophysical Journal, 784, 110
Mason E., Diaz M., Williams R. E., Preston G., Bensby T., 2010, A&A, 516, A108
Maund J. R., Smartt S. J., 2005, Monthly Notices of the Royal Astronomical Society, 360, 288
Montargès M., et al., 2021, Nature, 594, 365
Nadezhin D. K., 1980, Ap&SS, 69, 115
Neustadt J. M. M., Kochanek C. S., Stanek K. Z., Basinger C., Jayasinghe T., Garling C. T., Adams S. M., Gerke J., 2021, MNRAS, 508, 516
O'Connor E., Ott C. D., 2011, ApJ, 730, 70
Ohnaka K., Driebe T., Hofmann K.-H., Weigelt G., Wittkowski M., 2008, Astronomy & Astrophysics, 484, 371
Ott C. D., et al., 2011, Phys. Rev. Lett., 106, 161103
Pearson J., et al., 2025, arXiv e-prints, p. arXiv:2507.00125
Pejcha O., Metzger B. D., Tyles J. G., Tomida K., 2017, ApJ, 850, 59
Pence W. D., et al., 2019, Publications of the Astronomical Society of the Pacific, 131, 078003
Perna R., Duffell P., Cantiello M., MacFadyen A. I., 2014, ApJ, 781, 119
Perrin M. D., Soummer R., Elliott E. M., Lallo M. D., Sivaramakrishnan A., 2012, in Clampin M. C., Fazio G. G., MacEwen H. A., Oschmann Jacobus M. J., eds, Society of Photo-Optical Instrumentation Engineers (SPIE) Conference Series Vol. 8442, Space Telescopes and Instrumentation 2012: Optical, Infrared, and Millimeter Wave. p. 84423D, doi:10.1117/12.925230
Perrin M. D., Sivaramakrishnan A., Lajoie C.-P., Elliott E., Pueyo L., Ravindranath S., Albert L., 2014, in Oschmann Jacobus M. J., Clampin M., Fazio G. G., MacEwen H. A., eds, Society of Photo-Optical Instrumentation Engineers (SPIE) Conference Series Vol. 9143, Space Telescopes and Instrumentation 2014: Optical, Infrared, and Millimeter Wave. p. 91433X, doi:10.1117/12.2056689
Pierel J., 2024, Space-Phot: Simple Python-Based Photometry for Space Telescopes, doi:10.5281/zenodo.12100100, https://doi.org/10.5281/zenodo.12100100
Pierel J. D. R., et al., 2024, ApJ, 967, 50
Rau A., Kulkarni S. R., Ofek E. O., Yan L., 2007, The Astrophysical Journal, 659, 1536
Ray A., Farr W., Kalogera V., 2025, arXiv e-prints, p. arXiv:2507.09099
Renzo M., Ott C. D., Shore S. N., de Mink S. E., 2017, A&A, 603, A118
Reynolds T. M., Fraser M., Gilmore G., 2015, Monthly Notices of the Royal Astronomical Society, 453, 2885
Rieke G. H., et al., 2015, PASP, 127, 584
Schneider F. R. N., Laplace E., Podsiadlowski P., 2025, A&A, 700, A253
Shara M. M., Zurek D., Prialnik D., Yaron O., Kovetz A., 2010, ApJ, 725, 824

Smartt S., 2015, Publications of the Astronomical Society of Australia, 32, e016
Smartt S. J., Maund J. R., Hendry M. A., Tout C. A., Gilmore G. F., Mattila S., Benn C. R., 2004, Science, 303, 499
Smartt S., Eldridge J., Crockett R., Maund J. R., 2009, Monthly Notices of the Royal Astronomical Society, 395, 1409
Smith N., Li W., Filippenko A. V., Chornock R., 2011, Monthly Notices of the Royal Astronomical Society, 412, 1522
Smith N., et al., 2016, Monthly Notices of the Royal Astronomical Society, 458, 950
Smith N., et al., 2018, MNRAS, 480, 1466
Smith J. A., Vanden Berk D. E., Horne K., et al. 2020, Astronomical Journal, 160, 167
Stępień K., 2011, A&A, 531, A18
Sukhbold T., Woosley S. E., Heger A., 2018, ApJ, 860, 93
Tylenda R., et al., 2011, Astronomy & Astrophysics, 528, A114
Walmswell J. J., Eldridge J. J., 2012, Monthly Notices of the Royal Astronomical Society, 419, 2054
Wood P. R., Bessell M. S., Fox M. W., et al. 1989, Astrophysical Journal, 341, 957
Woosley S. E., Weaver T. A., 1986, ARA&A, 24, 205
Zapartas E., de Mink S. E., Justham S., Smith N., Renzo M., de Koter A., 2021, A&A, 645, A6

This paper has been typeset from a TEX/LATEX file prepared by the author.

Disappearance of a massive star in the Andromeda Galaxy due to formation of a black hole

Kishalay De[1,2,3*], Morgan MacLeod[4], Jacob E. Jencson[5], Elizabeth Lovegrove[6], Andrea Antoni[2], Erin Kara[3], Mansi M. Kasliwal[7], Ryan M. Lau[8], Abraham Loeb[4,9], Megan Masterson[3], Aaron M. Meisner[8], Christos Panagiotou[3], Eliot Quataert[10] and Robert Simcoe[3]

[1] Department of Astronomy and Columbia Astrophysics Laboratory, Columbia University, New York, USA

[2] Center for Computational Astrophysics, Flatiron Institute, New York, USA

[3] Kavli Institute for Astrophysics and Space Research, Massachusetts Institute of Technology, Cambridge, USA

[4] Center for Astrophysics, Harvard University & Smithsonian, Cambridge, USA

[5] IPAC, Caltech, Pasadena, USA [6] United States Naval Observatory, Washington DC, USA

[7] Cahill Center for Astrophysics, California Institute of Technology, Pasadena, USA

[8] National Optical-Infrared Astronomy Research Laboratory, National Science Foundation, Tucson, USA

[9] Black Hole Initiative, Harvard University, Cambridge, USA

[10] Department of Astrophysical Sciences, Princeton University, Princeton, USA

[*]Corresponding author. Email: kd3038@columbia.edu

When a massive star reaches the end of its lifetime, its core collapses and releases neutrinos that drive a shock into the outer layers (stellar envelope). A sufficiently strong shock ejects the envelope, producing a supernova. If the shock fails to eject it, the envelope is predicted to fall back onto the collapsing core, producing a stellar-mass black hole (BH) and causing the star to disappear. We

report observations of M31-2014-DS1, a hydrogen-depleted supergiant in the Andromeda Galaxy. In 2014 it brightened in the mid-infrared. From 2017 to 2022 it faded by factors of $\gtrsim 10^4$ in optical light, becoming undetectable, and $\gtrsim 10$ in total light. We interpret these observations, and those of a previous event in NGC 6946, as evidence for failed supernovae forming stellar-mass BHs.

Massive stars [those with initial masses $\gtrsim$ 10 solar masses ($M_\odot$)] can expand and become variable towards the end of their lifetime, undergoing luminosity changes observable on human timescales (*1*). These variations can result from unstable nuclear fusion in the core or mass transfer to a binary companion as the star expands (*2*). Some of these stars end their lives in luminous [$\gtrsim 10^7$ solar luminosities ($L_\odot$)] supernova (SN) explosions caused by the collapse of the core (*3, 4*) and subsequent ejection of the stellar envelope by neutrino-powered shocks (*1, 5*). These core-collapse SNe are routinely observed by optical time-domain surveys (*6*).

Theoretical models predict that in other massive stars, the neutrino shock fails to eject the envelope, causing most of the stellar material to fall back onto the collapsing core – forming a stellar mass black hole (BH) (*7, 8*). Even as the star abruptly disappears following the failed SN (*5, 9*), the initial loss of gravitational binding energy (equivalent to ≈ 0.2 to $0.5\,M_\odot$) to neutrino emission (*10, 11*) and feedback from inefficient accretion (*12, 13*) are predicted to inject $\sim 10^{45}$ to 10^{49} erg into the stellar envelope. This is sufficient to eject a small fraction of the outer envelope, possibly producing a faint optical transient ($\lesssim 10^6\,L_\odot$; (*11, 14*)). A long-lived brightening in mid-infrared (MIR) light can result from the condensation of this material in a circumstellar dust shell (*15, 16*). Observing such low luminosity stellar eruptions and stars that disappear without an explosion requires monitoring individual stars at extragalactic distances (*17, 18*) with uniform, sensitive searches over years to decades (*7*).

Observations of a disappearing supergiant

We applied an image subtraction pipeline (*19*) to the Near-Earth Object Wide-Field Infrared Survey Explorer (NEOWISE; (*20*)) MIR sky survey to search for variable sources in the Andromeda and Triangulum local group galaxies cataloged as Messier 31 and Messier 33, respectively. Using the six-month cadenced observations from 2009 to 2022, we searched for luminous MIR transients (*21*)

that would accompany dusty stellar eruptions such as failed SNe. We identified a faint brightening of a star (hereafter M31-2014-DS1) at celestial coordinates Right Ascension 00h 45m 13.47s, Declination +41° 32′ 33.14″ (J2000 equinox) (Figures 1B-D) towards M31. Beginning in 2014, this source source increased in MIR flux by ≈ 50% over ≈ 2 years, then faded below its initial flux within a year, and continued to fade until 2022 (Figures 2, 3 & S1).

We retrieved optical light curves of the source from ground and space-based surveys (*21*). In optical light, this source faded by a factor of $\gtrsim$ 100 between 2016 and 2019, and was undetectable in recent ground-based optical imaging using the MMT Observatory in 2023 (Figure 2). This location was also serendipitously imaged by the Hubble Space Telescope (HST) in 2022. We re-analyzed the HST data (*21*), finding no detection in the optical F606W filter (Figure 1F), but a faint source ($\gtrsim 10^4\times$ fainter than the progenitor from 2012) in the near-infrared (NIR) F814W filter (Figure 1H). We obtained follow-up NIR imaging and spectroscopic observations using the Infrared Telescope Facility and Keck telescopes in 2023 (*21*), which confirm a faint red source in the NIR JHK-bands (Figures 1J and 4B).

This source was previously identified as an irregular variable star (designated V7984 M31B; (*22*)), and classified as a candidate red supergiant (RSG) based on archival NIR colors (*23*). We used archival HST and Spitzer Space Telescope (SST) observations from 2005-2012 (*21*) to measure the star's spectral energy distribution (SED). We fitted the SED with a model of a blackbody photosphere surrounded by a circumstellar dust shell expected from mass loss in evolved stars (Figure 3). The best-fitting model corresponds to a supergiant star with luminosity $L \approx 10^5 L_\odot$ and effective temperature $T_{\rm eff} \approx 4500$ K surrounded by a dust shell with temperature $T_d \approx 870$ K at a radius of ≈ 110 astronomical units (au). Although previously classified as a candidate RSG, this effective temperature classifies the star as a warmer, yellow supergiant (*24, 25*). The observed red SED is due to reddening by the circumstellar dust, from which we infer a high mass-loss rate of $\approx 10^{-4}\,{\rm M}_\odot\ {\rm yr}^{-1}$ (*21*).

To investigate how these properties varied over time, we applied the same SED model to optical data from the Gaia space telescope and MIR data from NEOWISE (*21*). The best-fitting models have an almost constant bolometric luminosity (radiated power integrated across all wavelengths) for ≈ 1000 days after the MIR brightening began, which then declines by $\gtrsim$ 10× over the next ≈ 1000 days (*21*) (Figure 5). During this time, the source became more obscured by dust (Figures

4 & S5), with the dust shell reaching an optical depth $\tau \gtrsim 20$ and the central blackbody reducing in radius by a factor of $\gtrsim 5$ (*21*) (Figure 4).

Core-collapse of a massive star

The abrupt and sustained bolometric fading of M31-2014-DS1 is unlike the variations observed in other massive, evolved stars (*26, 27*). Some sources exhibit a temporary optical dimming due to episodes of enhanced mass loss and dust formation (*28, 29*), but this re-processes the optical emission into the infrared, so the bolometric luminosity remains constant or gets brighter (*21*) due to ongoing nuclear fusion and sometimes energy injection from a binary companion (*30, 31*). Even with dust obscuration, those sources become brighter in the infrared. Geometric effects, such as preferential mass loss along the equator (*32*) can reduce the fraction of the remnant luminosity that reaches an observer; however, calculations show this can reduce the observed luminosity by no more than a factor of two (*33*). This expectation is consistent with observations of nearby stellar merger remnants with known mass ejection geometry (*33*).

The continuous optical and MIR observations of M31-2014-DS1 during its fading (Figure 2) show no commensurate increase in infrared brightness while the optical brightness faded by a factor of 10^4. Therefore the bolometric luminosity reduced, which we attribute to a cessation in nuclear fusion and the collapse of the stellar core. There is no evidence for an associated core-collapse SN, which would have been easily observable. We therefore interpret M31-2014-DS1 as a failed SN in which most of the stellar envelope fell back to form a BH (*7*).

Interpretation as a failed supernova

We compare the inferred properties of M31-2014-DS1 to stellar evolution models and the theoretically expected end-stages of massive stars. The observed progenitor properties (Figure 3, between 2005 to 2012) are hotter than predicted for the nominal end-point of single star evolutionary tracks (*34*) which characterize the progenitors of the hydrogen-rich SNe IIP; however, they are similar to the observed progenitors of some hydrogen-deficient SNe (the Type IIb and IIL SNe) (*5*). The latter have been interpreted as arising from high mass loss (due to winds or binary interaction; (*35, 36*)) that removed most of the hydrogen-rich stellar envelope. We constructed stellar

models of that process (*21*) and find the closest match with the observed progenitor has a terminal mass of $\approx 5\,M_\odot$, of which $\approx 0.28\,M_\odot$ is the outer hydrogen-rich envelope (Figure 3B). This model had an initial mass of $\approx 13 M_\odot$, and is bluer at late times than a hydrogen-rich counterpart without enhanced mass loss (*21*).

We use the optical observations to empirically constrain any mass ejection associated with the collapsing stellar core. Based on analytical models for outbursts caused by energy injection into hydrogen-rich envelopes (*37*), we set an upper limit of $\lesssim 0.1\,M_\odot$ ejected material at the star's escape velocity $v_{\rm esc} \approx 60\,{\rm km\,s^{-1}}$, and corresponding limits of $\lesssim 0.3\,M_\odot$ at $5\,v_{\rm esc}$ and $\lesssim 1.5\,M_\odot$ at $25\,v_{\rm esc}$ (Figure 5A). These constraints imply that most of the $\approx 5\,M_\odot$ star collapsed instead of being ejected, exceeding the maximum mass of a neutron star (*38*) and therefore forming a BH.

If the star were collapsing purely due to its self-gravity, the outer envelope would collapse into the BH within roughly its free-fall time $t_{\rm ff} \approx \frac{1}{\sqrt{G\rho}} \approx 210\,{\rm d}$, where G is the Gravitational constant and ρ is the average stellar density. This is shorter than the observed continued bolometric fading over $\gtrsim 1000\,{\rm d}$ (Figure 5), indicating that the fallback is delayed by energy injected into the outer envelope. To simulate the resulting mass accretion onto the central BH, we take the same hydrogen-depleted progenitor star model as above but add a range of shock energies ($\sim 10^{45}$ to 10^{49} erg) into the outer envelope. Such shocks are expected from neutrino mass loss and feedback from inefficient accretion (*39–41*) during the collapse of the core. In the final stages of stellar evolution, these outer layers undergo vigorous turbulent convection, which carries substantial angular momentum (*12, 13*) and suppresses direct accretion (*42*). Numerical simulations (*41*) show that $\lesssim 1\%$ of material falling from the outer supergiant envelope accretes directly onto the BH. We adopt an analytic model of the accreted fraction as a function of the relative angular momenta of the fallback material and that of an orbit at the BH horizon (*21*).

The results from our models indicate that the mass accretion rate declines rapidly at early times, initially far exceeding the maximum accretion rate (the Eddington accretion rate) where photons can freely escape from near the BH (*43*). During this phase, the emergent luminosity is expected (*44*) to be capped near the Eddington luminosity $L_{\rm Edd} \approx 6 \times 10^{38}\,{\rm erg\,s^{-1}}$ (for a $5\,M_\odot$ BH), corresponding to the limit where material accreting at the Eddington accretion rate generates accretion luminosity such that the outward radiation pressure balances the inward gravitational pull of the BH.

Comparing these models to the observations (Figure 5) indicates that the $\approx 1000\,{\rm d}$ luminosity

plateau is explained by a super-Eddington accretion phase when the source luminosity remains steady at $\approx$ 30 to 50% $L_{\rm Edd}$ despite more rapid mass infall. As the infall rate falls below the Eddington rate, the emergent luminosity is expected to become proportional to the decaying accretion rate, as observed in the data. Larger shock energies unbind a larger fraction of the progenitor envelope, leaving behind a smaller mass that falls back over a shorter period of time. Although we cannot precisely constrain the exact time of collapse, the fading by a factor of $\approx$ 10 over $\approx$ 1000 d is most consistent with shock energies of 10^{47} to 10^{48} erg (Figure 5). In those cases, $\approx$ 98% of the stellar mass collapses or falls back, leaving a $\approx 5 M_{\odot}$ BH.

Those are weak shock energies compared to typical core collapse SNe ($\sim 10^{51}$ erg; (*5*)). They are sufficient to unbind $\lesssim 0.1 M_{\odot}$ of the outer envelope, which would produce a luminous optical outburst that is sufficiently brief to have been missed by observations given the photometric cadence (Figure 5). We expect the ejected mass to carry a distribution of velocities as it moves outwards and cools (*21*). Most of the material would reach the dust condensation radius ($r_{\rm c}$) at which solid dust grains begin to condense from the ejecta. This would produce hot dust on a timescale of $\sim r_{\rm c}/v_{\rm esc} \approx 30\,{\rm au}/60\,{\rm km\,s^{-1}} \approx 900\,{\rm d}$ after the ejection, which is consistent with the time of the observed peak MIR flux. Although the details of the dust formation are sensitive to the velocity distribution and dust formation process (*30*), our model velocity distributions (*21*) imply that the fraction of the total ejecta in the hot dust shell (near $r_{\rm c}$) is $f_{\rm shell} \approx 0.1$ at any given time. The hot dust mass in the shell is therefore $m_{\rm shell} \sim f_{\rm shell} M_g r_{\rm dg}$, where M_g is the total ejected gas mass ($\sim 0.1\,{\rm M}_{\odot}$) and $r_{\rm dg} \approx 0.01$ (*45, 46*) is the assumed dust-to-gas mass ratio. We find $m_{\rm shell} \sim 10^{-4}\,{\rm M}_{\odot}$, which is similar to the dust mass derived from the SED ($\approx 1.1 \times 10^{-4}\,{\rm M}_{\odot}$; Figure S5).

Unified model for a previous candidate

A candidate disappearing supergiant (designated NGC 6946-BH1) has previously been identified in the galaxy NGC 6946 (*16, 47, 48*). Figure 3 also shows its progenitor for comparison with M31-2014-DS1. NGC 6946-BH1 exhibited a luminous ($\sim 10^6\,{\rm L}_{\odot}$) optical outburst followed by an expanding dusty envelope, implying $\sim 0.1 - 1\,{\rm M}_{\odot}$ of ejecta (*48*). This was consistent with predictions of either failed SNe from hydrogen-rich progenitors (*11*) or some types of stellar mergers (*32, 49*). The dust-obscured remnant then faded to $\approx$ 15% ($\sim 10^{38}$ erg s^{-1}) of the progenitor

luminosity in ≈ 3000 days (*16*), indicating the termination of nuclear fusion (*50*). However, this is difficult to reconcile with the decades-long ($\gtrsim 10^5$ d) super-Eddington phase for massive hydrogen-rich stars (*48, 51*), during which the emergent luminosity is expected to be constant near the BH Eddington limit ($\sim 10^{39}$ erg s^{-1}). By constructing a hydrogen-rich RSG progenitor model (*21*) that matches the M31-2014-DS1 progenitor luminosity, we confirm that rapid fading timescales of a few years cannot be explained with stars that have largely retained their hydrogen-rich envelopes (Figure 5).

The progenitor of NGC 6946-BH1 was initially identified as an RSG (*16, 47*). Later analysis found that it was hotter than expected for single star RSG evolution (Figure 3), being more consistent with a yellow supergiant (*52*). We compare its properties to our models, finding that the closest match is a progenitor with an initial mass of $17.5 M_\odot$ with enhanced late-stage mass loss, which forms a hydrogen-depleted star with a terminal mass of $\approx 7.5\,M_\odot$ of which $\approx 0.6\,M_\odot$ is the hydrogen-rich envelope (Figure 3; (*21*)). Applying a similar analysis as for M31-2014-DS1 (*21*), we calculate that the twice as massive hydrogen-rich envelope in the NGC 6946-BH1 model produces a longer duration outburst (~ 150 d), as observed. Our calculated accretion-powered plateau and fallback timescale (~ 3000 d) are consistent with the bolometric fading of NGC 6946-BH1 (*21, 49, 50*).

M31-2014-DS1 has more archival data available than NGC 6946-BH1, which excludes a similar optical outburst and better constrains the fading timescale, which we connect with our hydrogen-depleted progenitor model. Nevertheless, the similarities between M31-2014-DS1 and NGC 6946-BH1 lead us to conclude they were both associated with the core collapse of massive hydrogen-depleted stars that produced stellar mass BHs. Accretion onto the BHs might produce X-ray emission, but that has not been detected for either M31-2014-DS1 (from archival X-ray observations (*21*)) and NGC 6946-BH1, which is explained by X-ray absorption from the surrounding gas (*21, 48, 53*). Theoretical models of BH formation from massive stars predict a wide range of stellar progenitors (*54, 55*) with few observational constraints. Using previous estimates for the fraction of failed SNe (*18, 56, 57*), we calculate that the probability of us identifying at least one event in our search is 1 to 20% (*21*). Our calculated stellar evolution of M31-2014-DS1 is similar to many core collapse SN progenitors (Figure 3) implying a complex (possibly chaotic) relationship between stellar birth mass and BH formation for stars with initial masses $\gtrsim 12\,M_\odot$, as previously predicted on theoretical grounds (*54, 55*).

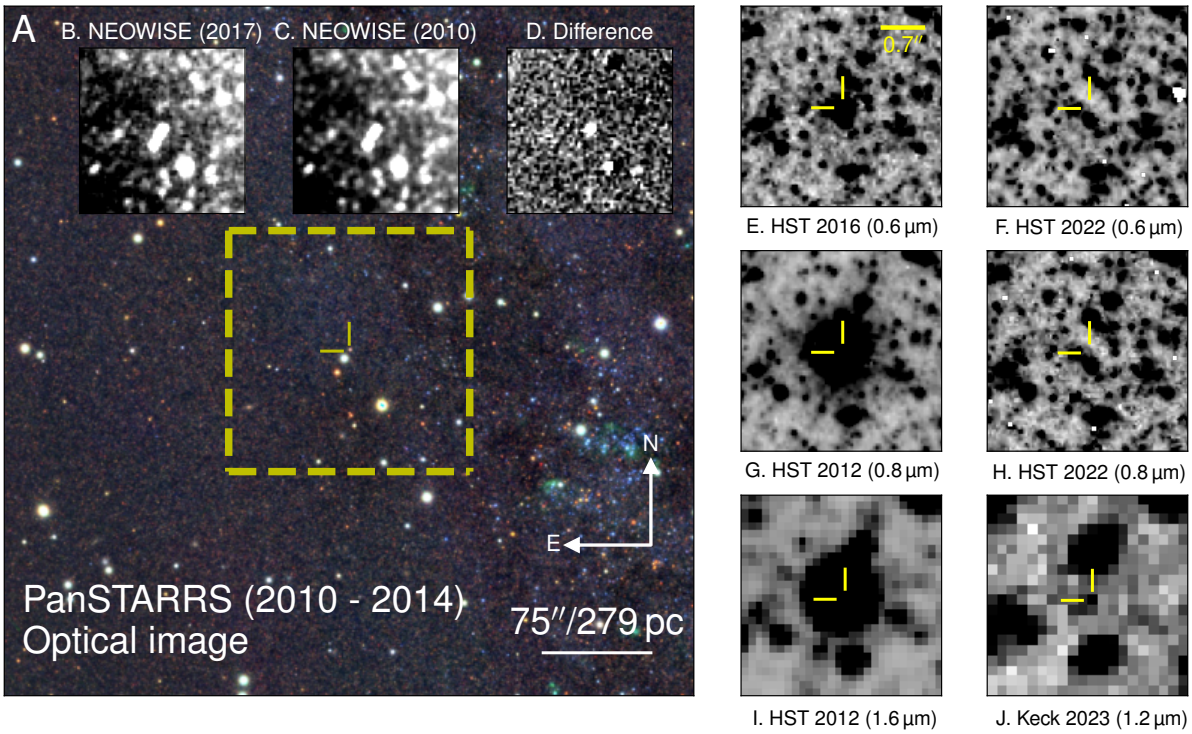

Figure 1: **Location and disappearance of M31-2014-DS1.** (A) Optical color composite image of the discovery field taken from the Panoramic Survey Telescope and Rapid Response System (PanSTARRS/PS1 survey; (*21*)). The yellow dashed square indicates the region shown in panels B-D (where white indicates brighter pixels) and the yellow cross-hair marks the position of the star. (B) NEOWISE (*20*) MIR image taken in 2017, (C) NEOWISE image in 2010 and (D) the difference between them. The other panels show zoomed-in images of the star (as indicated by the scale, with black indicating brighter pixels) taken in the labeled years: (E-H) optical HST images; (I) near-infrared HST image; (J) near-infrared Keck image.

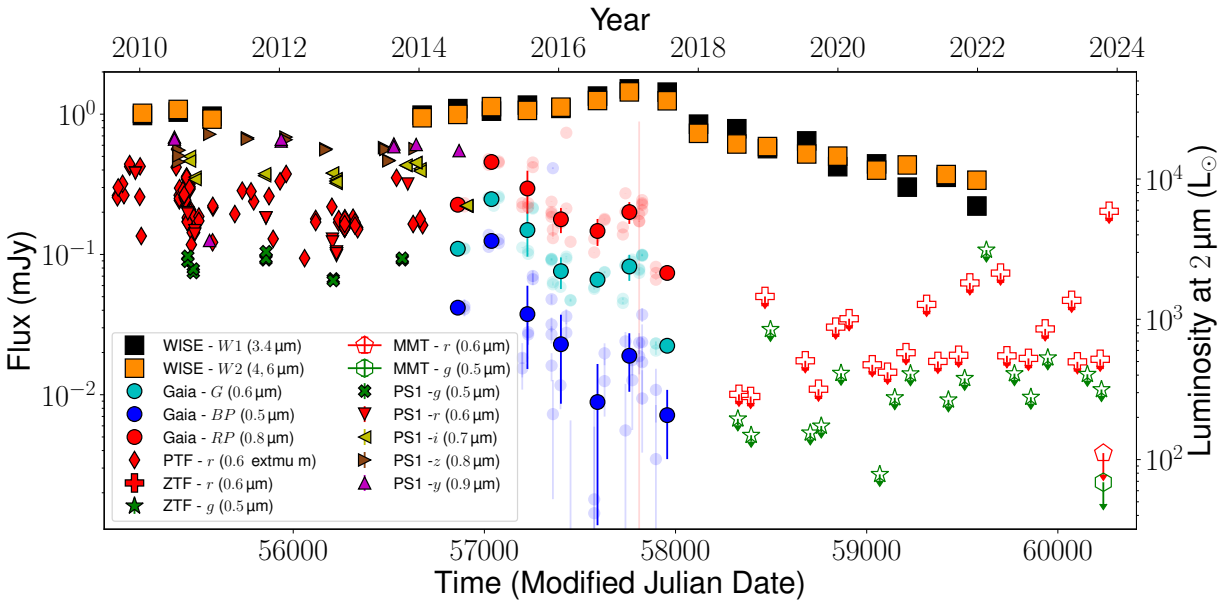

Figure 2: **Brightness of M31-2014-DS1 as a function of time**. The measured flux in millijansky (mJy, left axis) and equivalent luminosity at the distance of the Andromeda Galaxy (right axis), both on logarithmic scales, are plotted as a function of time in modified Julian date (MJD, lower axis) and Gregorian year (upper axis). Archival data are from the Palomar Transient Factory (PTF), NEOWISE, PS1, Gaia and Zwicky Transient Facility (ZTF) surveys; also shown are follow-up photometric data from the MMT Observatory (*21*). Error bars are 1σ confidence (smaller than the symbol size for the NEOWISE and pre-2014 data); hollow symbols with downwards arrows are 5σ upper limits. For the Gaia photometry, we show the raw measurements as light symbols, while the dark symbols are the averages within 45 d of the closest epoch of NEOWISE data. The luminosity is monochromatic λF_λ, where λ is the wavelength and F_λ is the flux density, scaled to a wavelength of 2 µm. The MIR data are shown on a linear scale in Figure S1, and all photometric data are provided (with references provided in (*21*)) in the online data repository.

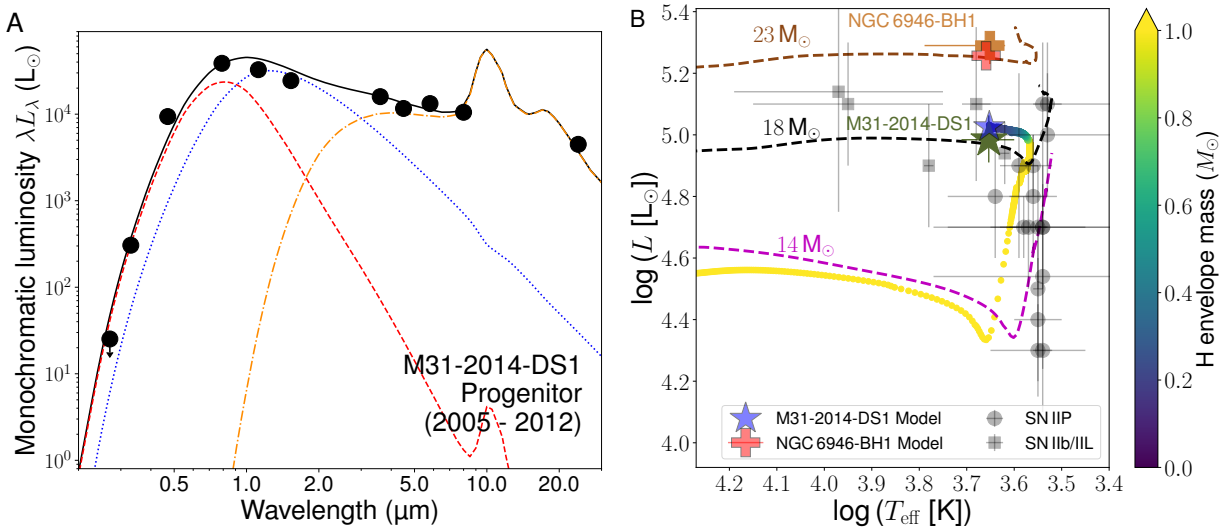

Figure 3: **Spectral energy distribution and physical properties of the progenitor.** (A) The ultraviolet to MIR SED of M31-2014-DS1 (solid and hollow circles, in units of the monochromatic luminosity $\lambda\, L_\lambda$, where L_λ is the luminosity density) observed with HST and SST from 2005-2012. Lines are the best-fitting `DUSTY` model (parameters are listed in Table S2). Total flux (black solid line), dust emission (orange dot-dashed), dust-scattered stellar emission (red-dashed) and dust-attenuated stellar emission (blue dotted). Error bars are 1σ confidence (smaller than the symbol sizes), and downward arrows are 5σ upper limits. (B) The observed luminosity and effective temperature of M31-2014-DS1 (green star, from panel A) compared to theoretical single star evolutionary tracks at different initial masses (colored dashed lines) (*34*). The observed progenitor of NGC 6946-BH1 (brown plus symbol) and those of known hydrogen-rich SNe (*8*) (type indicated in legend) are shown. Error bars are 1σ confidence. Colored circles are our stellar evolution model for the progenitor of M31-2014-DS1 (*21*), with the residual hydrogen envelope mass indicated by the color bar. The model at the time of core collapse is indicated for M31-2014-DS1 (blue star) and for NGC 6946-BH1 (red plus symbol).

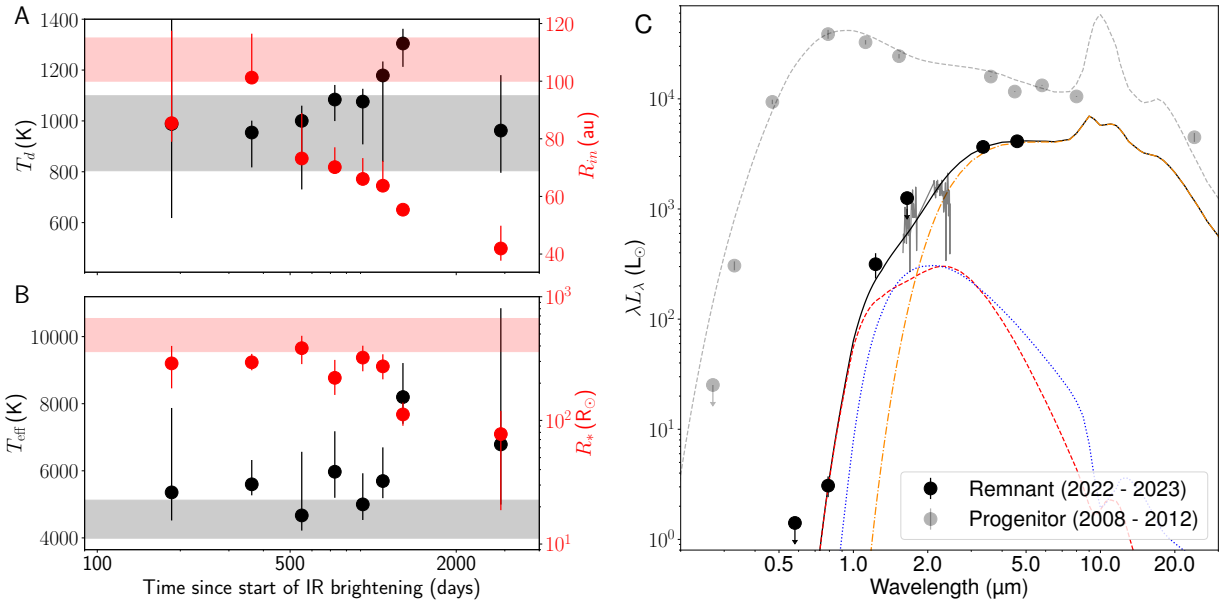

Figure 4: **Evolution of the stellar and dust properties of M31-2014-DS1.** Temporal evolution of the dust shell and stellar photosphere inferred from the SED model fitting: (A) the dust temperature (T_d; black, left axis) and inner shell radius (R_in; red, right axis) and (B) the effective temperature (black, left axis) and inferred stellar radius (red, right axis). These are plotted as functions of time since the start of the MIR brightening in 2014 (MJD 56674.19; Figure 2 and (*21*)). The shaded regions are the corresponding model parameters for the progenitor from 2005-2012. Other parameters are shown in Figure S5. The SED of the remnant of M31-2014-DS1 (C) in 2022 to 2023 [photometry in black circles and spectrum in gray lines (shown on a linear scale in Figure S2)]. The best-fitting `DUSTY` model with line styles as in Figure 3, and parameters are listed in Table S2. The corresponding progenitor photometry (gray circles) and SED model (dashed grey line) are shown. Error bars are 1σ confidence and downward arrows are 5σ upper limits.

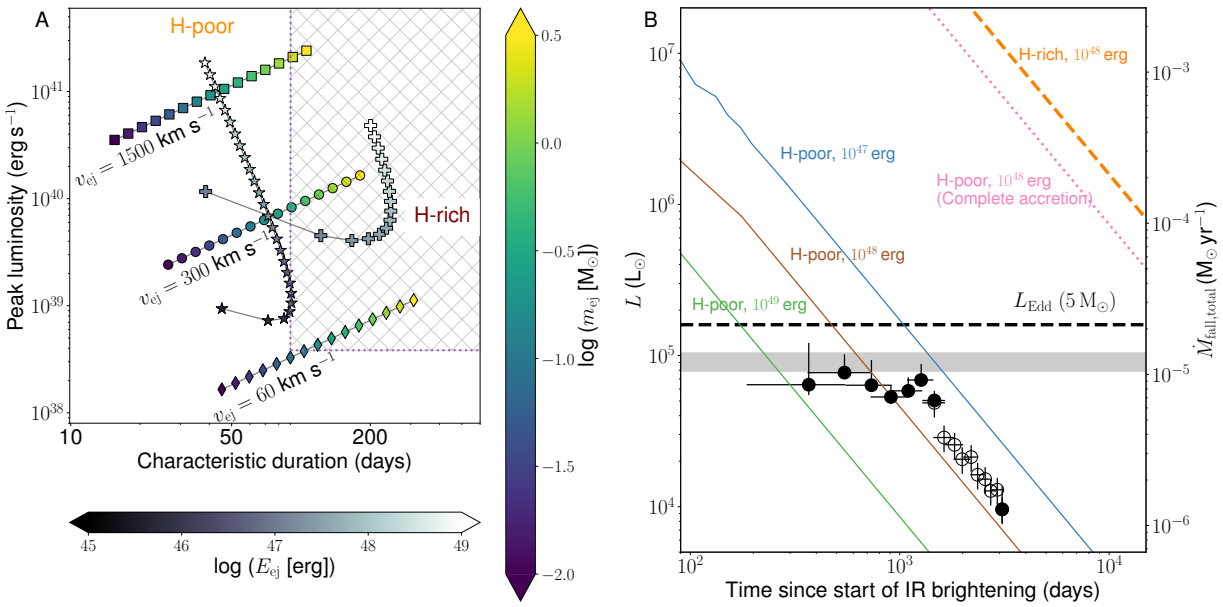

Figure 5: **Constraints on the mass ejection and stellar envelope fallback in M31-2014-DS1.** (A) The luminosity and duration of transients powered by energy injection into hydrogen-rich envelopes, for ejecta with different velocities (v_{ej}) and kinetic energies (E_{ej}). The diamonds, circles, and squares indicate ejecta with velocities of $\approx$ 1×, $\approx$ 5×, and $\approx$ 25× the progenitor's escape velocity respectively, with colors indicating ejecta mass (m_{ej}; right color bar). The cross-hatched area shows the phase space ruled out by the optical photometry (*21*). Also shown are the luminosity and transient duration for the H-poor (stars) and H-rich (plus symbols) models as a function of ejecta kinetic energy (bottom color bar). (B) The bolometric fading of M31-2014-DS1 compared to models of mass fallback rates for different explosion energies. The hydrogen-poor and hydrogen-rich progenitor models both assume 5% accretion radiative efficiency. For comparison, the dotted pink line shows 100% accretion in the H-poor case and the dashed orange line shows an example H-rich case. Black solid circles are parameters inferred from the SED models, and hollow circles are estimates using a bolometric correction to MIR luminosity (*21*). Error bars are 1σ confidence. The gray shaded region shows the progenitor luminosity, and the black dashed line shows the Eddington luminosity (L_{Edd}) for a 5 $M_\odot$ BH. The right axis shows the corresponding total mass fallback rate ($\dot{M}_{fall,total}$) from the models.

References and Notes

1. N. Langer, Presupernova Evolution of Massive Single and Binary Stars. Ann. Rev. Astron. Astrophys. **50**, 107–164 (2012), doi:10.1146/annurev-astro-081811-125534.

2. N. Smith, W. Li, J. M. Silverman, M. Ganeshalingam, A. V. Filippenko, Luminous blue variable eruptions and related transients: diversity of progenitors and outburst properties. Mon. Not. R. Astron. Soc. **415** (1), 773–810 (2011), doi:10.1111/j.1365-2966.2011.18763.x.

3. H. T. Janka, K. Langanke, A. Marek, G. Martínez-Pinedo, B. Müller, Theory of core-collapse supernovae. Phys. Rep. **442** (1-6), 38–74 (2007), doi:10.1016/j.physrep.2007.02.002.

4. A. Burrows, D. Vartanyan, Core-collapse supernova explosion theory. Nature **589** (7840), 29–39 (2021), doi:10.1038/s41586-020-03059-w.

5. S. J. Smartt, Progenitors of Core-Collapse Supernovae. Ann. Rev. Astron. Astrophys. **47** (1), 63–106 (2009), doi:10.1146/annurev-astro-082708-101737.

6. D. A. Perley, *et al.*, The Zwicky Transient Facility Bright Transient Survey. II. A Public Statistical Sample for Exploring Supernova Demographics. Astrophys. J. **904** (1), 35 (2020), doi:10.3847/1538-4357/abbd98.

7. C. S. Kochanek, *et al.*, A Survey About Nothing: Monitoring a Million Supergiants for Failed Supernovae. Astrophys. J. **684** (2), 1336–1342 (2008), doi:10.1086/590053.

8. S. J. Smartt, Observational Constraints on the Progenitors of Core-Collapse Supernovae: The Case for Missing High-Mass Stars. Publ. Astron. Soc. Aust. **32**, e016 (2015), doi:10.1017/pasa.2015.17.

9. E. O'Connor, C. D. Ott, Black Hole Formation in Failing Core-Collapse Supernovae. Astrophys. J. **730** (2), 70 (2011), doi:10.1088/0004-637X/730/2/70.

10. D. K. Nadezhin, Some Secondary Indications of Gravitational Collapse. Astrophys. Space Sci. **69** (1), 115–125 (1980), doi:10.1007/BF00638971.

11. E. Lovegrove, S. E. Woosley, Very Low Energy Supernovae from Neutrino Mass Loss. Astrophys. J. **769** (2), 109 (2013), doi:10.1088/0004-637X/769/2/109.

12. A. Gilkis, N. Soker, Angular Momentum Fluctuations in the Convective Helium Shell of Massive Stars. Astrophys. J. **827** (1), 40 (2016), doi:10.3847/0004-637X/827/1/40.

13. E. Quataert, D. Lecoanet, E. R. Coughlin, Black hole accretion discs and luminous transients in failed supernovae from non-rotating supergiants. Mon. Not. R. Astron. Soc. **485** (1), L83–L88 (2019), doi:10.1093/mnrasl/slz031.

14. E. Lovegrove, S. E. Woosley, W. Zhang, Very Low-energy Supernovae: Light Curves and Spectra of Shock Breakout. Astrophys. J. **845** (2), 103 (2017), doi:10.3847/1538-4357/aa7b7d.

15. C. S. Kochanek, Dust formation by failed supernovae. Mon. Not. R. Astron. Soc. **444** (3), 2043–2047 (2014), doi:10.1093/mnras/stu1559.

16. S. M. Adams, C. S. Kochanek, J. R. Gerke, K. Z. Stanek, X. Dai, The search for failed supernovae with the Large Binocular Telescope: confirmation of a disappearing star. Mon. Not. R. Astron. Soc. **468** (4), 4968–4981 (2017), doi:10.1093/mnras/stx816.

17. T. M. Reynolds, M. Fraser, G. Gilmore, Gone without a bang: an archival HST survey for disappearing massive stars. Mon. Not. R. Astron. Soc. **453** (3), 2885–2900 (2015), doi:10.1093/mnras/stv1809.

18. J. M. M. Neustadt, *et al.*, The search for failed supernovae with the Large Binocular Telescope: a new candidate and the failed SN fraction with 11 yr of data. Mon. Not. R. Astron. Soc. **508** (1), 516–528 (2021), doi:10.1093/mnras/stab2605.

19. K. De, *et al.*, An infrared transient from a star engulfing a planet. Nature **617** (7959), 55–60 (2023), doi:10.1038/s41586-023-05842-x.

20. A. Mainzer, *et al.*, Initial Performance of the NEOWISE Reactivation Mission. *Astrophys. J.* **792** (1), 30 (2014), doi:10.1088/0004-637X/792/1/30.

21. Materials and methods are available as supplementary materials.

22. J. Kaluzny, *et al.*, DIRECT Distances to Nearby Galaxies Using Detached Eclipsing Binaries and Cepheids. I. Variables in the Field M31B. Astron. J. **115** (3), 1016–1044 (1998), doi: 10.1086/300235.

23. P. Massey, K. F. Neugent, E. M. Levesque, M. R. Drout, S. Courteau, The Red Supergiant Content of M31 and M33. Astron. J. **161** (2), 79 (2021), doi:10.3847/1538-3881/abd01f.

24. E. R. Beasor, N. Smith, J. E. Andrews, Don't Believe the Hype(r): The Yellow Supergiants of Westerlund 1. Astrophys. J. **952** (2), 113 (2023), doi:10.3847/1538-4357/acdd6d.

25. R. M. Humphreys, T. J. Jones, J. C. Martin, Yellow Supergiants and Post-red Supergiant Evolution in the Large Magellanic Cloud. Astron. J. **166** (2), 50 (2023), doi: 10.3847/1538-3881/acdd6c.

26. C. Conroy, *et al.*, A Complete Census of Luminous Stellar Variability on Day to Decade Timescales. Astrophys. J. **864** (2), 111 (2018), doi:10.3847/1538-4357/aad460.

27. M. D. Soraisam, *et al.*, Variability of Massive Stars in M31 from the Palomar Transient Factory. Astrophys. J. **893** (1), 11 (2020), doi:10.3847/1538-4357/ab7b7b.

28. J. E. Jencson, *et al.*, An Exceptional Dimming Event for a Massive, Cool Supergiant in M51. Astrophys. J. **930** (1), 81 (2022), doi:10.3847/1538-4357/ac626c.

29. A. K. Dupree, *et al.*, The Great Dimming of Betelgeuse: A Surface Mass Ejection and Its Consequences. Astrophys. J. **936** (1), 18 (2022), doi:10.3847/1538-4357/ac7853.

30. C. S. Kochanek, The Astrophysical Implications of Dust Formation during the Eruptions of Hot, Massive Stars. Astrophys. J. **743** (1), 73 (2011), doi:10.1088/0004-637X/743/1/73.

31. N. Smith, D. J. Frew, A revised historical light curve of Eta Carinae and the timing of close periastron encounters. Mon. Not. R. Astron. Soc. **415** (3), 2009–2019 (2011), doi: 10.1111/j.1365-2966.2011.18993.x.

32. A. Kashi, N. Soker, Type II intermediate-luminosity optical transients (ILOTs). Mon. Not. R. Astron. Soc. **467** (3), 3299–3305 (2017), doi:10.1093/mnras/stx240.

33. C. S. Kochanek, Transients obscured by dusty discs. Mon. Not. R. Astron. Soc. **529** (3), 1958–1969 (2024), doi:10.1093/mnras/stae589.

34. J. Choi, *et al.*, Mesa Isochrones and Stellar Tracks (MIST). I. Solar-scaled Models. *Astrophys. J.* **823** (2), 102 (2016), doi:10.3847/0004-637X/823/2/102.

35. C. Georgy, Yellow supergiants as supernova progenitors: an indication of strong mass loss for red supergiants? Astron. & Astrophys. **538**, L8 (2012), doi:10.1051/0004-6361/201118372.

36. S.-C. Yoon, M. Cantiello, Evolution of Massive Stars with Pulsation-driven Superwinds During the Red Supergiant Phase. Astrophys. J. **717** (1), L62–L65 (2010), doi:10.1088/2041-8205/717/1/L62.

37. D. Kasen, S. E. Woosley, Type II Supernovae: Model Light Curves and Standard Candle Relationships. Astrophys. J. **703** (2), 2205–2216 (2009), doi:10.1088/0004-637X/703/2/2205.

38. V. Kalogera, G. Baym, The Maximum Mass of a Neutron Star. Astrophys. J. **470**, L61 (1996), doi:10.1086/310296.

39. E. Quataert, D. Kasen, Swift 1644+57: the longest gamma-ray burst? Mon. Not. R. Astron. Soc. **419** (1), L1–L5 (2012), doi:10.1111/j.1745-3933.2011.01151.x10.1086/141928.

40. M. Ivanov, R. Fernández, Mass Ejection in Failed Supernovae: Equation of State and Neutrino Loss Dependence. Astrophys. J. **911** (1), 6 (2021), doi:10.3847/1538-4357/abe59e.

41. A. Antoni, E. Quataert, Numerical simulations of the random angular momentum in convection - II. Delayed explosions of red supergiants following 'failed' supernovae. Mon. Not. R. Astron. Soc. **525** (1), 1229–1245 (2023), doi:10.1093/mnras/stad2328.

42. J. M. Blondin, Hypercritical Spherical Accretion onto Compact Objects. Astrophys. J. **308**, 755 (1986), doi:10.1086/164548.

43. Y.-F. Jiang, L. Dai, Numerical Simulations of Super-Eddington Accretion Flows. *arXiv e-prints* arXiv:2408.16856 (2024), doi:10.48550/arXiv.2408.16856.

44. Y.-F. Jiang, J. M. Stone, S. W. Davis, A Global Three-dimensional Radiation Magnetohydrodynamic Simulation of Super-Eddington Accretion Disks. Astrophys. J. **796** (2), 106 (2014), doi:10.1088/0004-637X/796/2/106.

45. V. Karambelkar, *et al.*, Hot springs and dust reservoirs: JWST reveals the dusty, molecular aftermath of extragalactic stellar mergers. *arXiv e-prints* arXiv:2508.03932 (2025), doi:10.48550/arXiv.2508.03932.

46. T. Kamiński, *et al.*, V838 Monocerotis as seen by ALMA: A remnant of a binary merger in a triple system. Astron. & Astrophys. **655**, A32 (2021), doi:10.1051/0004-6361/202141526.

47. J. R. Gerke, C. S. Kochanek, K. Z. Stanek, The search for failed supernovae with the Large Binocular Telescope: first candidates. Mon. Not. R. Astron. Soc. **450** (3), 3289–3305 (2015), doi:10.1093/mnras/stv776.

48. C. M. Basinger, C. S. Kochanek, S. M. Adams, X. Dai, K. Z. Stanek, The search for failed supernovae with the Large Binocular Telescope: N6946-BH1, still no star. Mon. Not. R. Astron. Soc. **508** (1), 1156–1164 (2021), doi:10.1093/mnras/stab2620.

49. E. R. Beasor, *et al.*, JWST Reveals a Luminous Infrared Source at the Position of the Failed Supernova Candidate N6946-BH1. Astrophys. J. **964** (2), 171 (2024), doi:10.3847/1538-4357/ad21fa.

50. C. S. Kochanek, J. M. M. Neustadt, K. Z. Stanek, The Search for Failed Supernovae with the Large Binocular Telescope: The Mid-infrared Counterpart to N6946-BH1. Astrophys. J. **962** (2), 145 (2024), doi:10.3847/1538-4357/ad18d7.

51. R. Fernández, E. Quataert, K. Kashiyama, E. R. Coughlin, Mass ejection in failed supernovae: variation with stellar progenitor. Mon. Not. R. Astron. Soc. **476** (2), 2366–2383 (2018), doi:10.1093/mnras/sty306.

52. R. M. Humphreys, Comments on the Progenitor of NGC 6946-BH1. *Research Notes of the American Astronomical Society* **3** (10), 164 (2019), doi:10.3847/2515-5172/ab5191.

53. S. Balberg, L. Zampieri, S. L. Shapiro, Black Hole Emergence in Supernovae. Astrophys. J. **541** (2), 860–882 (2000), doi:10.1086/309472.

54. T. Sukhbold, T. Ertl, S. E. Woosley, J. M. Brown, H. T. Janka, Core-collapse Supernovae from 9 to 120 Solar Masses Based on Neutrino-powered Explosions. Astrophys. J. **821** (1), 38 (2016), doi:10.3847/0004-637X/821/1/38.

55. L. Boccioli, L. Roberti, The Physics of Core-Collapse Supernovae: Explosion Mechanism and Explosive Nucleosynthesis. *Universe* **10** (3), 148 (2024), doi:10.3390/universe10030148.

56. S. M. Adams, C. S. Kochanek, J. R. Gerke, K. Z. Stanek, The search for failed supernovae with the Large Binocular Telescope: constraints from 7 yr of data. Mon. Not. R. Astron. Soc. **469** (2), 1445–1455 (2017), doi:10.1093/mnras/stx898.

57. R. A. Byrne, M. Fraser, Nothing to see here: failed supernovae are faint or rare. Mon. Not. R. Astron. Soc. **514** (1), 1188–1205 (2022), doi:10.1093/mnras/stac1308.

58. K. De, Data and models for M31-2014-DS1, `https://doi.org/10.5281/zenodo.17774115` (2025), doi:10.5281/zenodo.17774115.

59. E. L. Wright, *et al.*, The Wide-field Infrared Survey Explorer (WISE): Mission Description and Initial On-orbit Performance. *Astron. J.* **140** (6), 1868–1881 (2010), doi:10.1088/0004-6256/140/6/1868.

60. D. Lang, unWISE: Unblurred Coadds of the WISE Imaging. *Astron. J.* **147** (5), 108 (2014), doi:10.1088/0004-6256/147/5/108.

61. A. M. Meisner, D. Lang, D. J. Schlegel, Time-resolved WISE/NEOWISE Coadds. *Astron. J.* **156** (2), 69 (2018), doi:10.3847/1538-3881/aacbcd.

62. B. Zackay, E. O. Ofek, A. Gal-Yam, Proper Image Subtraction - Optimal Transient Detection, Photometry, and Hypothesis Testing. *Astrophys. J.* **830**, 27 (2016), doi:10.3847/0004-637X/830/1/27.

63. S. van der Walt, A. Crellin-Quick, J. Bloom, SkyPortal: An Astronomical Data Platform. *The Journal of Open Source Software* **4** (37), 1247 (2019), doi:10.21105/joss.01247.

64. Gaia Collaboration, *et al.*, Gaia Early Data Release 3. Summary of the contents and survey properties. *Astron. & Astrophys.* **649**, A1 (2021), doi:10.1051/0004-6361/202039657.

65. N. M. Law, *et al.*, The Palomar Transient Factory: System Overview, Performance, and First Results. Publ. Astron. Soc. Pac. **121** (886), 1395 (2009), doi:10.1086/648598.

66. A. Rau, *et al.*, Exploring the Optical Transient Sky with the Palomar Transient Factory. Publ. Astron. Soc. Pac. **121** (886), 1334 (2009), doi:10.1086/605911.

67. E. O. Ofek, *et al.*, The Palomar Transient Factory photometric catalog 1.0. Publ. Astron. Soc. Pac. **124** (918), 854 (2012), doi:10.1086/666978.

68. K. C. Chambers, *et al.*, The Pan-STARRS1 Surveys. *arXiv e-prints* arXiv:1612.05560 (2016).

69. H. A. Flewelling, *et al.*, The Pan-STARRS1 Database and Data Products. Astrophys. J. Suppl. **251** (1), 7 (2020), doi:10.3847/1538-4365/abb82d.

70. D. W. Evans, *et al.*, Gaia Data Release 3. The Gaia Andromeda Photometric Survey. Astron. & Astrophys. **674**, A4 (2023), doi:10.1051/0004-6361/202244204.

71. E. C. Bellm, *et al.*, The Zwicky Transient Facility: System Overview, Performance, and First Results. Publ. Astron. Soc. Pac. **131** (1), 018002 (2019), doi:10.1088/1538-3873/aaecbe.

72. F. J. Masci, *et al.*, The Zwicky Transient Facility: Data Processing, Products, and Archive. Publ. Astron. Soc. Pac. **131** (1), 018003 (2019), doi:10.1088/1538-3873/aae8ac.

73. J. J. Dalcanton, *et al.*, The Panchromatic Hubble Andromeda Treasury. Astrophys. J. Suppl. **200** (2), 18 (2012), doi:10.1088/0067-0049/200/2/18.

74. A. E. Dolphin, WFPC2 Stellar Photometry with HSTPHOT. Publ. Astron. Soc. Pac. **112**, 1383–1396 (2000), doi:10.1086/316630.

75. A. Dolphin, DOLPHOT: Stellar photometry, Astrophysics Source Code Library, record ascl:1608.013 (2016).

76. B. F. Williams, *et al.*, The Panchromatic Hubble Andromeda Treasury. X. Ultraviolet to Infrared Photometry of 117 Million Equidistant Stars. Astrophys. J. Suppl. **215** (1), 9 (2014), doi:10.1088/0067-0049/215/1/9.

77. R. C. Bohlin, Perfecting the Photometric Calibration of the ACS CCD Cameras. Astron. J. **152** (3), 60 (2016), doi:10.3847/0004-6256/152/3/60.

78. Space Telescope Science Institute (STScI), Photometric Calibration — WFC3 Data Analysis, `https://www.stsci.edu/hst/instrumentation/wfc3/data-analysis/photometric-calibration` (2025), `https://www.stsci.edu/hst/instrumentation/wfc3/data-analysis/photometric-calibration`, last updated 16 June 2025.

79. H. I. Teplitz, *et al.*, The Spitzer Source List, in *Astronomical Data Analysis Software and Systems XIX*, Y. Mizumoto, K. I. Morita, M. Ohishi, Eds., vol. 434 of *Astronomical Society of the Pacific Conference Series* (2010), p. 437.

80. G. G. Fazio, *et al.*, The Infrared Array Camera (IRAC) for the Spitzer Space Telescope. Astrophys. J. Suppl. **154** (1), 10–17 (2004), doi:10.1086/422843.

81. G. H. Rieke, *et al.*, The Multiband Imaging Photometer for Spitzer (MIPS). Astrophys. J. Suppl. **154** (1), 25–29 (2004), doi:10.1086/422717.

82. D. Fabricant, *et al.*, Binospec: A Wide-field Imaging Spectrograph for the MMT. Publ. Astron. Soc. Pac. **131** (1001), 075004 (2019), doi:10.1088/1538-3873/ab1d78.

83. J. T. Rayner, *et al.*, SpeX: A Medium-Resolution 0.8-5.5 Micron Spectrograph and Imager for the NASA Infrared Telescope Facility. Publ. Astron. Soc. Pac. **115** (805), 362–382 (2003), doi:10.1086/367745.

84. I. S. McLean, *et al.*, MOSFIRE, the multi-object spectrometer for infra-red exploration at the Keck Observatory, in *Ground-based and Airborne Instrumentation for Astronomy IV*, I. S. McLean, S. K. Ramsay, H. Takami, Eds., vol. 8446 of *Society of Photo-Optical Instrumentation Engineers (SPIE) Conference Series* (2012), p. 84460J, doi:10.1117/12.924794.

85. J. C. Wilson, *et al.*, Mass producing an efficient NIR spectrograph, in *Ground-based Instrumentation for Astronomy*, A. F. M. Moorwood, M. Iye, Eds., vol. 5492 of *Society of Photo-Optical Instrumentation Engineers (SPIE) Conference Series* (2004), pp. 1295–1305, doi:10.1117/12.550925.

86. M. C. Cushing, W. D. Vacca, J. T. Rayner, Spextool: A Spectral Extraction Package for SpeX, a 0.8-5.5 Micron Cross-Dispersed Spectrograph. Publ. Astron. Soc. Pac. **116**, 362–376 (2004), doi:10.1086/382907.

87. W. D. Vacca, M. C. Cushing, J. T. Rayner, A Method of Correcting Near-Infrared Spectra for Telluric Absorption. Publ. Astron. Soc. Pac. **115**, 389–409 (2003), doi:10.1086/346193.

88. A. Fruscione, *et al.*, CIAO: Chandra's data analysis system, in *Society of Photo-Optical Instrumentation Engineers (SPIE) Conference Series*, D. R. Silva, R. E. Doxsey, Eds., vol. 6270 of *Society of Photo-Optical Instrumentation Engineers (SPIE) Conference Series* (2006), p. 62701V, doi:10.1117/12.671760.

89. D. E. Graessle, *et al.*, The Chandra X-ray Observatory calibration database (CalDB): building, planning, and improving, in *Observatory Operations: Strategies, Processes, and Systems*, D. R. Silva, R. E. Doxsey, Eds., vol. 6270 of *Society of Photo-Optical Instrumentation Engineers (SPIE) Conference Series* (2006), p. 62701X, doi:10.1117/12.672876.

90. HI4PI Collaboration, *et al.*, HI4PI: A full-sky H I survey based on EBHIS and GASS. Astron. & Astrophys. **594**, A116 (2016), doi:10.1051/0004-6361/201629178.

91. A. Savino, *et al.*, The Hubble Space Telescope Survey of M31 Satellite Galaxies. I. RR Lyrae-based Distances and Refined 3D Geometric Structure. Astrophys. J. **938** (2), 101 (2022), doi:10.3847/1538-4357/ac91cb.

92. P. A. Evans, *et al.*, An online repository of Swift/XRT light curves of γ-ray bursts. Astron. & Astrophys. **469** (1), 379–385 (2007), doi:10.1051/0004-6361:20077530.

93. P. A. Evans, *et al.*, Methods and results of an automatic analysis of a complete sample of Swift-XRT observations of GRBs. Mon. Not. R. Astron. Soc. **397** (3), 1177–1201 (2009), doi:10.1111/j.1365-2966.2009.14913.x.

94. K. K. Madsen, *et al.*, Calibration of the NuSTAR High-energy Focusing X-ray Telescope. Astrophys. J. Suppl. **220** (1), 8 (2015), doi:10.1088/0067-0049/220/1/8.

95. K. K. Madsen, K. Forster, B. Grefenstette, F. A. Harrison, H. Miyasaka, Effective area calibration of the Nuclear Spectroscopic Telescope Array. *Journal of Astronomical Telescopes, Instruments, and Systems* **8**, 034003 (2022), doi:10.1117/1.JATIS.8.3.034003.

96. Z. Ivezic, M. Elitzur, Self-similarity and scaling behaviour of infrared emission from radiatively heated dust - I. Theory. *Mon. Not. R. Astron. Soc.* **287** (4), 799–811 (1997), doi:10.1093/mnras/287.4.799.

97. Z. Ivezic, M. Nenkova, M. Elitzur, User Manual for DUSTY. *arXiv e-prints* astro-ph/9910475 (1999).

98. T. Verhoelst, *et al.*, The dust condensation sequence in red supergiant stars. Astron. & Astrophys. **498** (1), 127–138 (2009), doi:10.1051/0004-6361/20079063.

99. J. S. Mathis, W. Rumpl, K. H. Nordsieck, The size distribution of interstellar grains. *Astrophys. J.* **217**, 425–433 (1977), doi:10.1086/155591.

100. K. De, *et al.*, SRGA J181414.6-225604: A New Galactic Symbiotic X-Ray Binary Outburst Triggered by an Intense Mass-loss Episode of a Heavily Obscured Mira Variable. Astrophys. J. **935** (1), 36 (2022), doi:10.3847/1538-4357/ac7c6e.

101. D. Foreman-Mackey, D. W. Hogg, D. Lang, J. Goodman, emcee: The MCMC Hammer. Publ. Astron. Soc. Pac. **125** (925), 306 (2013), doi:10.1086/670067.

102. E. L. Fitzpatrick, Correcting for the Effects of Interstellar Extinction. Publ. Astron. Soc. Pac. **111** (755), 63–75 (1999), doi:10.1086/316293.

103. E. F. Schlafly, D. P. Finkbeiner, Measuring Reddening with Sloan Digital Sky Survey Stellar Spectra and Recalibrating SFD. Astrophys. J. **737** (2), 103 (2011), doi:10.1088/0004-637X/737/2/103.

104. H. Sana, *et al.*, Binary Interaction Dominates the Evolution of Massive Stars. *Science* **337** (6093), 444 (2012), doi:10.1126/science.1223344.

105. K. F. Neugent, E. M. Levesque, P. Massey, N. I. Morrell, M. R. Drout, The Red Supergiant Binary Fraction of the Large Magellanic Cloud. Astrophys. J. **900** (2), 118 (2020), doi: 10.3847/1538-4357/ababaa.

106. K. F. Neugent, E. M. Levesque, P. Massey, Binary Red Supergiants: A New Method for Detecting B-type Companions. Astron. J. **156** (5), 225 (2018), doi:10.3847/1538-3881/aae4e0.

107. K. F. Neugent, The Red Supergiant Binary Fraction as a Function of Metallicity in M31 and M33. Astrophys. J. **908** (1), 87 (2021), doi:10.3847/1538-4357/abd47b.

108. P. Massey, K. F. Neugent, B. M. Smart, A Spectroscopic Survey of Massive Stars in M31 and M33. Astron. J. **152** (3), 62 (2016), doi:10.3847/0004-6256/152/3/62.

109. L. Dessart, E. Livne, R. Waldman, Shock-heating of stellar envelopes: a possible common mechanism at the origin of explosions and eruptions in massive stars. Mon. Not. R. Astron. Soc. **405** (4), 2113–2131 (2010), doi:10.1111/j.1365-2966.2010.16626.x.

110. J. A. Goldberg, L. Bildsten, B. Paxton, Inferring Explosion Properties from Type II-Plateau Supernova Light Curves. Astrophys. J. **879** (1), 3 (2019), doi:10.3847/1538-4357/ab22b6.

111. I. K. W. Kleiser, D. Kasen, Rapidly fading supernovae from massive star explosions. Mon. Not. R. Astron. Soc. **438** (1), 318–328 (2014), doi:10.1093/mnras/stt2191.

112. B. Paxton, *et al.*, Modules for Experiments in Stellar Astrophysics (MESA). Astrophys. J. Suppl. **192** (1), 3 (2011), doi:10.1088/0067-0049/192/1/3.

113. A. S. Jermyn, *et al.*, Modules for Experiments in Stellar Astrophysics (MESA): Time-dependent Convection, Energy Conservation, Automatic Differentiation, and Infrastructure. Astrophys. J. Suppl. **265** (1), 15 (2023), doi:10.3847/1538-4365/acae8d.

114. Y.-F. Jiang, Three Dimensional Natures of Massive Star Envelopes. *Galaxies* **11** (5), 105 (2023), doi:10.3390/galaxies11050105.

115. M. Renzo, C. D. Ott, S. N. Shore, S. E. de Mink, Systematic survey of the effects of wind mass loss algorithms on the evolution of single massive stars. Astron. & Astrophys. **603**, A118 (2017), doi:10.1051/0004-6361/201730698.

116. E. R. Coughlin, E. Quataert, R. Fernández, D. Kasen, A physical model of mass ejection in failed supernovae. Mon. Not. R. Astron. Soc. **477** (1), 1225–1238 (2018), doi:10.1093/mnras/sty667.

117. E. R. Coughlin, E. Quataert, S. Ro, Weak Shock Propagation with Accretion. I. Self-similar Solutions and Application to Failed Supernovae. Astrophys. J. **863** (2), 158 (2018), doi:10.3847/1538-4357/aad198.

118. A. Gilkis, N. Soker, Triggering jet-driven explosions of core-collapse supernovae by accretion from convective regions. Mon. Not. R. Astron. Soc. **439** (4), 4011–4017 (2014), doi:10.1093/mnras/stu257.

119. A. Antoni, E. Quataert, Numerical simulations of the random angular momentum in convection: Implications for supergiant collapse to form black holes. Mon. Not. R. Astron. Soc. **511** (1), 176–197 (2022), doi:10.1093/mnras/stab3776.

120. W. Xu, Simple Convective Accretion Flows (SCAFs): Explaining the ≈ -1 Density Scaling of Hot Accretion Flows around Compact Accretors. Astrophys. J. **954** (2), 180 (2023), doi:10.3847/1538-4357/ace892.

121. S.-C. Yoon, L. Dessart, A. Clocchiatti, Type Ib and IIb Supernova Progenitors in Interacting Binary Systems. Astrophys. J. **840** (1), 10 (2017), doi:10.3847/1538-4357/aa6afe.

Acknowledgments

We thank the anonymous referees for a careful review of the manuscript and providing constructive feedback for improving its contents. We thank H. Gupta, K. Das and P. Nair for assistance with the observations. We thank S. R. Kulkarni, L. Hillenbrand, J. Goldberg and C. Conroy for valuable discussions. Data were obtained at the W. M. Keck Observatory from telescope time allocated to the National Aeronautics and Space Administration through the agency's scientific partnership with the California Institute of Technology and the University of California. The Observatory was made possible by the generous financial support of the W. M. Keck Foundation. The authors wish to recognize and acknowledge the very important cultural role and reverence that the summit of

Maunakea has always had within the indigenous Hawaiian community. We are most fortunate to have the opportunity to conduct observations from this mountain. This research has made use of the Keck Observatory Archive (KOA), which is operated by the W. M. Keck Observatory and the NASA Exoplanet Science Institute (NExScI), under contract with the National Aeronautics and Space Administration. We acknowledge the Visiting Astronomer Facility at the Infrared Telescope Facility, which is operated by the University of Hawaii under contract 80HQTR19D0030 with the National Aeronautics and Space Administration.

Funding: K. D. was supported by NASA through the NASA Hubble Fellowship grant #HST-HF2-51477.001 awarded by the Space Telescope Science Institute, which is operated by the Association of Universities for Research in Astronomy, Inc., for NASA, under contract NAS5-26555. K. D.'s data analysis was supported by NASA through a Keck PI Data Award, administered by the NASA Exoplanet Science Institute and through ADAP grant number 80NSSC24K0663. M.MacLeod was supported by a Clay postdoctoral fellowship at the Smithsonian Astrophysical Observatory. A.A. was supported by the Simons Foundation through a Flatiron Research Fellowship. E.Q.'s work benefited from interactions at workshops funded by the Gordon and Betty Moore Foundation through grant GBMF5076.

Author contributions: K.D. identified the object, initiated follow-up observations, carried out the analysis and wrote the manuscript. M.MacLeod developed theoretical models and helped write the manuscript. J.E.J. analyzed the archival space telescope data and R.M.L. assisted with the observational interpretation. A.A., A.L., E.L. and E.Q. contributed to the theoretical interpretation and modeling. M.M.K. and R.S. assisted with ground-based observational follow-up. E.K., M.Masterson and C.P. performed the X-ray data analysis. A.M.M. produced the time-resolved stacks of WISE images. All authors contributed to the scientific interpretation.

Competing interests: There are no competing interests to declare.

Data and materials availability: The photometric data, image subtraction tools and theoretical stellar evolution models and failed supernova calculations are available at `https://github.com/dekishalay/M31-2014-DS1/` and archived on Zenodo (*58*). The NEOWISE images can be

accessed at http://byw.tools/wiseview by providing the source coordinates. The image subtraction photometry code used for the NEOWISE images can be found at https://github.com/dekishalay/M31-2014-DS1/ and Zenodo (*58*). The Gaia photometry can be accessed at https://vizier.cds.unistra.fr/viz-bin/VizieR-3?-source=I/355/epphot by providing the source coordinates. The PTF light curves can be accessed at https://irsa.ipac.caltech.edu/cgi-bin/Gator/nph-scan?submit=Select&projshort=PTF by providing the source coordinates. The ZTF light curves can be produced at https://ztfweb.ipac.caltech.edu/cgi-bin/requestForcedPhotometry.cgi by providing the source coordinates. The MMT images can be accessed at https://www.mmto.org/cfa-optical-infrared-science-archive/ using the source coordinates. The PanSTARRS light curves can be accessed at https://catalogs.mast.stsci.edu/panstarrs by providing the source coordinates. The HST images can be accessed at https://mast.stsci.edu/portal/Mashup/Clients/Mast/Portal.html by providing the source coordinates and using Program IDs 12111, 14072 and 16730. The Spitzer photometry can be accessed at https://vizier.cds.unistra.fr/viz-bin/VizieR?-source=II/368 by providing the source coordinates. The Keck images and spectra can be accessed at https://koa.ipac.caltech.edu/cgi-bin/KOA/nph-KOAlogin using Program IDs 2023B_N258 and 2023B_N258. The IRTF data can be accessed at https://irsa.ipac.caltech.edu/applications/irtf/ using Program ID 2023B053.

Supplementary materials

Materials and Methods

Supplementary Text

Figs. S1 to S12

Tables S1 to S2

References *(59-121)*

Supplementary Materials for

Disappearance of a massive star in the Andromeda Galaxy due to formation of a black hole

Kishalay De*, Morgan MacLeod, Jacob E. Jencson, Elizabeth Lovegrove,Andrea Antoni, Erin Kara, Mansi M. Kasliwal, Ryan M. Lau, Abraham Loeb,Megan Masterson, Aaron M. Meisner, Christos Panagiotou, Eliot Quataert, and Robert Simcoe

*Corresponding author. Email: kd3038@columbia.edu

This PDF file includes:

Materials and Methods

Identification in NEOWISE

The Wide-field Infrared Survey Explorer (WISE) satellite (*59*), and its extended mission NEOWISE (*20*), performed all-sky MIR survey in the $W1$ (3.4 μm) and $W2$ (4.6 μm) bands since 2014; we use data up to 2022. NEOWISE revisits each part of the sky once every ≈ 0.5 yr. We searched for transients in time-resolved coadded images produced as part of the unWISE project (*60, 61*). We used the ZOGY algorithm (*62*) to perform image subtraction on the NEOWISE images using the co-added images of the WISE mission (obtained in 2010-2011) as reference images. The pipeline produces a database of all transients with statistical significance of $\gtrsim 10\sigma$. Follow-up for the sources was coordinated using the `fritz` astronomical data platform (*63*).

We applied selection criteria to the catalog of WISE transients to identify luminous MIR outbursts spatially coincident with M31 and M33 satisfying the following criteria:

1. Transient located within 4 degrees of the nucleus of M31 or M33.

2. The source brightened from the reference image and had no prior history of outbursts or variability in WISE data before the flagged brightening. The transient was detected in at least two consecutive epochs, to reject foreground moving objects.

3. The transient was not coincident with a foreground Galactic star, determined from the parallax and proper motion measurements from Gaia Data Release 3 (*64*).

4. The transient has peak MIR luminosity of $\gtrsim 10^{37}$ erg s^{-1}, chosen to select outbursts that reach the expected Eddington luminosity for a ≈ 0.1 to 1 $M_\odot$ star, while excluding lower luminosity IR outbursts from young stars and X-ray binaries.

We identified the source WTP 16aathhy (internal alphanumeric code in the database), initially as a candidate nova, at a projected separation of $\approx 0.54^\circ$ (≈ 7 kpc) from the nucleus of M31. The transient was identified at $> 10\sigma$ significance in difference imaging for the NEOWISE observation of the field in 2016 July (MJD 57591.79) at a (host subtracted) magnitude of $W2 = 17.91 \pm 0.10$ AB mag. The transient is coincident with an optical point source in archival ground-based imaging and Gaia DR3. Given the lower spatial resolution of WISE, we adopt the Gaia coordinates

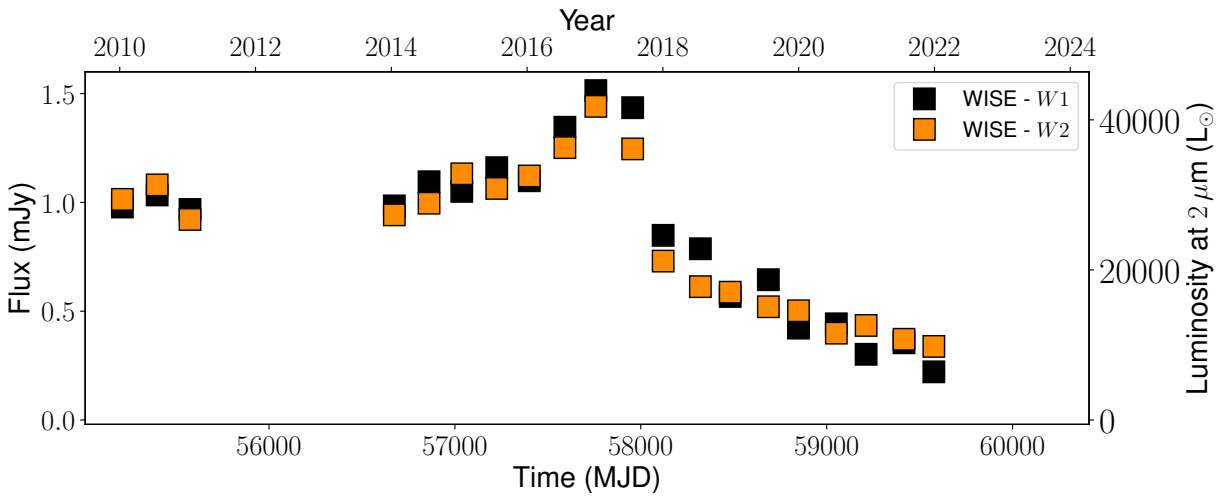

Figure S1: **NEOWISE light curve of M31-2014-DS1**. Same as Figure 2, but showing only the NEOWISE data and on a linear vertical scale.

of the optical source. The optical source parallax is consistent with zero (= 0.09±0.23 mas) as are the proper motions in the right ascension ($\mu_{\rm RA} = -0.17 \pm 0.17$) and declination ($\mu_{\rm Dec} = -0.10 \pm 0.21$) (*64*), indicating it is not a foreground Galactic star. We performed forced photometry on the NEOWISE difference images at the Gaia position, finding the IR brightening of the source began in the first NEOWISE visit of the field on MJD 56674.19 (Figure S1), followed by a brightening by 50% over the next $\approx$ 1000 d. We nominally adopt the time of the first NEOWISE visit as the reference time for our analysis, and designate the source as M31-2014-DS1 based on the onset year of the event and its subsequent identification as a disappearing star. The exact time of the start of the IR brightening is not well constrained.

Archival photometry

The progenitor of M31-2014-DS1 has been reported in historical archival optical and infrared source catalogs. It was previously considered as an irregular variable star in the field of M31 (*22*) and designated as V7984 M31B. We searched for archival time resolved photometry of the source from ground and space-based surveys. The field was observed with the PTF (*65, 66*) between 2010 and 2014 in the r-filter; we retrieved time resolved photometry of the source from the survey archive (*67*). The source was observed in the $grizy$ filters by the PS1 survey (*68*) between 2010 and

2014; we retrieved the point source photometry from the online source catalog (*69*). We retrieved optical photometry of the source between 2014 and 2017 in the Gaia G, BP and RP passbands from the Gaia-Andromeda survey (*70*) in Gaia DR3. This was observed as part of the Zwicky Transient Facility (ZTF (*71*)) optical survey between 2018 and 2024, but there is no source detected at that position in g and r-bands, in either the stacked reference image or individual epochs of observation. We derive 5σ upper limits on the source flux from forced Point Spread Function (PSF) photometry on the ZTF difference images (*72*), and stacking the non-detection upper limits in bins of 60 d. The archival light curve is shown in Figure 2, and all photometry is provided in the online data repository.

The source was serendipitously observed by the HST and SST at multiple epochs between 2005 and 2022. We analyzed the available HST imaging from 2012 taken with the Advanced Camera for Surveys (ACS; F475W, F814W filters) and Wide Field Camera 3 (WFC3) in both the Ultraviolet-Visible (UVIS; F336W, F275W filters) and Infrared (IR; F110W, F160W filters) channels as part of the Panochromatic Hubble Andromeda Treasury (PHAT) program (*73*), as well as the 2016 ACS/Wide Field Camera (WFC) imaging in F625W and 2022 WFC3/UVIS imaging in F606W and F814W. We processed the available HST images with `DOLPHOT` (*74, 75*) to obtain PSF-fitting photometry of M31-2014-DS1. As inputs to `DOLPHOT`, we use the Charge Tranfer Efficiency-corrected `flc` frames for ACS/WFC and WFC3/UVIS and `flt` frames for WFC3/IR downloaded from the Mikulski Archive for Space Telescopes. We adopt the `DOLPHOT` parameter settings for each camera as used by PHAT (*73, 76*). We ran `DOLPHOT` separately for each instrument and filter combination over the available epochs, using the drizzled 2012 F814W mosaic as a common reference image for alignment across all runs. `DOLPHOT` computes and applies aperture corrections to a radius of 0.5″ for the reported photometry. We then corrected to infinite apertures for each instrument and filter combination (*77, 78*). We retrieved SST photometry of the source in 2005 from the Spitzer source list (*79*). The photometry was acquired with the Infrared Array Camera (IRAC (*80*)) in Channels 1 (3.6 µm), 2 (4.5 µm), 3 (5.8 µm) and 4 (8.0 µm), and using the Multiband Imaging Photometer for Spitzer (MIPS (*81*)) in Channel 1 (24.0 µm). We use the measurements from 2012 and 2022 to characterize the progenitor and remnant of M31-2014-DS1, and list them in Table S1.

Follow-up imaging

We obtained follow-up optical imaging of the source using the Binospec instrument (*82*) on the MMT telescope. Observations were obtained between Coordinated Universal Time (UTC) 2023 October 18 and 2023 October 19, consisting of dithered exposures of the field with total exposure time of 2400 s and 1800 s in the g and r filters respectively. The data were reduced, stacked and calibrated against the PS1 catalog. We performed aperture photometry at the position of the source, and derive 5σ upper limits of $r > 22.44$ mag and $g > 22.96$ mag, limited primarily by source confusion in the dense field.

We obtained near-infrared imaging of the source using the SpeX instrument (*83*) on the NASA Infrared Telescope Facility on UTC 2023 September 06. A series of dithered exposures were obtained with a total exposure time of 1200 s in both J and K filters. The images were reduced, stacked and calibrated against the 2MASS catalog. No source is detected at the transient position, with a 5σ limiting magnitude of $J > 19.0$ mag and $K > 17.8$ mag.

We obtained deeper near-infrared imaging using the Multi-Object Spectrometer For Infrared Exploration (MOSFIRE (*84*)) on the Keck-I telescope, on UTC 2023 December 25. The source was observed over multiple dithered exposures with a total exposure time of 288 s and 297 s in J and K bands respectively. High winds during the K-band observations led us to discard those images. Performing aperture photometry at the source position, a faint source is detected in the J-band images at $J = 20.90 \pm 0.28$ Vega mag.

Follow-up infrared spectroscopy

On UTC 2023 September 04, we obtained follow-up $1.0 - 2.5$ μm near-infrared spectroscopy of the source using the Near Infrared Echelle Spectrometer (NIRES (*85*)) on the Keck-II telescope. Due to the faintness of the source, it was acquired by centering a nearby bright star in the slit followed by applying a blind offset using the Gaia coordinates. We obtained a series of dithered exposures in the ABBA pattern with a total exposure time of 2400 s. We reduced the data using the `spextool` (*86*) software, followed by flux calibration and telluric correction using the `xtellcor` (*87*) package. A faint source is detected in the spectral trace in H and K bands, with a nearly featureless spectrum brightening towards longer wavelengths, shown in Figure 4 and Figure S2.

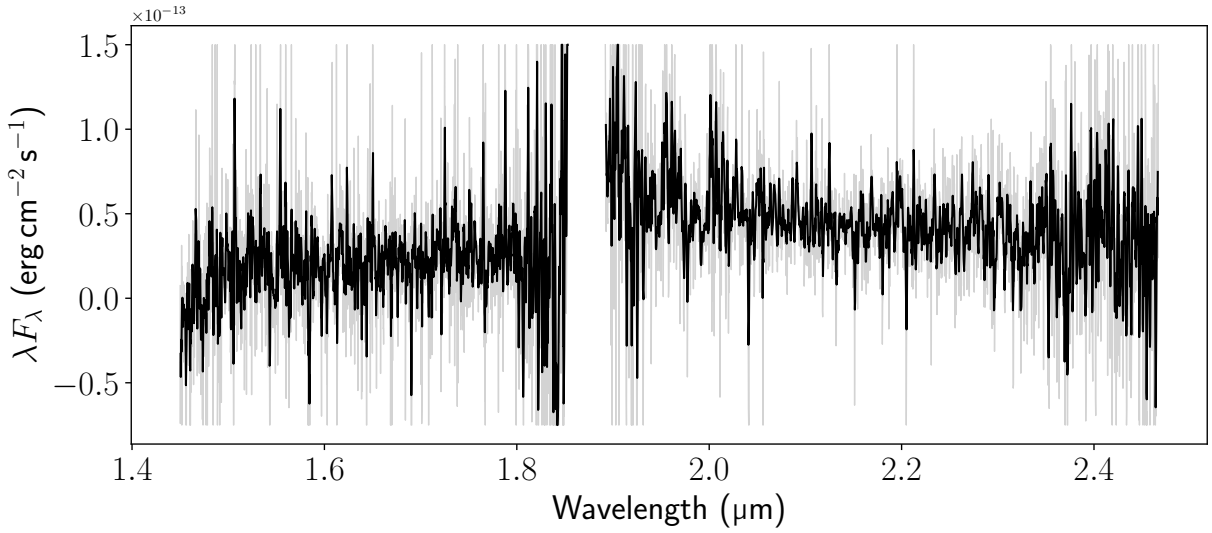

Figure S2: **NIRES spectrum of M31-2014-DS1**. Grey lines show the raw spectrum and black lines show the spectrum binned by averaging every five points to improve the signal-to-noise ratio.

X-ray observations

To constrain the X-ray luminosity of M31-2014-DS1, we retrieved archival observations of the source location by the Chandra X-ray telescope. The source was within the field of view of a 50 ks *Chandra* Advanced CCD Imaging Spectrometer-I observation in 2015. We reduced the data using CIAO (*88*) (version 4.16) and CALDBv4.11.0 (*89*), finding no source at the Gaia position. Using the `aplimits` tool (*88*) and following published procedures, we estimate a 3σ upper limit on the X-ray flux $F_X \lesssim 2.0 \times 10^{-15}$ erg s^{-1} cm^{-2} in the 0.5-7 keV band. This limit was calculated using a circular source region with a radius of $5''$ and by assuming a power-law spectrum (number of photons $N \propto E^{-\Gamma}$, where E is the photon energy and $\Gamma = 2$ is the assumed photon index) with Galactic absorption (*90*) corresponding to a hydrogen column density $N_H = 2.26 \times 10^{21}$ cm^{-2}. At a distance of 770 kpc (*91*), this corresponds to an X-ray luminosity $L_X \lesssim 1.4 \times 10^{35}$ erg s^{-1}.

We also searched the Swift archive for observations within $12'$ of the source after 2015, finding four observations in July 2020. Using the XRT products generator (*92, 93*), we stacked these observations ($\approx$ 4 ks in total) and set a 3σ upper limit of $F_X \lesssim 1.3 \times 10^{-13}$ erg s^{-1} cm^{-2} in the 0.3-10 keV band, assuming the same power-law as for the Chandra observations. Without correcting for any intrinsic absorption, this corresponds to $L_X \lesssim 8.9 \times 10^{36}$ erg s^{-1}.

The Gaia position was also observed serendipitously by NuSTAR four times in 2015. We followed standard procedure (*94*) to reduce the observational data using the *nupipeline* and *nuproducts* tools of the *NuSTAR* Data Analysis Software (NuSTARDAS) package version 2.1.2 (*94*) and the corresponding CALDBv20240422 (*95*). No source at the Gaia position is detected in any of the observations. Assuming the same power-law spectrum, we estimated a stacked 3σ upper limit 2-10 keV flux $F_X \lesssim 2.2 \times 10^{-14}$ erg s^{-1} cm^{-2}, which corresponds to $L_X \lesssim 1.6 \times 10^{36}$ erg s^{-1}.

DUSTY modeling

M31-2014-DS1 exhibits excess MIR emission throughout its evolution from 2014 to 2022, indicating dust surrounding the star. We model the optical to MIR SED of the transient to estimate the properties of the central star and circumstellar dust shell, and their evolution over time. We use the dust radiative dust transfer code DUSTY V4 (*96, 97*) to produce models that are fitted to the multi-wavelength data. We assume a spherically symmetric distribution of the dust with a radial density profile that changes with radius r as $\propto r^{-2}$ around the star, which is assumed to be a point source. We assume the dust grains are composed of warm silicates, as expected for massive supergiants (*98*), and a grain size distribution from (*99*) – with minimum and maximum grain sizes of $a_{\rm min} = 0.005\,\mu$m and $a_{\rm max} = 0.25\,\mu$m.

We fitted the progenitor photometry from HST and SST using a Markov Chain Monte Carlo (MCMC) wrapper around the DUSTY code (*100*) using the Python `emcee` library (*101*). We model the foreground wavelength dependent interstellar extinction using a standard relation (*102*) extending from ultraviolet to the MIR. The free parameters of the model are the dust optical depth at 0.55 μm (τ_V), the foreground visual extinction (A_V), the inner stellar temperature (T_*), the dust temperature at the inner edge of the shell (T_d), the ratio of the outer to inner radius of the shell (Y) and the total flux (F). We assume flat priors on all the free parameters and ensure convergence of the posterior sampling chains by checking for stabilization of the autocorrelation time to $< 1\%$ in consecutive steps. The posterior probability distributions are shown in Figure S3 and listed in Table S2.

We find the thickness Y to be poorly constrained because the wavelength coverage is primarily confined to the shorter wavelength MIR bands where the emission is dominated by the hotter, inner part of the dust shell. The best-fitting foreground extinction is consistent with the expected Milky Way extinction in this direction ($A_V \approx 0.1$ mag) (*103*), with no additional extinction within M31.

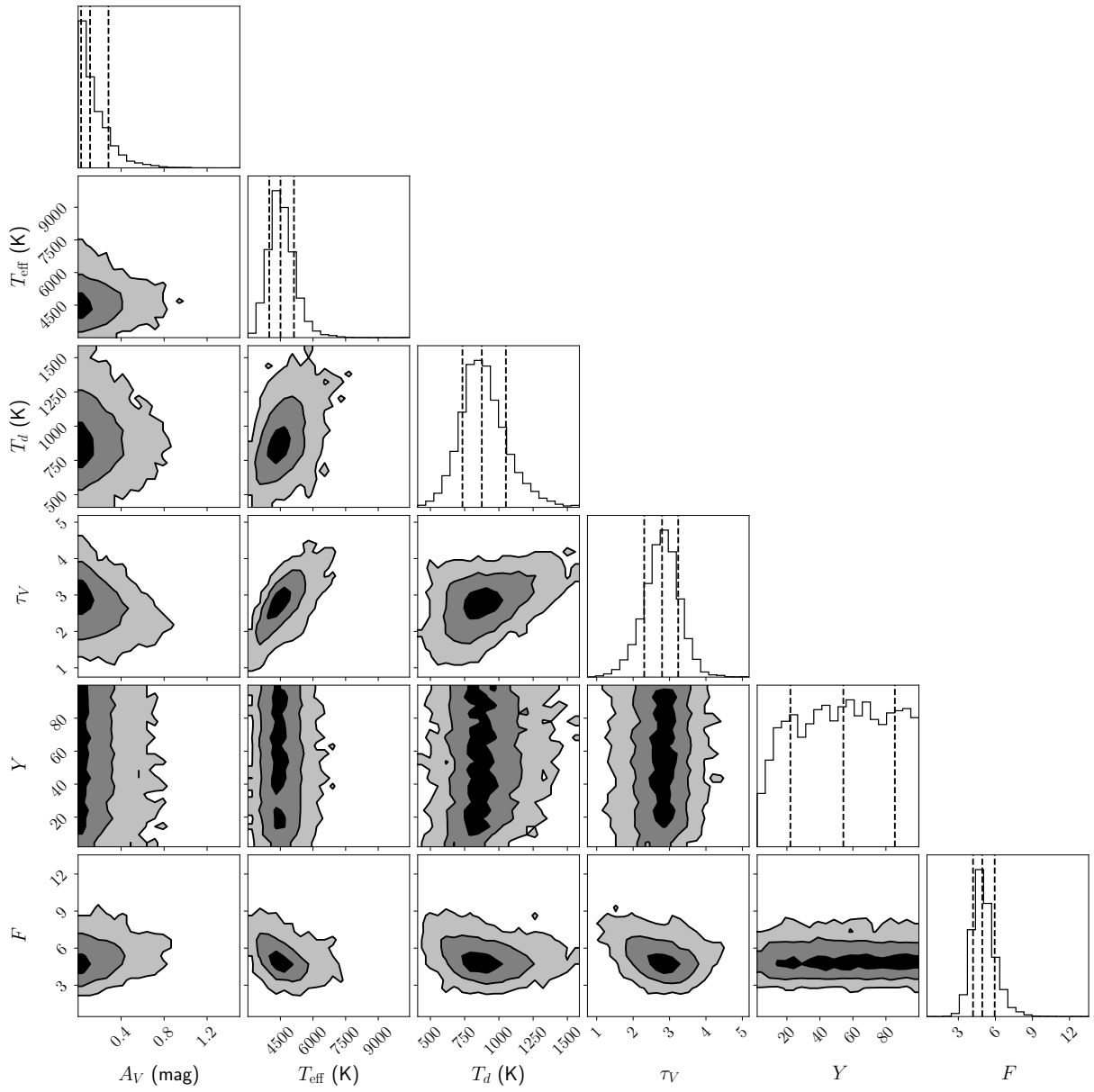

Figure S3: **Corner plot for the MCMC DUSTY modeling of the progenitor of M31-2014-DS1 in 2012.** F is in units of 10^{-12} erg cm^{-2} s^{-1}. The dark, medium and light shaded regions indicate contours enclosing 39%, 86% and 99% of the probability region for the respective parameters. The median of the posterior distributions and the corresponding 68% confidence intervals are shown as vertical dashed lines in the one dimensional histograms and listed in Table S2.

To constrain the SED of the remnant, we perform the same analysis using the HST, Keck and NEOWISE data obtained during $\approx 2022 - 2023$, fixing the foreground extinction to $A_V = 0.1$ mag and the thickness $Y = 10$ based on the progenitor model. Consistent with the optical disappearance

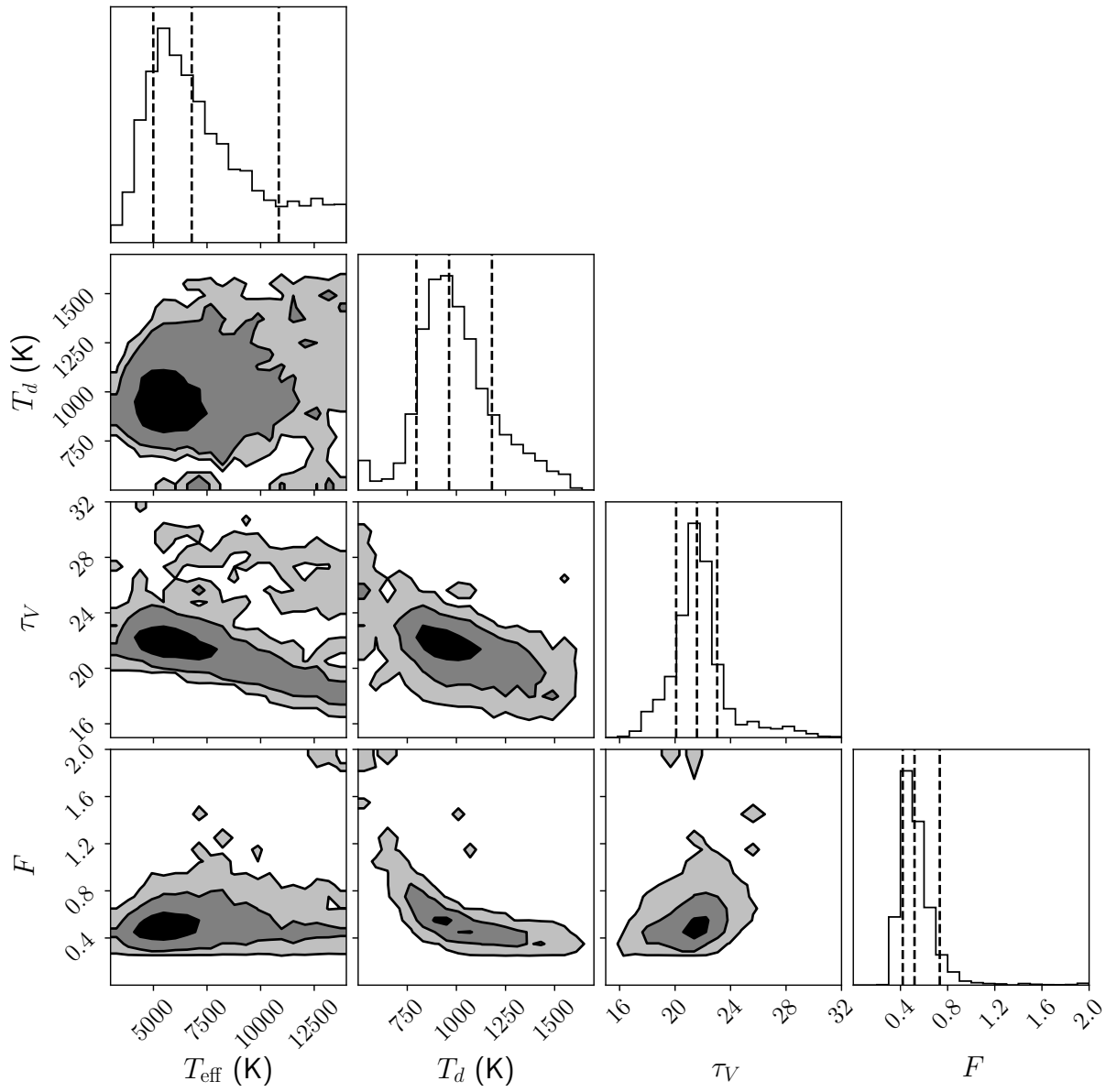

Figure S4: **Corner plots for the MCMC DUSTY modeling of the remnant of M31-2014-DS1 in 2022-2023.** Same as in Figure S3 but for the SED in 2022-2023. The median parameter values and their 68% confidence intervals are listed in Table S2; A_V and Y were fixed to their 2012 values.

and slow infrared fading, we find the remnant has a much higher optical depth and $\approx 10\times$ fainter bolometric flux (Figure S4 and Table S2).

A stellar companion to the massive progenitor star (*104*) could affect both the pre-disappearance and remnant photometry. Any companion is unlikely to be a similarly evolved cool star, given the

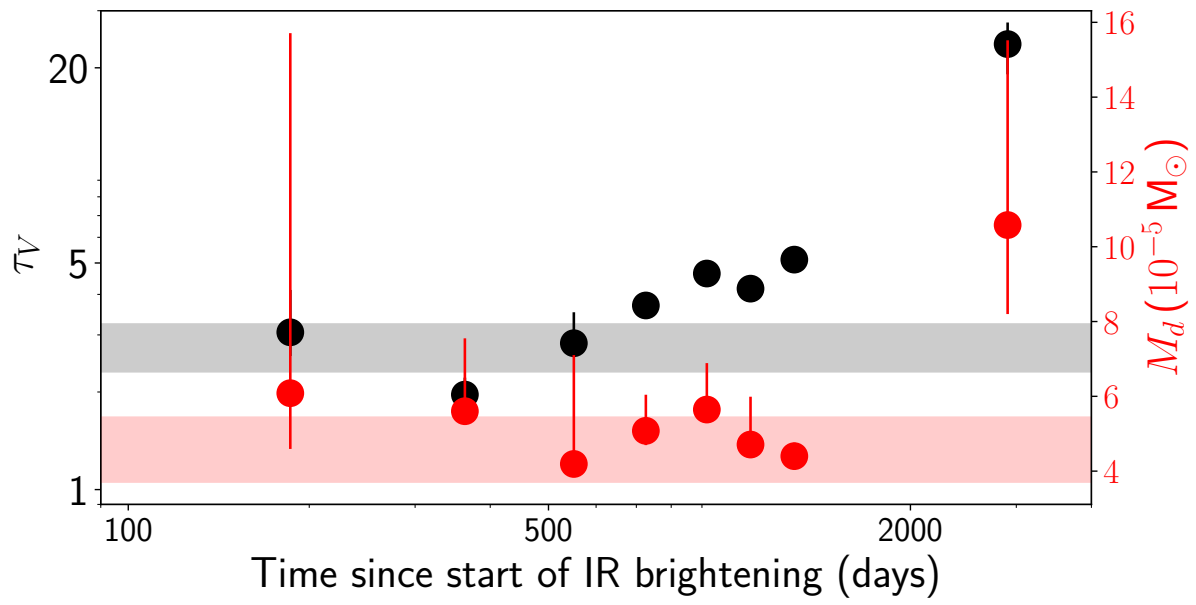

Figure S5: **Optical depth and total mass of circumstellar dust during the dimming episode**. Errors are shown at 1σ confidence level. Same as Figure 4A, but for the optical depth (black, left axis) and mass of dust in the circumstellar shell (red, right axis).

very short lifetime of this phase (*105*). For unevolved companions, lower mass (smaller than A-type dwarfs; $\lesssim 2.5\,\mathrm{M}_\odot$) stars are unlikely because the total lifetime of the RSG would be shorter than the pre-main sequence lifetime of the companion (*106*), while compact stellar remnants (e.g. a companion neutron star/BH) would have no observable effects on the observed photometry. Therefore, OB-type stellar companions are the only possible contaminants for the observed photometry, which would contribute excess emission at the bluest wavelengths ($\lesssim 5000\,$Å; (*106*)) because the cool supergiant outshines the companion in redder light (*107*). Previous analysis of stellar model grids has shown that such excess blue emission is identifiable in color-color space of $U-B$ and $R-I$ (*106*).

Based on the photometry of the progenitor (*108*), we find $U-B = 1.30 \pm 0.01$ and $R-I = 0.72 \pm 0.01$. The $U-B$ color is much redder than selection thresholds for RSG + OB type binaries ($U-B < 1$; (*105*)) and inconsistent with the entire binary RSG photometry model grid (*106*). Those models did not include yellow supergiants (YSGs) or RSGs with dust shells, but those would produce even bluer $U-B$ colors due to the hotter YSG star or decreased contribution of RSG emission at bluer wavelengths, respectively. Therefore, we find no evidence for a binary companion

in the progenitor photometry could affect the SED. A-type and lower mass stars are not likely given evolutionary age constraints; because stars in this lower mass range have optical luminosity $\lesssim 10\,L_\odot$, the observed optical fading of the star to already a few $L_\odot$(Figure 4) disfavors the effects of a binary companion on the remnant SED as observed in 2022-2023.

Dust evolution during the disappearance

To investigate the evolution of the source, we use the Gaia multi-color photometric coverage during the optical fading (Figure 2) and the NEOWISE photometry. Because the Gaia measurements are not simultaneous with the NEOWISE coverage, we average the Gaia measurements around the time of each NEOWISE observation (within 1.5 months of each epoch; Figure 2). For each NEOWISE epoch, we construct an optical (Gaia BP and RP) to MIR (NEOWISE $W1$ and $W2$) SED. We then perform the same SED fitting for these epochs as for the remnant modeling above. At each epoch, we estimate the total mass of dust in the shell as

$$M_d = \frac{4\pi\tau_V R_{\rm in}^2 Y}{\kappa_d} r_{\rm dg} \tag{S1}$$

where $R_{\rm in}$ is the radius of the inner shell, $\kappa_d \approx 50\,{\rm cm^2\,g^{-1}}$ is the average visual opacity per unit total mass (gas and dust) and $r_{\rm dg} \approx 0.01$ is the assumed dust-to-gas mass ratio relevant for the late-phase evolution of low energy explosions (*45, 46*). Adopting $Y = 10$, we find

$$M_d \approx 6.1\times10^{-8}{\rm M_\odot}\left(\frac{R_{in}}{1000\,{\rm R_\odot}}\right)^2 \tau_V \tag{S2}$$

The inferred progenitor optical depth indicates a wind-loading parameter $A = \dot{M}/4\pi\, v_w \approx 7\times 10^{13}\,{\rm g\,cm^{-1}}$, where $\dot{M}$ and v_w are the progenitor mass-loss rate and wind velocity, respectively. Taking $v_w \approx 50-100\,{\rm km\,s^{-1}}$, typical for YSGs with our inferred $T_{\rm eff}$ ($\approx 4500\,{\rm K}$; (*25*)), implies a high mass-loss rate of $\approx (1-2)\times10^{-4}\,{\rm M_\odot\ yr^{-1}}$. The subsequent evolution of the dust temperature, inner radius, inner source temperature and inferred photospheric radius are shown in Figure 4, while the evolution of the dust optical depth and total mass are shown in Figure S5. The evolution of the total source luminosity during this time is shown in Figure 5.

To estimate the source luminosity evolution between the end of the Gaia coverage in 2017 and the SED of the remnant in 2022, we estimate a bolometric correction between the MIR luminosity using trapezoidal integration of the NEOWISE fluxes and the total luminosity from the `DUSTY`

models for the last Gaia + NEOWISE epoch in 2017. We apply this bolometric correction to the NEOWISE MIR data from 2018 to 2022, which is shown in Figure 5.

This analysis shows a gradual increase in the dust temperature and a decrease in the inner shell radius (Figure 4A) and total luminosity, from the progenitor to the remnant in 2022. A similar trend is seen in the evolution of the stellar temperature and radius, with the remnant having a higher inferred temperature and smaller radius of $\approx 20\%$ of the progenitor star. We compare the evolution of the dust shell radius to the minimum radius at which dust can form around a luminous star, r_c, given by (*30*)

$$r_c \approx 11\,\mathrm{au} \left(\frac{L}{10^5\,\mathrm{L}_\odot}\right)^{1/2} \left(\frac{1500\,\mathrm{K}}{T_d}\right)^2 Q_{rat}^{-1/2} \tag{S3}$$

where L is the source luminosity and Q_{rat} is the ratio of average absorption efficiency of the dust to the stellar photosphere weighted by the blackbody spectrum of the star. For $T_d \approx 1500\,\mathrm{K}$ and $T_* \approx 5000\,\mathrm{K}$, the analytical approximation in (*30*) provides $Q_{rat} \approx 0.15$, so

$$r_c \approx 28\,\mathrm{au} \left(\frac{L}{10^5\,\mathrm{L}_\odot}\right)^{1/2} \left(\frac{1500\,\mathrm{K}}{T_d}\right)^2 \tag{S4}$$

We attribute the inferred contraction of the inner shell radius to $\lesssim 50\,\mathrm{au}$ (Figure 4A) to dust formation near the condensation radius, causing the apparent shell to shrink in radius starting from the progenitor circumstellar shell. The optical depth of the dust shell increases by a factor of $\gtrsim 10\times$ due to the gradual contraction of the shell, but the total dust mass remains roughly constant in the initial $\approx 1000\,\mathrm{d}$ before increasing by $\approx 10^{-4}\,\mathrm{M}_\odot$ during the subsequent period as the source evolves to the 2022 remnant.

Constraints on mass ejection

We use the continuous optical photometric coverage of M31-2014-DS1 between 2010 and 2020 by PTF and Gaia to place limits on any optical outburst, which is predicted for H-recombination powered transients in failed SNe (*11*). The progenitor light curve (Figure 2) does not show an obvious optical outburst. To quantify the timescale of a possibly missed outburst, we measure the difference between successive observations of the star in PTF r-band and Gaia G-band data, which provide the most frequent temporal sampling. We use the visit separations over this period to quantify the timescale of an outburst that could have been missed between successive observations (Figure S6). We adopt an upper limit on the rise timescale of any missed outburst as half of

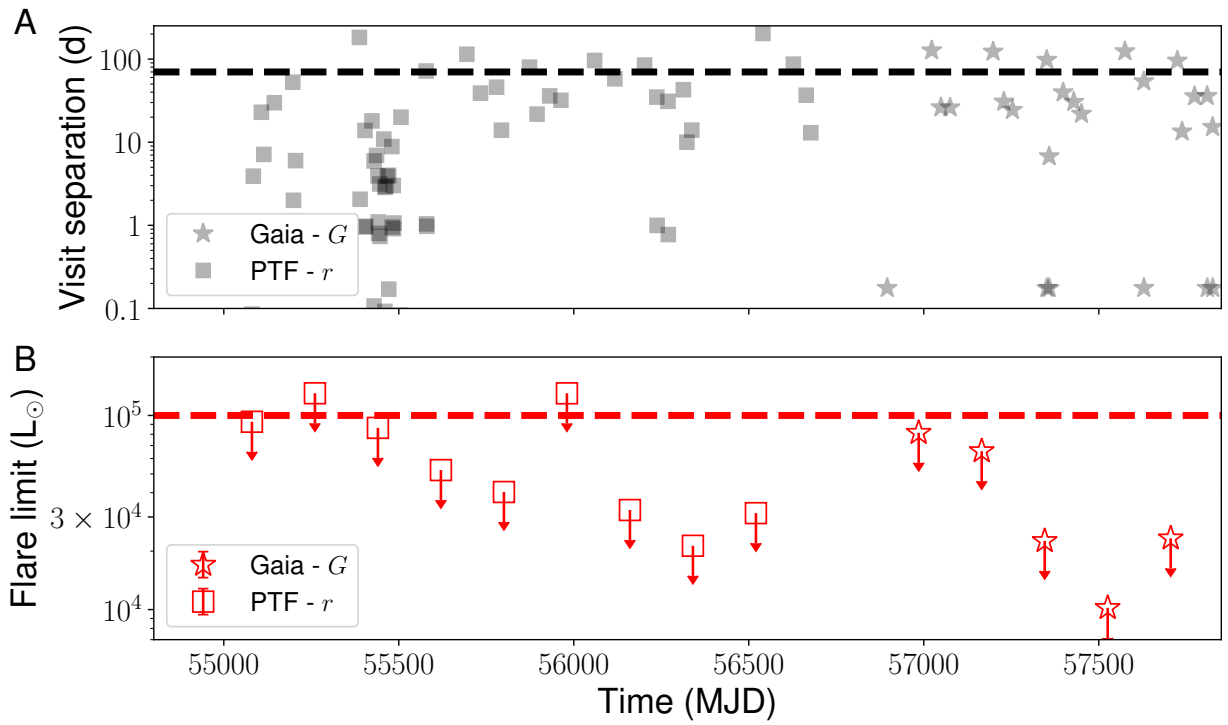

Figure S6: **Constraints on the peak luminosity and timescale of an optical outburst in M31-2014-DS1.** (A) Time separation between successive observations of the source in PTF r-band (squares) and Gaia (stars) observations. (B) Downward arrows are 10σ upper limits on the luminosity of an optical outburst after accounting for the irregular variability of the star (see text). The dashed lines show the adopted upper limits on the timescale (panel A) and luminosity (panel B) of a missed outburst.

the maximum visit separation during this time period $\approx$ 180 d. As the source exhibits irregular variability, which could hide a low amplitude outburst, we measure the standard deviation of the flux variability over six-month bins , and adopt an upper limit on the luminosity of a missed outburst as 10σ deviation from the median luminosity of the source in these bins (Figure S6). We adopt half of the highest luminosity limit during this period ($\approx 10^5$ $L_\odot$) as an upper limit on the luminosity of any missed optical outburst in M31-2014-DS1. These constraints on the outburst luminosity and timescale are shown in Figure 5A as the hatched area.

Stellar mass shock-heated and expelled in a full or partial stellar explosion expands, cools, and radiates as it becomes transparent, producing transient but luminous emission. In the case of hydrogen-rich ejecta like that of Type II SNe, stellar merger ejecta, or weak explosions of massive stars, emission is dominated by the recombination of hydrogen at temperatures of a few to ten

thousand kelvin. Empirical scaling relations characterize the timescale, color, and luminosity of such H-rich ejecta, though depend upon the stellar model and shock passage through the star (*109, 110*). In the case of failed SNe, because the initial infall, shock passage, and subsequent ejection of material happen over one to several stellar dynamical times, we expect transients that are broader but less luminous than their fully impulsive counterparts (*41*). We adopt the scaling relations [(*111*), their equations 13 and 14]:

$$L_{\rm pl} \approx 1.2 \times 10^{42} {\rm erg\ s^{-1}} \times E_{51}^{5/6} M_{10}^{-1/2} R_{500}^{2/3} \kappa_{0.4}^{-1/3} T_{6000}^{4/3}, \tag{S5}$$

where $L_{\rm pl}$ is the transient's plateau luminosity, and

$$t_{\rm pl} \approx 120\ d \times E_{51}^{-1/6} M_{10}^{1/2} R_{500}^{1/6} \kappa_{0.4}^{1/6} T_{6000}^{-2/3}, \tag{S6}$$

where $t_{\rm pl}$ is the plateau duration. E_{51} is the outburst energy in units of 10^{51} erg, M_{10} is the ejecta mass in units of $10\,{\rm M}_\odot$, R_{500} is the progenitor radius in units of $500\,{\rm R}_\odot$, $\kappa_{0.4}$ is the characteristic opacity before recombination in units of $0.4\,{\rm cm^2\ g^{-1}}$, and T_{6000} is the effective temperature at which the recombining material becomes transparent, in units of 6000 K.

We apply this model to determine the range of transient durations and luminosities in Figure 5. For a typical YSG with a mass of $5M_\odot$ and radius of $500R_\odot$ (*25*), the escape velocity is ≈ 60 km s^{-1}. We therefore adopt representative velocities for ejecta above these minimum escape speeds for different stellar models. Figure 5 shows tracks of $v_{\rm ej} = 60$, 300 and $1500\,{\rm km\,s^{-1}}$, with different ejecta masses ranging from $10^{-2}\,M_\odot$ to $3\,M_\odot$. Higher ejecta masses or faster velocities correspond to higher energy events that produce more luminous transients. Figure 5A shows the parameter space of models that are excluded because they would have been detected, given our constraints on the luminosity and duration of an outburst.

Progenitor Stellar Models

We model the implosion of a stellar envelope and the resulting accretion onto a central compact object using the stellar evolution code MESA (*112, 113*) (version 24.08.1). MESA solves the equations of hydrostatic stellar structure and evolves them forward in time by computing the nuclear and thermal time-evolution of a star. We use these models to investigate about the interior density profile of the progenitor star of M31-2014-DS1.

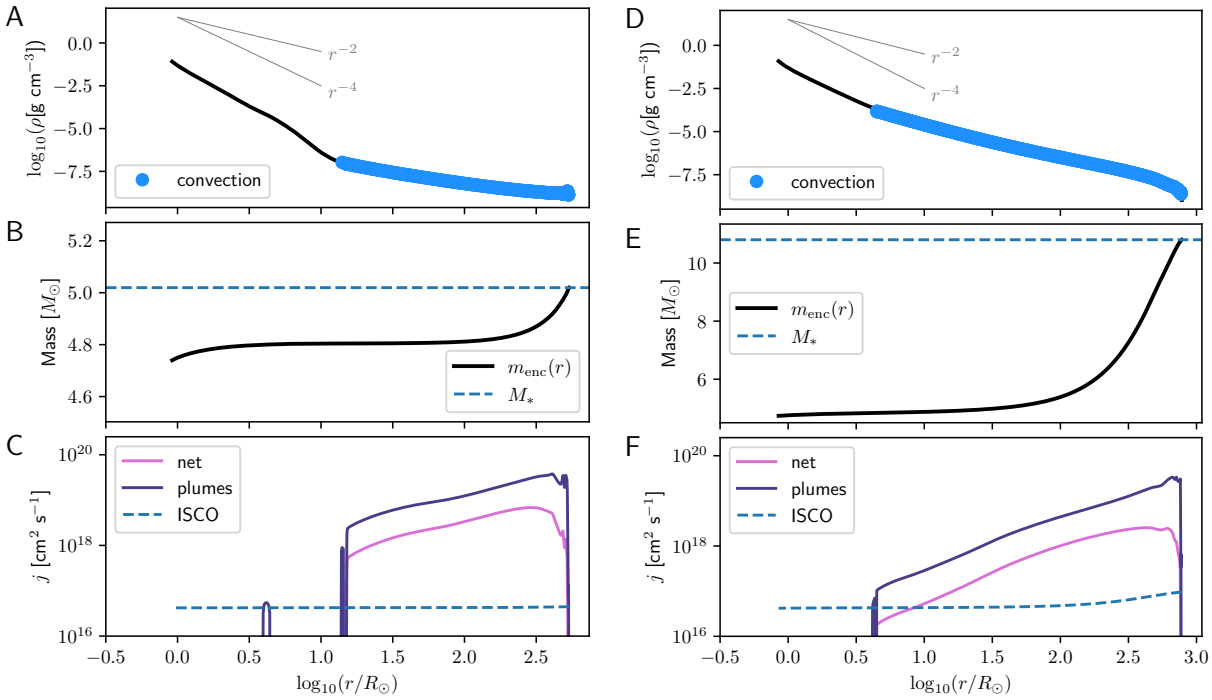

Figure S7: **Comparison of the hydrogen envelope structures of H-poor and H-rich progenitor star models.** (A, D) Radial profile of the mass density in the envelope ρ (black lines), with convective regions highlighted as blue thick regions. Radial density profiles scaling with radius r as r^{-2} and r^{-4} are shown for comparison. (B, E) Radial profiles of the enclosed mass $m_{\rm enc}(r)$ (black lines) with the total model mass shown as a blue horizontal dashed line. (C, F) Radial profiles of the typical angular momentum content j – the net angular momentum (pink lines) and the characteristic angular momentum of convective plumes (purple lines). The blue dashed line indicates j at the innermost stable circular orbit if all of the enclosed mass were to collapse to a BH. We find that convective regions carry much more random angular momentum than a BH horizon, preventing direct fallback of these outer envelope regions.

The detailed structure of the envelopes of massive stars is debated, especially because most models are limited to one dimension and the hydrostatic approximation (*114*). We therefore investigate only the broad differences in stellar structure between stars with large remaining hydrogen envelopes and those largely stripped of hydrogen. By adjusting the model mass loss history, we produce two qualitatively different models that share the approximate luminosity of the observed progenitor. Both models are evolved from the pre-main sequence until carbon core depletion. After carbon core depletion, we expect additional burning stages to continue in the core, but with little effect on the envelope structure.

Hydrogen-poor model: For the hydrogen-poor yellow supergiant model, we remove the majority of a partially-evolved star's hydrogen envelope. Physically, this might happen through phases of enhanced wind or binary mass stripping and exchange. The properties of a model star depend on how and when mass loss occurs. There is no evidence of a binary companion for M31-2014-DS1, but there is evidence for a high mass loss rate of the progenitor $\sim 10^{-4} M_{\odot}$ yr^{-1}, required to produce the circumstellar material that reddens the progenitor spectral energy distribution (Figure 3). We therefore consider a MESA model with an elevated mass loss rate in its late evolution as follows.

We begin with a pre-main-sequence stellar model with initial mass $13\,M_{\odot}$, which is evolved through subsequent burning stages. We adopt a heavy element mass fraction $Z = 0.014$, which is approximately solar. Until core helium exhaustion, we apply a nominal stellar mass loss rate using MESA's 'Dutch' wind scheme, appropriate for massive stars (*115*), with a coefficient of unity. The properties of convection affect our modeling and for the appearance of massive stars; we adopt mixing via the Ledoux criterion as applied in MESA (*113*), and apply a mixing length coefficient $\alpha_{\rm mlt} = 2$. We allow step-function overshooting of 0.345 scale heights above the H-core burning region, which facilitates the growth of the He core.

For late-stage burning, we allow locally super-Eddington regions of the convective envelope that form due to high opacity transitions in the cool outer envelope. We introduced additional energy transport efficiency in these regions, to avoid unrealistic inflation of stellar envelopes in the one-dimensional model. Previous three-dimensional models of the outer layers of convective massive stars have found large-scale convective plumes, time-variable turbulent layers, and effective porosity whereby radiation escapes through lower-density portions of envelope; these effects soften sharp features that occur in one-dimensional models (*113, 114*). We apply MESA's reduction factor to super-adiabatic temperature gradients that might otherwise occur [(*113*), their section 7.2]. The default treatment is active above $L(r)/L_{\rm Edd}(r) > 0.5$, which would apply to the majority of our model stars' envelopes, and allows stellar cores to proceed in their evolution without impediment from the envelope. After experimenting with the MESA settings, we adopted a correction only to Eddington factor $L(r)/L_{\rm Edd}(r) > 1.5$, which smooths the (unphysical) outer density inversion with little effect on the remainder of the envelope. Numerically, we adopt a convective Eddington parameter $\Gamma_{\rm c} = 1.5$, the growth and damping terms for the time-dependent convection $\alpha_1 = \alpha_2 = 20$, and a superadiabicity threhold $\delta_{\rm c} = 0.1$ [(*113*), their equation 73].

At core helium exhaustion, our model star has a total mass of $10.81 M_\odot$, of which $4.73 M_\odot$ are a core of helium and heavier elements. The star has a luminosity of $7.1 \times 10^4 L_\odot$ and an effective temperature of 3870 K. From this epoch onward, the remaining evolution to core carbon depletion lasts $\sim 2.5 \times 10^4$ yr. To this late-stage burning, we manually apply a mass loss rate of $2.376 \times 10^{-4} M_\odot$ yr^{-1}. This mass loss rate is chosen for approximate consistency with the observed progenitor reddening, and to reach core carbon depletion at an effective temperature that is consistent with the $\sim$ 4500 K progenitor in 2005-2012.

The star reaches carbon core depletion (approximated by core carbon mass fraction $< 10^{-4}$) with a total mass of $5.02 M_\odot$. Of this, $4.74 M_\odot$ is the helium core, and $0.28 M_\odot$ is the hydrogen-rich envelope. The model has slightly enhanced surface helium abundance (by $\sim$ 10% relative to its main sequence value), but retains approximately solar surface metal mass fraction. The model star has an effective temperature of 4527 K, and a luminosity of $1.07 \times 10^5 L_\odot$, similar to the constraints on the progenitor star (Figure 3 and Table S2). The model star's radius is $503 R_\odot$, and its escape velocity is $\sim$ 60 km s^{-1}. The interior structure of the hydrogen envelope of this model is shown in Figure S7.

Hydrogen-rich model: To produce a hydrogen-rich counterpart to our hydrogen-poor model, we continue the evolution of the same model star beyond helium core exhaustion, with the same wind settings. At core carbon exhaustion, the mass loss rate is $4.2 \times 10^{-6} M_\odot$ yr^{-1}, substantially lower than in the hydrogen-poor model. The star is $10.80 M_\odot$, of which $4.74 M_\odot$ are a core of helium and heavier elements. The star has a luminosity of $1.12 \times 10^5 L_\odot$ and an effective temperature of 3717 K. The star's radius is $779 R_\odot$, and its escape velocity is 73 km s^{-1}. This model is compared with the hydrogen-poor model in Figure S7, which shows that the hydrogen-rich star has a more extended convection zone, and thus carries more of its (overall greater) mass at large radii.

Simulations of energy injection and fallback

We adopt a simplified model of energy injection into these stellar envelopes by an outgoing shock, launched following the collapse of the core. The physics of shock energy deposition in failed SNe depends on factors including: the outward shock propagation through the infalling stellar material (*116, 117*), the time-dependence of collapse of the core into a proto-neutron star (*51*),

and on possible flow reversal and feedback from innefficient accretion onto a forming compact object (*12, 118*) (*41, 119*). For qualitative comparison, we examine a model in which a given kinetic energy $E_{\rm sh}$ is added to stellar layers following a simple, power-law prescription (*39*):

$$v_{\rm sh} = v_0 \left(\frac{r}{R_*} \right)^{\alpha_{\rm sh}}, \tag{S7}$$

where $v_{\rm sh}$ is the post-shock velocity, v_0 is a velocity scale, r is the radius within the star, R_* is the total stellar radius, and $\alpha_{\rm sh}$ is a power-law index. We assume $\alpha_{\rm sh} = 1$. We integrate this profile over the stellar envelope to obtain the energy input,

$$E_{\rm sh} = \int_0^{R_*} 2\pi r^2 \rho v_{\rm sh}^2 dr, \tag{S8}$$

and treat v_0 as a free parameter to match $E_{\rm sh}$ which we are trying to simulate. A fluid parcel is initially launched outward but may reverse and fall back if $v_{\rm sh}$ is less than the local escape velocity. Material expelled with $v_{\rm sh} < v_{\rm esc}$, where $v_{\rm esc}(r) = (2Gm/r)^{1/2}$ is the escape velocity, has a maximal radius

$$r_{\rm tr}(r) = r \left(1 - \left(\frac{v_{\rm sh}(r)}{v_{\rm esc}(r)} \right)^2 \right)^{-1} \tag{S9}$$

where r is the initial radius and $r_{\rm tr}(r)$ is the maximal, or "turning" radius of material initially at radius r. The fallback time $t_{\rm fb}(r)$ for a shell of bound stellar material expelled to turning radius $r_{\rm rt}$ is then

$$t_{\rm fb}(r) = \left(1 + \frac{v_{\rm sh}(r)}{v_{\rm esc}(r)} \right) t_{\rm ff}(r_{\rm rt}(r)) \tag{S10}$$

where G is the gravitational constant, m is the mass enclosed within radius r, and

$$t_{\rm ff}(r) = \pi \left(\frac{r^3}{8Gm} \right)^{1/2}. \tag{S11}$$

If $v_{\rm sh} = 0$, then $r_{\rm rt}(r) = r$ and the fallback time reduces to $t_{\rm ff}(r)$. The mass fallback rate is then $\dot{M} = dm_{\rm shell}/dt_{\rm fb}$ where $dm_{\rm shell}$ is the mass within a differential thin shell at radius r. At late times, when marginally bound material falls back, the asymptotic fallback rate changes with time t as

$$\dot{M} \approx \frac{2\pi}{3} r_0^2 \rho(r_0) v_{\rm esc}(r_0) \left(\frac{t}{t_{\rm ff}(r_0)} \right)^{-5/3}, \tag{S12}$$

where r_0 and the quantities that depend on it are evaluated at the critical radius where the shock velocity equals the escape velocity $v_{\rm sh}(r_0) = v_{\rm esc}(r_0)$. The unbound mass $m_{\rm ej}$ is material with

$v_{\rm sh}(r_0) > v_{\rm esc}(r_0)$, or

$$m_{\rm ej} = \int_{r_0}^{R_*} 4\pi r^2 \rho dr. \tag{S13}$$

Random angular momentum in turbulently convective envelopes of supergiant stars cause substantial departures from spherical symmetry during collapse (*13, 118, 119*). We expect individual plumes of stellar material to have a broad, isotropic specific angular momentum distribution with characteristic amplitude $j_{\rm plumes}$ of

$$j_{\rm plumes} \approx r v_{\rm conv} \tag{S14}$$

where $v_{\rm conv}$ is the typical convective velocity at radius r. We determine its value from mixing length theory applied to the stellar models. These plumes, if they freefall, become rotationally supported at a radius $r_{\rm circ}$

$$r_{\rm circ} \approx \frac{j_{\rm plumes}^2}{GM}. \tag{S15}$$

The specific angular momentum for material orbiting at the ISCO $j_{\rm ISCO}$ is approximately (depending on the BH's spin)

$$j_{\rm ISCO} \approx \frac{2GM_{\rm BH}}{c}. \tag{S16}$$

where c is the speed of light. The ratio of circularization radius to the radius of the innermost stable circular orbit $r_{\rm ISCO}$ is

$$\frac{r_{\rm circ}}{r_{\rm ISCO}} \approx \left(\frac{j_{\rm plumes}}{j_{\rm ISCO}}\right)^2. \tag{S17}$$

Below this radius angular momentum is dynamically important and imparts turbulence. The mass that falls inward is a function of radius, with turbulent convective motion preventing some degree of infall. We parameterize the accretion rate through radius r as

$$\dot{m} \approx \dot{m}(r_{\rm circ}) \left(\frac{r}{r_{\rm circ}}\right)^{\beta} \tag{S18}$$

where $\beta \sim 0.5$ is a power-law index characterizing the suppression of mass accretion due to the turbulent motion, $\dot{m}(r_{\rm circ})$ is the rate that mass reaches the circularization radius as material falls in from the stellar envelope. Previous generalized simulations of turbulent infall (*120*) derived $\beta \approx 0.7$ for gas with polytropic index $\gamma = 5/3$, or $\beta \approx 0.6$ for RSG collapse (*119*). We adopt the latter value, so

$$\dot{m}_{\rm BH} \approx \dot{m}(r_{\rm circ}) \left(\frac{r_{\rm ISCO}}{r_{\rm circ}}\right)^{0.6}. \tag{S19}$$

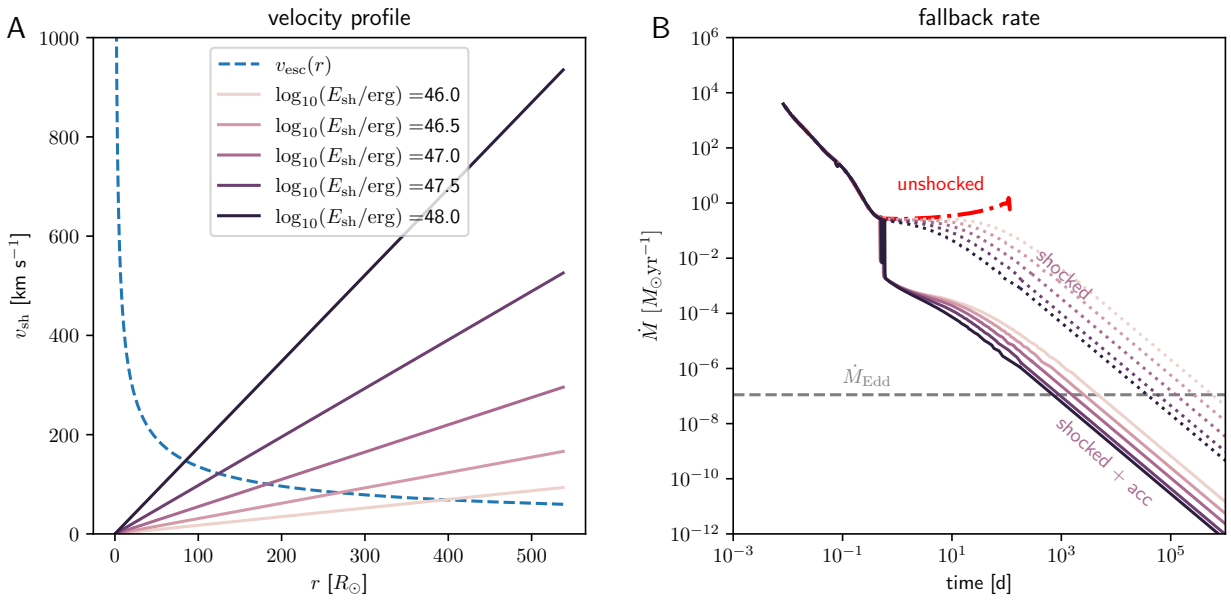

Figure S8: **Radial velocity profiles of the shocked material and the resulting fallback accretion rate in the failed SN model**. (A) Colored lines show the radial velocity ($v_{\rm sh}$) profile of the shocked material for different shock energies $E_{\rm sh}$. The blue dashed line shows the radial profile of the local escape velocity $v_{\rm esc}(r)$; regions with $v_{\rm sh} > v_{\rm esc}(r)$ yield unbound material, while regions with $v_{\rm sh} < v_{\rm esc}(r)$ fall back towards the core. (B) Mass fallback rate (shown as colored lines corresponding to the same shock energies in panel A) due to the infall of the shocked material. The dotted lines show the fallback rate without accounting for the inefficient accretion induced by the angular momentum barrier of the initial convective envelope; solid lines show the same after implementing the suppression of mass accretion. The case of unshocked material ($E_{\rm sh} = 0$) fallback is shown as a red dot-dashed line.

To compute the emergent luminosity from the accretion process in the late-time evolution, we adopt a simple radiative efficiency $\eta = 0.05$, the conversion factor from rest mass energy of the accreted material to the radiated luminosity $L = \eta \dot{m} c^2$.

Figure S8 shows the shock-injection, fallback, and accretion model applied to the H-poor progenitor MESA model, for a range of typical shock energies (*51*). Sufficiently strong shocks generate unbound material, and spread gas into marginally-bound trajectories that fall back at late-time with a dependence that asymptotes to $t^{-5/3}$. The effect of angular momentum is to greatly reduce the accretion efficiency, such that the BH accretion rate drops below its Eddington limit after about 10^3 d post-collapse, for shock energies in the range of 10^{46} to 10^{48} erg. Compared to the case of an unshocked star (i.e. fallback without energy injection) which complete falls back within

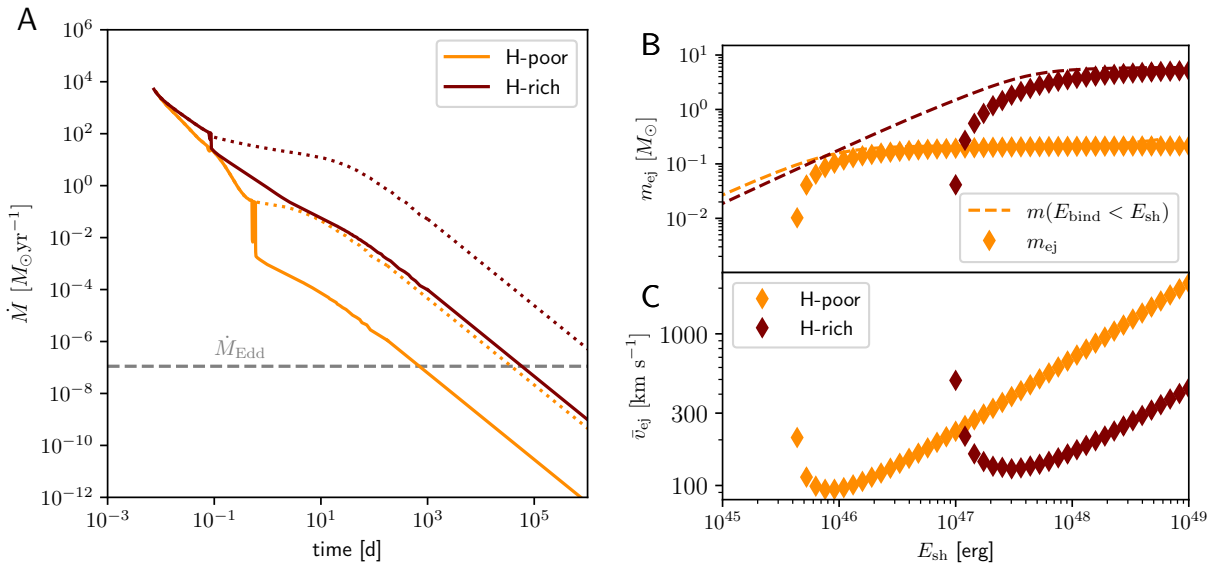

Figure S9: **Comparison of fallback and mass ejection in H-rich and H-poor progenitor models.** (A) Same as Figure S8B but comparing the fallback in the H-rich and H-poor models, with solid and dotted lines similarly showing the mass fallback rate with and without inefficient accretion. The Eddington mass accretion rate for a 5 $M_\odot$ compact object is shown as a gray horizontal dashed line for comparison. (B) Comparison of the ejected mass in the H-poor and H-rich models as function of the shock energy (diamonds). The dashed lines show the amount of mass with binding energy $E_{\rm bind}$ smaller than the input shock energy, with ejected mass asymptotically approaching this value for large shock energies. (C) Same as panel (B) but showing the velocity of the ejected material as a function of the shock energy.

$\sim$ 100 d (Figure S8B), the bulk of the mass ejection and fallback occurs thousands of days after core collapse.

Figure S9 compares the fallback and mass ejection for the H-rich and H-poor progenitor models. In the H-rich case, the late-time fallback from the mass-rich envelope is high (above the Eddington limit for 10^5 d$\sim$ 300 yr). The centrally concentrated H-poor model mostly accretes early, and drops below the Eddington limit in a few years. The expected ejecta properties also diverge. The H-rich model yields several solar masses of ejecta and transients of $L > 10^6 L_\odot$ for hundreds of days. The H-poor model ejects about $0.1 M_\odot$ at a higher velocity of several hundred km s^{-1}. Figure 5 shows the predicted luminosity and timescale for the resulting outbursts (for H-recombination powered events). We find that the predicted transient from a hydrogen-poor supergiant would last tens of days, which is sufficiently brief to have been missed by the optical photometry (Figure S6). The faint luminosity of the predicted outbursts for low shock energies ($\sim 10^{39}$ erg s^{-1} for $E_{\rm sh} \lesssim 10^{48}$ erg;

Figure 5) compared to the initial stellar luminosity ($\sim 5 \times 10^{38}$ erg s^{-1} from 2005-2012; Figure 3) would prevent the detection of an outburst given its irregular optical variability ($\approx 5\times$ in r-band; Figure 2) and consistent with the 10σ upper limits on any optical outburst (Figure S6).

Physical limits from X-ray non-detection

The accretion of the turbulent convective envelope onto the BH is inefficient, causing most of the outer envelope material to be expelled (Figure S8B; (*41*)). Both ejected and bound material can obscure emission from near the BH. We estimate the column density of hydrogen from the unbound component $N_{\rm H,ej}$ with $v_{\rm sh} > v_{\rm esc}$, which we assume to continue to expand at constant velocity, such that its radius is $v_{\rm sh}t$. Each radial zone in the initial stellar structure has mass dm. Then,

$$N_{\rm H,ej} \approx \frac{1}{m_p} \int \frac{dm}{4\pi (v_{\rm sh} t)^2} \tag{S20}$$

where m_p is the proton mass. $N_{\rm H,ej}$ scales as t^{-2}. The initially bound component that falls back toward the BH contains both the small fraction of material that accretes and the majority that is expelled instead. We neglect feedback from the passing shock (*41*) to estimate the column density of un-accreted material as a function of time. Most of the infall reverses around a scale of $r_{\rm circ}$, and expands from there. We estimate that the fallback driven outflow produces a column density $N_{\rm H,wind}$

$$N_{\rm H,wind} \sim \frac{1}{m_p} \frac{\dot{m}(r_{\rm circ})}{4\pi r_{\rm circ} v_{\rm esc}(r_{\rm circ})} \tag{S21}$$

This component scales with the fallback rate, and therefore decays as $t^{-5/3}$ at late times. Thus, the ejecta column dissipates first, so at late times the remaining column density depends on the inefficient accretion-and-outflow process.

Figure S10 estimates the column density as a function of time from our model. This includes both the unbound and reversing-fallback components. At late times, the more uncertain accretion outflow component dominates, due to its shallower time decay. For characteristic energies of $\sim 10^{47}$ erg, the column density along the line of sight drops below 10^{24} cm^{-2} – the approximate level to allow soft X-rays to penetrate – from a few $\times 10^3$ to 10^4 d. To quantitatively compare against our observations, we track the expected evolution of our model as a function of the surrounding column density and accretion luminosity (both of which decrease rapidly with time). Figure S10 compares those model predictions to the estimated total N_H at the epochs of the archival Chandra,

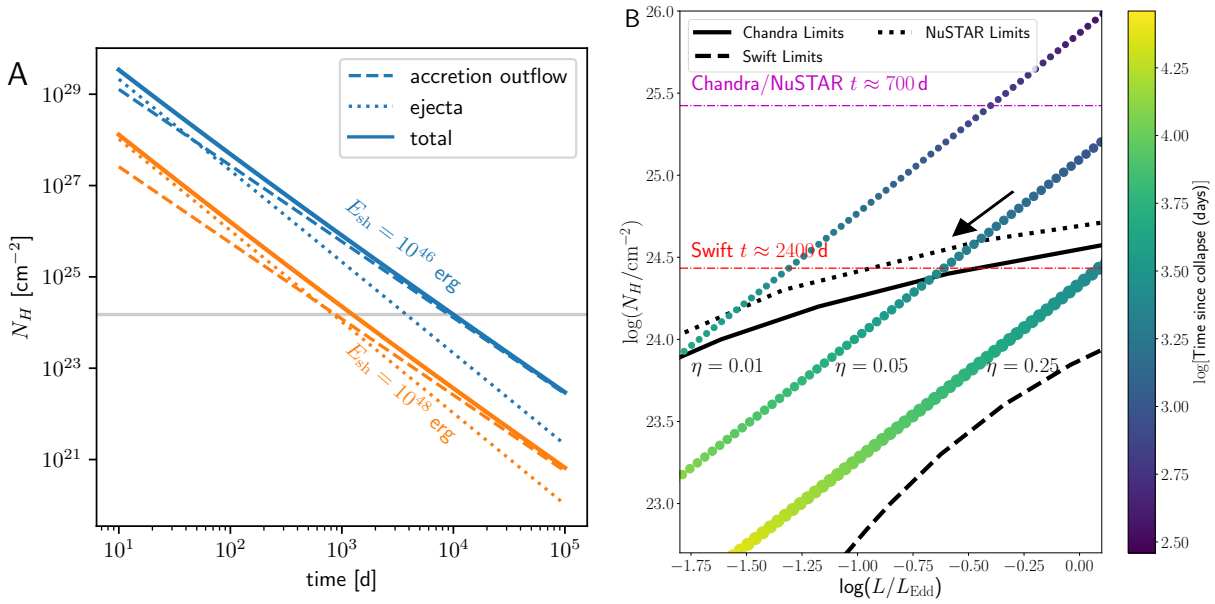

Figure S10: **Predicted evolution of the hydrogen column density N_H surrounding a newborn BH as a function of time and accretion luminosity (L), for different shock energies.** (A) Temporal evolution of the column density from the expanding ejecta (dotted lines), the accretion outflow from fallback material (dashed lines), and the total column density (solid lines) for two shock energies. The gray horizontal line shows $N_H \lesssim 1.5 \times 10^{24}$ cm^{-2}, where the Thompson optical depth becomes < 1 and the source may emerge in X-ray emission. (B) Evolution of the column density as a function of the accretion luminosity (normalized to the Eddington luminosity of a $5\,M_\odot$ BH) for $E_{sh} = 10^{47}$ erg, with the symbol colors indicating the time evolution (shown on the right color bar, and the arrow indicating the direction of increasing time) for three different radiative efficiencies ($\eta = 0.01, 0.05, 0.25$). The magenta dot-dashed and red dashed lines show the estimated N_H from the model at the epoch of the archival Chandra/NuSTAR (end of 2015) and Swift X-ray observations, respectively. The black solid, dotted and dashed lines show the detection threshold for X-ray emission for the respective Chandra, NuSTAR and Swift X-ray observations, where only regions below the lines would be detectable in the data.

NuSTAR and Swift X-ray observations and the phase space of N_H and L that are ruled out by the X-ray non-detections (assuming a $\Gamma = 2$ intrinsic X-ray spectrum). The calculations indicate that the source was too heavily obscured to be detected at the epochs of the archival X-ray observations.

Supplementary Text

The case of NGC 6946-BH1

M31-2014-DS1 shares several similarities with a previously reported failed SN candidate NGC 6946-BH1 (*16, 47, 48*). Both have a luminous supergiant progenitor, bolometric decay and a remnant

dominated by infrared emission. While the progenitor was interpreted as a RSG based on a comparison of its colors to single star evolutionary tracks (*16*), its pre-outburst colors were shown to be consistent with a hydrogen depleted yellow supergiant (*52*). The progenitor of NGC 6946-BH1 also had an infrared excess (*16*) indicating of intense terminal mass loss. For quantitative comparisons, we repeated the same analysis as above but applied to NGC 6946-BH1 by producing a stellar model that matches the reported luminosity and temperature of its progenitor ($\log(L/L_\odot) = 5.29^{+0.04}_{-0.06}$, $T_{\rm eff} = 4480^{+1670}_{-320}$; Figure 3B).

Adopting the same MESA parameters, we model the NGC 6946-BH1 progenitor as an initially 17.5 $M_\odot$ star with solar metallicity. We evolve this star to helium core depletion with the same mass loss prescription, at which point it has a mass of $12.62 M_\odot$, of which $6.89 M_\odot$ are a core of helium and heavier elements. To produce a hydrogen-poor model consistent with the yellow-supergiant hypothesis, after helium depletion, we apply an enhanced mass loss rate of $3.915 \times 10^{-4} M_\odot$ yr^{-1} until carbon is depleted in the star's core. At that point, the model star has a total mass of $7.52 M_\odot$, of which $6.90 M_\odot$ are the core and $0.62 M_\odot$ are hydrogen-rich. The surface helium abundance by mass is slightly enhanced relative to its initial state (0.31 versus 0.25 in the initial model), while the surface metal abundance remains solar. The model star has a luminosity of $1.81 \times 10^5 L_\odot$, and an effective temperature of 4562 K.

Figure S11 shows that the higher hydrogen envelope mass and larger radius for this stellar model (compared to M31-2014-DS1) results in the ejection of more mass ($\sim 0.3\,{\rm M}_\odot$) at higher velocities ($\sim 300\,{\rm km\,s^{-1}}$). The outburst properties associated with H-recombination for the ejecta are shown in Figure S12, compared to the H-poor and H-rich progenitor models for M31-2014-DS1. We find that the larger ejecta mass produces a longer duration outburst in the H-poor models. For NGC 6946-BH1, the total duration of the outburst was poorly constrained as between 3 and 11 months (*16*). Taking the rise time of the outburst to be half of the total duration, Figure S12A shows that the observed outburst properties of the source are consistent with a $\sim 10^{47}$ erg shock powered by neutrino mass loss.

Figure S12B shows the evolution of the mass fallback rate as the loosely bound material falls back into the stellar core. The $\approx 3\times$ more massive H-envelope leads to a longer time of ≈ 2000 d before the accretion falls below the Eddington rate, then fades by a factor of 10 over a few thousand days after the collapse. NGC 6946-BH1 was previously reported to fade to $\approx 15\%$ of its progenitor

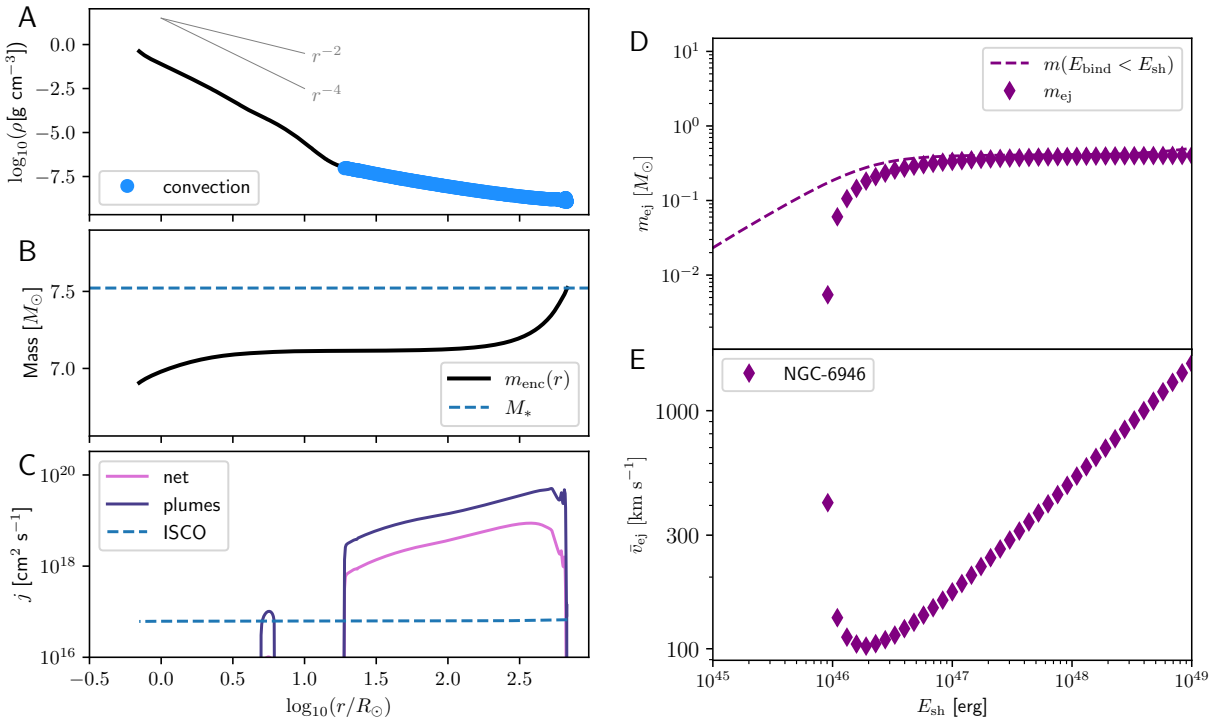

Figure S11: **Stellar model and predicted outburst properties for the progenitor of NGC 6946-BH1**. (A-C) Same as Figure S7A-C for the NGC 6946-BH1 terminal stellar model. (b) Same as Figure S9B-C, but for the NGC 6946-BH1 stellar model.

luminosity in $\sim$ 3000 d (*16*), Figure S12B compares its bolometric light curve (converted to effective mass accretion rate) to our model. Observations of the NGC 6946-BH1 remnant at $\approx$ 5100 d show that it has a luminosity of $\sim 10-20\%$ of the progenitor (*49, 50*). Earlier epochs of observation did not have mid-IR coverage (therefore the bolometric luminosity was poorly constrained). Nevertheless, the slower fading of NGC 6946-BH1 is consistent with our model, which predicts fading by a factor of 2 to 3 over a decade.

Comparison to rates of failed SNe

An observational strategy has been previously proposed (*7*) to search for the disappearance of massive stars due to stellar collapse into a BH, possibly accompanied by a low luminosity transient. Given the typical lifetime of an evolved supergiant ($\sim 10^6$ years), a survey monitoring $\sim 10^6$ supergiants could identify massive stellar death (either as a successful or failed SN) at a rate of $\approx 1\,\mathrm{yr}^{-1}$ (*7*), and constrain the fraction of failed SNe. A $\approx$ 11 yr survey (*18, 47, 56*) led to the

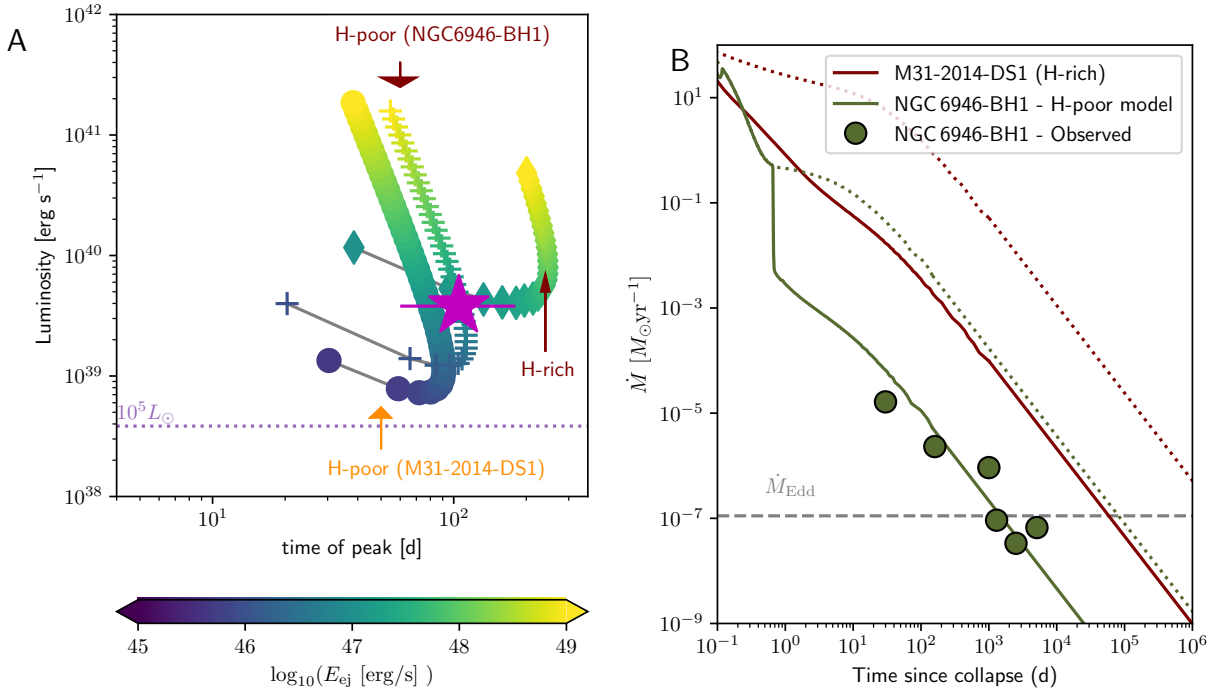

Figure S12: **The predicted outburst properties and late-time mass fallback evolution for the model for NGC 6946-BH1, compared to the H-poor and H-rich models for M31-2014-DS1.** (A) Same as Figure 5A for the H-poor model for M31-2014-DS1 (circles), the H-rich model for M31-2014-DS1 (diamonds) and the progenitor model for NGC 6946-BH1 (plus symbols) with the shock energy shown on the color bar. The magenta star shows the observed luminosity and duration of the NGC 6946-BH1 outburst. The horizontal dotted line shows progenitor luminosity for M31-2014-DS1. (B) Same as Figure S8B but comparing the mass fallback evolution for the H-rich progenitor model of M31-2014-DS1 and the H-poor progenitor model of NGC 6946-BH1, for shock energy of 10^{48} erg. The observed bolometric light curve of NGC 6946-BH1 is shown after converting luminosity into mass accretion rate assuming a radiative efficiency of $\eta = 0.05$.

identification of NGC 6946-BH1 (*16*) and another less constrained candidate (*18*). A previous search of archival data for low luminosity optical transients reported no detections or candidates (*57*).

Our NEOWISE search was sensitive to variability of supergiants in M31 and M33 down to a luminosity threshold of $\gtrsim 10^{37}$ erg s^{-1}. Taking the luminosity of the MIR brightening in M31-2014-DS1 ($\approx 10^{38}$ erg s^{-1}), and considering that dust luminosity scales linearly with the ejected mass in the optically thin brightening phase, our search was sensitive to all outbursts with ejected mass $\gtrsim 10^{-2}$ M$_\odot$ ($\approx 10\%$ of that M31-2014-DS1). This covers the entire range of expected H-envelope masses in supergiant stars (*121*), the survey included $\approx 2 \times 10^4$ supergiants (with optical luminosity $\gtrsim 3.5 \times 10^3$ L$_\odot$) in M31 and M33 [(*7*), their Figure 4] and had a ≈ 15 yr baseline.

The fraction of massive star deaths that result in failed SNe (f) is unknown, with previous studies proposing a lower limit of $f \gtrsim 0.25$ based on the local BH density (*7*), estimate $f \approx 0.04-0.4$ based on the previous survey (*18*), and an upper limit of $f < 0.61$ (*57*). Assuming a typical supergiant lifetime of $\sim (5-10) \times 10^5$ yr, we therefore estimate the number of such events in M31 and M33 to be $\approx 0.01-0.2$ for $f \approx 0.05-0.5$ over a duration of ≈ 15 yr. Therefore, our identification of one such event is not improbable but fortuitous, even if the fraction of failed events is close to the upper limit. A similar calculation for the previous survey that monitored $\sim 10^6$ supergiants over the same duration (*7*) found an expected number of $0.5-5$ events, consistent with their results (two candidates). The high inferred fraction is consistent with theoretical predictions that BH formation can occur in stars with masses as low as $\approx 13\,M_\odot$.

Table S1: Archival space-based photometry of M31-2014-DS1 from HST and SST. Uncertainties are 1σ confidence, and upper limits are 5σ.

Epoch (MJD)	Filter	AB Mag	Instrument
56115	F110W	16.86 ± 0.05	HST/WFC3-IR
56115	F160W	16.83 ± 0.05	HST/WFC3-IR
56273	F475W	19.15 ± 0.05	HST/ACS
56273	F814W	17.05 ± 0.10	HST/ACS
56115	F336W	23.25 ± 0.10	HST/WFC3-UVIS
56115	F275W	> 26.18	HST/WFC3-UVIS
53391	Channel 1 (3.6 μm)	16.37 ± 0.01	SST/IRAC
53391	Channel 2 (4.5 μm)	16.47 ± 0.01	SST/IRAC
53391	Channel 3 (5.8 μm)	16.05 ± 0.01	SST/IRAC
53391	Channel 4 (8.0 μm)	15.95 ± 0.01	SST/IRAC
53243	Channel 1 (24.0 μm)	15.69 ± 0.10	SST/MIPS
59617	F606W	> 28.48	HST/WFC3-UVIS
59617	F814W	27.30 ± 0.23	HST/WFC3-UVIS

Table S2: Best-fit DUSTY parameters for the progenitor and remnant of M31-2014-DS1.

Model	F (10^{-12} erg cm^{-2} s^{-1})	$\log(L/L_\odot)$	$T_{\rm eff}$ (K)	T_d (K)	τ	Y	A_V (mag)
Progenitor	$5.0^{+1.0}_{-0.7}$	$4.97^{+0.08}_{-0.07}$	4500^{+610}_{-520}	880^{+180}_{-140}	$2.8^{+0.4}_{-0.5}$	54^{+31}_{-32}	$0.1^{+0.2}_{-0.1}$
Remnant	$0.5^{+0.2}_{-0.1}$	$3.97^{+0.15}_{-0.10}$	6800^{+4100}_{-1800}	960^{+220}_{-170}	$22.0^{+1.5}_{-1.5}$	10 (fixed)	0.1 (fixed)